

**Strain Transducers for Active Control
- Lumped Parameter Model -**

Y. Aoki, P. Gardonio and S.J. Elliott

ISVR Technical Memorandum N° 970

August 2006



SCIENTIFIC PUBLICATIONS BY THE ISVR

Technical Reports are published to promote timely dissemination of research results by ISVR personnel. This medium permits more detailed presentation than is usually acceptable for scientific journals. Responsibility for both the content and any opinions expressed rests entirely with the author(s).

Technical Memoranda are produced to enable the early or preliminary release of information by ISVR personnel where such release is deemed to be appropriate. Information contained in these memoranda may be incomplete, or form part of a continuing programme; this should be borne in mind when using or quoting from these documents.

Contract Reports are produced to record the results of scientific work carried out for sponsors, under contract. The ISVR treats these reports as confidential to sponsors and does not make them available for general circulation. Individual sponsors may, however, authorize subsequent release of the material.

COPYRIGHT NOTICE

(c) ISVR University of Southampton All rights reserved.

ISVR authorises you to view and download the Materials at this Web site ("Site") only for your personal, non-commercial use. This authorization is not a transfer of title in the Materials and copies of the Materials and is subject to the following restrictions: 1) you must retain, on all copies of the Materials downloaded, all copyright and other proprietary notices contained in the Materials; 2) you may not modify the Materials in any way or reproduce or publicly display, perform, or distribute or otherwise use them for any public or commercial purpose; and 3) you must not transfer the Materials to any other person unless you give them notice of, and they agree to accept, the obligations arising under these terms and conditions of use. You agree to abide by all additional restrictions displayed on the Site as it may be updated from time to time. This Site, including all Materials, is protected by worldwide copyright laws and treaty provisions. You agree to comply with all copyright laws worldwide in your use of this Site and to prevent any unauthorised copying of the Materials.

UNIVERSITY OF SOUTHAMPTON
INSTITUTE OF SOUND AND VIBRATION RESEARCH
SIGNAL PROCESSING AND CONTROL GROUP

**Strain Transducers for Active Control
- Lumped Parameter Model -**

by

Y Aoki, P. Gardonio and S.J. Elliott

ISVR Technical Memorandum No: 970

August 2006

Authorised for issue by
Prof. R. Allen
Group Chairman

Contents

1	INTRODUCTION	7
1.1	Active Structural Acoustic Control	7
1.2	Scope and Objectives	8
1.3	Structure of the Report	9
2	ACTIVE CONTROL AND STABILITY	10
2.1	DVFB Control	12
2.2	Open Loop Frequency Response Function	14
2.3	Control Performance	16
3	MODEL PROBLEM	19
3.1	Actuator Mass Effect	19
3.2	Actuator Stiffness Effect	23
3.3	Actuator-Panel Fully Coupled Model	31
3.4	Sensor-Actuator Fully Coupled Model	33
3.4.1	Sensor dynamics	33
3.4.2	Fully coupled model	36
3.5	Models Validation	41
4	PARAMETRIC STUDY OF PIEZOELECTRIC PATCH ACTUATOR	45
4.1	Size	45
4.2	Thickness	50
4.3	Combined Size and Thickness with Constant Volume	54
4.4	Offset Length	58
5	CONCLUSION	62
A	Classical thin plate theory	64
A.1	Equation of Motion	64
A.2	Force Actuator	67
A.3	Strain Actuator	68
B	Mobility	71
B.1	Ideal Sensor and Ideal Actuator	71
B.2	Ideal Sensor and Lightweight Actuator	72
B.3	Ideal Sensor and Elastic Actuator	73
B.4	Actuator-Plate Fully Coupled Model	75

B.5 Actuator-Sensor-Plate Fully Coupled Model	77
C Piezoelectric Actuator Induced Moment	78
Reference	82

List of Figures

1.1	Smart panel with a piezoelectric patch actuator and a velocity sensor at its center for the implementation of a direct velocity feedback control loop that generates active damping	7
2.1	Physical arrangement of test rigs, which consist of an acoustic cavity with rigid walls and a baffled clamped smart panel, excited by a transverse point force generated by a shaker	11
2.2	Moments excitation generated by a piezoelectric patch that is bonded on the bottom side of the panel, when the applied voltage has the same polarity as the poling voltage.	13
2.3	Block diagram of the direct velocity feedback control system	13
2.4	The Bode plot (left) and the Nyquist plot(right) of the open loop FRF of a closely located velocity sensor and a square piezoelectric actuator(solid line), and the predicted phase lag (dashed line)	16
2.5	Definition of the stability coefficient (δ_0) and the control performance coefficient(δ_{rk})	18
2.6	Maximum reduction index R_k with reference to the control ratio δ_{0k}	18
3.1	Schematic representation of distributed mass model	20
3.2	The Bode plot (top) and the Nyquist plot (bottom 1 by 2 array) of the open loop FRF between the ideal velocity sensor and either the massless piezoelectric actuator (faint line, left), or the lightweight piezoelectric actuator (dotted line, right)	22
3.3	Schematic representation of the actuator stiffness model with single pair of springs	23
3.4	Schematic representation of the lumped spring model of the actuator patch with the notation of the forces and displacements at the connecting points between the lumped spring and the smart panel in x-direction (top) and y-direction(bottom)	28
3.5	Schematic representation of the actuator stiffness model with multiple pairs of springs	28
3.6	The Bode plot (top) and the Nyquist plot (bottom 1 by 2 array) of the open loop FRF of the ideal velocity sensor and the piezoelectric actuator without (faint line, left) and with (dotted line, right) stiffness effect of the piezoelectric actuator	29
3.7	Actuation moment (solid black line) and total moment including the stiffness effect of the actuator patch (blue dotted line) without(left) and with(right) the factor of the maximum operating voltage	30

3.8	The Bode plot (top) and the Nyquist plot (bottom 1 by 2 array) of the open loop FRF between the ideal velocity sensor and the piezoelectric actuator without (faint line, left) and with (dotted line, right) inertia and elastic effects of the piezoelectric actuator	32
3.9	Internal structure of tri-shear piezoelectric sensing accelerometer 352C67 . . .	33
3.10	Schematic representation of the piezoelectric accelerometer transducer, which is modeled as a single degree-of-freedom system	34
3.11	Transfer function between the acceleration of the panel at the sensor position and the voltage signal output of the accelerometer	36
3.12	Schematic representation of a piezoelectric accelerometer transducer, and the notation of the forces and displacement at the connecting points between the elements of the accelerometer and the smart panel	37
3.13	The Bode plot (top) and the Nyquist plot (bottom, 1 by 2 array) of the open loop FRF between the ideal accelerometer sensor and the practical piezoelectric actuator (faint line), the open loop FRF between the integrated signal from the accelerometer sensor and the practical piezoelectric actuator (dotted line, right)	40
3.14	The Bode plot (top) and the Nyquist plot (bottom, 1 by 2 array) of simulated open loop FRF using the plate-actuator fully coupled model (solid line, left), and measured open loop FRF between the input signal to the piezoelectric actuator and the output signal obtained by laser vibrometer (dotted line, right)	43
3.15	The Bode plot (top) and the Nyquist plot (bottom, 1 by 2 array) of the simulated open loop FRF using the plate-actuator-sensor fully coupled model (solid line, left), and the measured open loop FRF between the input signal to the piezoelectric actuator and the digitally integrated output signal obtained by the accelerometer sebsor (dotted line, right)	44
4.1	The Bode plot (top) and the Nyquist plot (bottom 2 x 2 array) of the open loop FRF between the ideal velocity sensor and various size actuators; Case 1: 20x20mm (faint line, left top), Case 2: 30x30mm (dotted line, right top), Case 3: 40x40mm (dash-dotted line, left down), Case 4: 50x50mm (dashed line, right down)	47
4.2	The Bode plot (top) and the Nyquist plot (bottom 2 x 2 array) of the open loop FRF between the integrated signal of the accelerometer sensor and various size actuators; Case 1: 20x20mm (faint line, left top), Case 2: 30x30mm (dotted line, right top), Case 3: 40x40mm (dash-dotted line, left down), Case 4: 50x50mm (dashed line, right down)	48
4.3	Flexural wavelength with reference to frequency	49
4.4	Maximum vibration reduction at 1st(blue solid line), 4th (black dotted line), 8th (red dot dashed line), and 11th resonance (green dashed line) with reference to the size length, using the ideal velocity sensor-actuator pair (left) or accelerometer sensor-actuator pair (right)	49
4.5	The Bode plot (top) and the Nyquist plot (bottom 2 x 2 array) of the open loop FRF between the ideal velocity sensor and various thickness actuators; Case 1: 0.001mm (faint line, left top), Case 2: 0.25mm (dotted line, right top), Case 3: 0.5mm (dash-dotted line, left down), Case 4: 1.0mm (dashed line, right down)	51

4.6	The Bode plot (top) and the Nyquist plot (bottom 2 x 2 array) of the open loop FRF between the integrated signal of the accelerometer sensor and various thickness actuators; Case 1: 0.001mm (faint line, left top), Case 2: 0.25mm (dotted line, right top), Case 3: 0.5mm (dash-dotted line, left down), Case 4: 1.0mm (dashed line, right down)	52
4.7	Maximum vibration reduction at 1st(blue solid line), 4th (black dotted line), 8th (red dot dashed line) ,and 11th resonances (green dashed line) with reference to the thickness of the actuator using the ideal velocity sensor-actuator pair (left) or using accelerometer sensor-actuator pair (right)	53
4.8	The Bode plot (top) and the Nyquist plot (bottom 2 x 2 array) of the open loop FRF between the ideal velocity sensor and various size and thickness actuators; Case 1: 20x20mm 1.125mm (faint line, left top), Case 2: 30x30mm 0.5mm (dotted line, right top), Case 3: 40x40mm 0.28mm (dash-dotted line, left down), Case 4: 50x50mm 0.18mm (dashed line, right down)	55
4.9	The Bode plot (top) and the Nyquist plot (bottom 2 x 2 array) of the open loop FRF between the integrated signal of the accelerometer sensor and various size and thickness actuators; Case 1: 20x20mm 1.125mm (faint line, left top), Case 2: 30x30mm 0.5mm (dotted line, right top), Case 3: 40x40mm 0.28mm (dash-dotted line, left down), Case 4: 50x50mm 0.18mm (dashed line, right down)	56
4.10	Maximum vibration reduction at 1st(blue solid line), 4th (black dotted line), 8th (red dot dashed line), and 11th resonance (green dashed line) with reference to the size of the actuator using the ideal velocity sensor-actuator pair (left) or using accelerometer sensor-actuator pair (right)	57
4.11	The Bode plot (top) and the Nyquist plot (bottom 2 x 2 array) of the open loop FRF between the ideal velocity sensor and the actuator with various offset length; Case 1: no offset (faint line, left top), Case 2: 0.25mm offset(dotted line, right top), Case 3: 0.5mm offset (dash-dotted line, left down), Case 4: 1.0mm offset(dashed line, right down)	59
4.12	The Bode plot (top) and the Nyquist plot (bottom 2 x 2 array) of the open loop FRF between the ideal velocity sensor and the actuator with various offset length; Case 1: no offset (faint line, left top), Case 2: 0.25mm offset(dotted line, right top), Case 3: 0.5mm offset (dash-dotted line, left down), Case 4: 1.0mm offset(dashed line, right down)	60
4.13	Maximum vibration reduction at 1st(blue solid line), 4th (black dotted line), 8th (red dot dashed line), and 11th resonance (green dashed line) with reference to the offset length, using the ideal velocity sensor-actuator pair (left) or using accelerometer sensor-actuator pair (right)	61
C.1	Strain distribution; (a)unconstrained piezoelectric actuator(Top) and (b) bonded piezoelectric actuator on the panel (bottom)	79
C.2	Stress distribution (top) and its decomposition into passive (bottom left) and active stress (bottom right)	80

List of Tables

2.1	Geometric and physical properties of the smart panel	10
2.2	Geometric and physical properties of the the piezoelectric patch actuator	11
3.1	Geometric and physical properties of the accelerometer	39
4.1	Geometric parameter of the piezoelectric patch actuator considered in the parametric study regarding the actuator size	49
4.2	Geometric parameter of the piezoelectric patch actuator considered in the parametric study regarding the actuator thickness	53
4.3	Parameter of the actuator considered in the parametric study regarding the actuator size and thickness	57
4.4	Geometric parameter of the piezoelectric patch actuator considered in the parametric study regarding the offset length	61
A.1	Values for the constants G_x and H_x	67

Chapter 1

INTRODUCTION

1.1 Active Structural Acoustic Control

Over past decades noise and vibration effects on human beings have been regarded as significant problems and the regulations for the maximum acoustic and vibration levels have become more and more stringent. Especially for both land and air transportation vehicles, the control of vibration and sound transmission through lightly damped panels is an important issue, since it might result in discomfort.

In general, vibration and sound radiation control is achieved with passive treatments, which offer efficient results at high audio frequencies. However, passive approaches tend to have limited performance at low audio frequencies and require relatively bulky and heavy treatments[1]. Alternatively, at low audio frequencies, active vibration control techniques can be employed to reduce the sound radiation through thin structures. The low frequency response of lightly damped thin structures is characterized by well separated and sharp resonances. In the vicinity of resonance frequencies active damping control tends to be effective[1],[2]. Direct velocity feedback (DVFB) control is a simple way to implement active damping control[1],[3]. As schematically shown in Figure 1.1, when DVFB control is implemented, the control actuator exerts a control action directly proportional to the opposite of the velocity at the error sensor, thus it generates active damping.

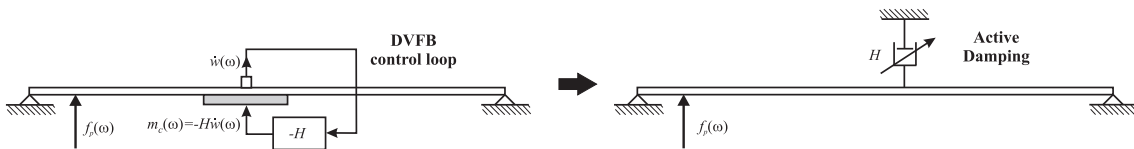


Figure 1.1: Smart panel with a piezoelectric patch actuator and a velocity sensor at its center for the implementation of a direct velocity feedback control loop that generates active damping

The principal issue of feedback control systems is stability, which is guaranteed if the sensor and actuator are collocated and dual. In this case the open loop sensor-actuator Frequency Response Function (FRF) is bound to be positive real and therefore the feedback control loop is unconditionally stable[1],[2], [4]-[6]. Thus large control gains could be implemented, which, in the case of velocity feedback, produce high levels of damping that reduces the response of the structure of sharp resonances at low frequency[1],[2], [4].

Elliott et al.[7] have proposed to use arrays of decentralized single channel velocity feedback control systems to generate active damping in panels. Their studies have shown that arrays of direct velocity feedback control systems can be efficiently operated to reduce both the low frequency vibration of the panel and its sound radiation or transmission. The use of control units with small piezoelectric patch actuators and accelerometer sensors at their centers has been considered in order to obtain compact and lightweight panels[8]-[10]. The velocity sensor detects the transverse vibration and the piezoelectric patch actuator exerts line moments along the edges[11], so that this control unit is neither collocated nor dual[5]. Thus, the plant responses of the decentralized control units are not guaranteed to be positive real at all frequencies[6]. As a result, the decentralized control loops are stable only for a limited range of control gains[2], [6]. This limits the generation of active damping on the structure and thus the vibration reduction and sound transmission[8]-[10]. It is therefore crucial to improve the collocation and duality properties of the velocity sensor and the piezoelectric patch actuator pair in order to develop more stable and robust feedback control loops, which produce the desired levels of active damping on smart panels.

1.2 Scope and Objectives

This report presents simulations and experimental results regarding the modeling of a smart panel, which consists of a rectangular panel with the dimensions $l_x \times l_y = 414\text{mm} \times 314\text{mm}$ and a single control unit. This control unit is composed of three main components: (1) an accelerometer sensor that detects out-of-plane acceleration, (2) a piezoelectric patch actuator that acts as the secondary controlling source, and (3) an analogue constant gain feedback controller, that connect the accelerometer sensor to the piezoelectric patch actuator. The piezoelectric transducer is bound on one sides of the panel, while the accelerometer sensor is attached on the other side in correspondence to the center of the actuator. The smart panel is mounted on a rigid frame positioned on the top open side of a rectangular cavity with thick rigid walls.

The three main objectives of this report are:

1. to build a mathematical model of smart panel, which separate the various effects of the local response of the sensor-actuator unit;
2. to validate the model by experiments;
3. to investigate the configuration of the control unit, which maximize the stability and performance of the control system.

In order to investigate the effects of the piezoelectric actuator and seismic accelerometer sensor transducers on the stability and control performance, practical detailed models are proposed instead of the standard simplified model with the ideal massless actuator and the ideal velocity sensor. In particular two fully coupled models are derived, which take into account: a) the passive mass and stiffness loading effects of the piezoelectric patch and b) the dynamic response and operational output signal of the accelerometer sensor in addition to the passive actuator effects. The open loop sensor-actuator FRF obtained with these two models are tested against experimental measurements in order to show the validity of the mathematical models. By using these two validated fully coupled models, an extensive parametric study is

carried out in order to achieve the third objective listed above. Both the Bode and the Nyquist plots of the open loop sensor-actuator FRFs are used to investigate the stability of the feedback loop, which is assessed with reference to Nyquist stability criterion. The performance of the control unit is investigated in term of the maximum vibration reduction at first few resonances. A simple formula is proposed, which gives these maximum vibration reductions at resonance frequencies from the Nyquist plot of the open loop sensor-actuator FRFs.

1.3 Structure of the Report

This report is divided into five chapters. Chapter 2 of this report briefly introduces the concept of smart panel with single sensor-actuator pair. Further on, the direct velocity feedback control (DVFB) method and the implementation of active damping on the smart panel are explained. The stability and control performance concepts are revised, and a simple formula for the calculus of the maximum vibration reduction at the error sensor with a stable loop is derived. Chapter 3 presents the formulation of the analytical models used to predict the response of the fully coupled plate and the piezoelectric patch. The predicted response of the plate with actuator and practical/ideal sensor is briefly introduced. The simulated results are compared with measured ones, and the validity of the numerical model is discussed. Chapter 4 presents a parametric study that highlights the effects of the size, thickness and bounding offset of the piezoelectric patch actuator on stability and control performance. This study verifies that stability properties can be significantly improved by modifying the geometric parameters of the actuator patch. Conclusions are given in Chapter 5.

Chapter 2

ACTIVE CONTROL AND STABILITY

The study presented in this report considers a rectangular thin aluminium panel with dimensions 414mm x 314mm and 1mm thickness. As shown in Figure 2.1, the panel is mounted on a rigid frame, which is positioned on the top open side of a rectangular cavity with rigid walls. This test rig has been designed in such a way to get sound radiation into the open space only from the top side of the panel. The plate is driven into motion by a shaker that generate point force f_p at the position $(x_p, y_p) = (62.1\text{mm}, 138.2\text{mm})$. It is assumed that the radiated acoustic sound pressure has no effect on the vibration of the panel. The geometry and physical properties of the plate are given in Table 2.1.

The panel is equipped with one feedback control unit that consists of a closely located accelerometer sensor and a square piezoelectric actuator. The piezoelectric actuator has a dimension of 25mm x 25mm x 0.5mm and is fixed on the inner side of the panel by a thin bonding layer of glue. The center position of the piezoelectric patch, where the error sensor is also located, is situated at $(x_c, y_c) = (136.6\text{mm}, 222.9\text{mm})$. The physical properties and geometry of the piezoelectric patch considered in this study are summarized in Table 2.2.

Table 2.1: Geometric and physical properties of the smart panel

parameter	value
Dimensions	$l_x \times l_y = 414\text{mm} \times 314\text{mm}$
Thickness	$h_s = 1\text{mm}$
Density	$\rho_s = 2700 \text{ kg/m}^3$
Young's Module	$E_s = 7.2 \times 10^9 \text{ N/m}^2$
Poisson's Ration	$\nu_s = 0.33$
Loss Factor	$\eta_s = 0.02$

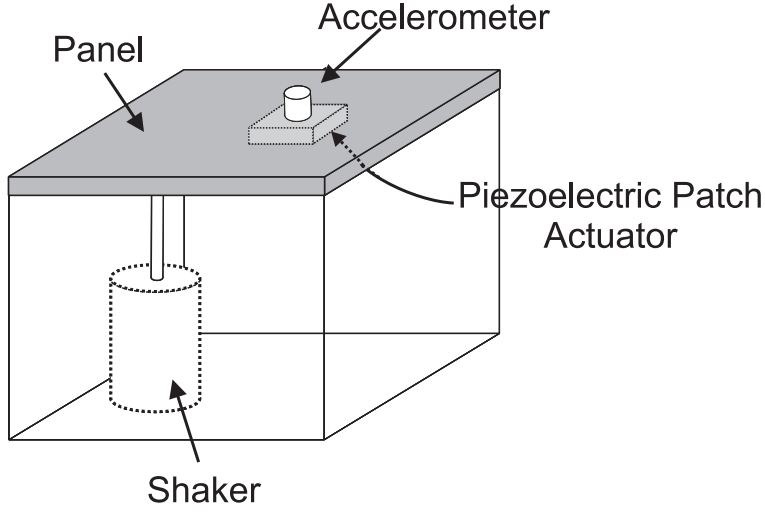


Figure 2.1: Physical arrangement of test rigs, which consist of an acoustic cavity with rigid walls and a baffled clamped smart panel, excited by a transverse point force generated by a shaker

Table 2.2: Geometric and physical properties of the the piezoelectric patch actuator

parameter	value
Dimensions	$a_x \times a_y = 25\text{mm} \times 25\text{mm}$
Thickness	$h_{pzt} = 0.5\text{mm}$
Center Position	$x_c \times y_c = 0.33l_x \times 0.71l_y$
Density	$\rho_{pzt} = 7600 \text{ kg/m}^3$
Young's Module	$E_{pzt} = 6.1 \times 10^9 \text{ N/m}^2$
Poisson's Ration	$\nu_{pzt} = 0.31$
Strain Constant	$d_{31} = 268 \times 10^{-12} \text{ m/V}$
Actuation Constant	$c_\alpha = 1.226 \times 10^{-3} \text{ N/V}$
Max. Operating Voltage	$c_m = 235 \times 10^3 \text{ V/m}$

2.1 DVFB Control

When the panel is excited by the primary excitation f_p and the control moments m_c , generated by an ideal massless piezoelectric actuator, the phasor of the velocity in z-direction at the sensor position \dot{w}_c can be written using the following mobility expression:

$$\dot{w}_c = Y_{cp}f_p + \mathbf{Y}_{cc}^p \mathbf{m}_c, \quad (2.1)$$

where Y_{cp} is the mobility function between the primary excitation and the velocity at the control sensor, and \mathbf{Y}_{cc}^p is a 4-element row vector with the mobility functions between the control moments along the edges of the actuator and the control velocity:

$$\mathbf{Y}_{cc}^p = [Y_{cx1} \quad Y_{cx2} \quad Y_{cy1} \quad Y_{cy2}]. \quad (2.2)$$

The derivation of the mobility functions is given in Appendix A, and the formula for the mobility functions used in this chapter are given in section 1 of Appendix B. In Eq.(2.1), \mathbf{m}_c denotes a 4-element column vector with the control moments generated by the piezoelectric patch along the four edges:

$$\begin{aligned} \mathbf{m}_c &= [m_{cx1} \quad m_{cx2} \quad m_{cy1} \quad m_{cy2}]^T \\ &= m_c [-1 \quad 1 \quad 1 \quad -1]^T \\ &= m_c \mathbf{d}, \end{aligned} \quad (2.3)$$

where m_{cx1} , m_{cx2} , m_{cy1} , and m_{cy2} are respectively the control moment along $y = y_{c1}$ between $x = (x_{c1}, x_{c2})$, and $y = y_{c2}$ between $x = (x_{c1}, x_{c2})$, $x = x_{c1}$ between $y = (y_{c1}, y_{c2})$, and $x = x_{c2}$ between $y = (y_{c1}, y_{c2})$, as shown in Figure 2.2. m_c denotes the magnitude of the effective bending moment per unit length, which is induced by the piezoelectric patch actuator to the panel. The effective moment m_c is proportional to the applied voltage across the piezoelectric actuator V_c ,

$$m_c = c_\alpha V_c, \quad (2.4)$$

where c_α is the piezoelectric constant given in Eq.(C.17). The details regarding the formulation of the effective actuation moments is presented in Appendix C.

The response at the error sensor generated by the primary excitation and the Direct Velocity FeedBack (DVFB) control loop can be formulated in terms of the classic disturbance rejection block diagram as shown in Figure 2.3. In this figure H denotes a constant feedback gain, and V_c denotes the input voltage signal to the piezoelectric actuator. When the DVFB control loop is implemented, the control voltage V_c is defined as follows:

$$V_c = -H\dot{w}_c. \quad (2.5)$$

Thus, the actuator induced moment m_c is given by:

$$m_c = c_\alpha V_c = -c_\alpha H\dot{w}_c. \quad (2.6)$$

Therefore, the velocity at the sensor location \dot{w}_c can be calculated as:

$$\dot{w}_c = \frac{Y_{cp}f_p}{1 + G_s H}, \quad (2.7)$$

where G_s denotes the transfer function between the error sensor and the piezoelectric actuator:

$$G_s = c_\alpha \mathbf{Y}_{cc}^p \mathbf{d}. \quad (2.8)$$

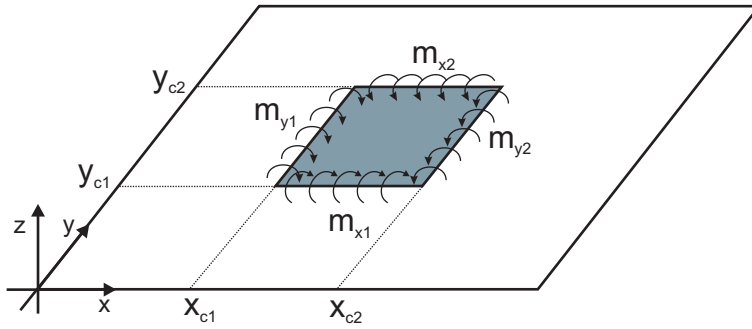


Figure 2.2: Moments excitation generated by a piezoelectric patch that is bonded on the bottom side of the panel, when the applied voltage has the same polarity as the poling voltage.

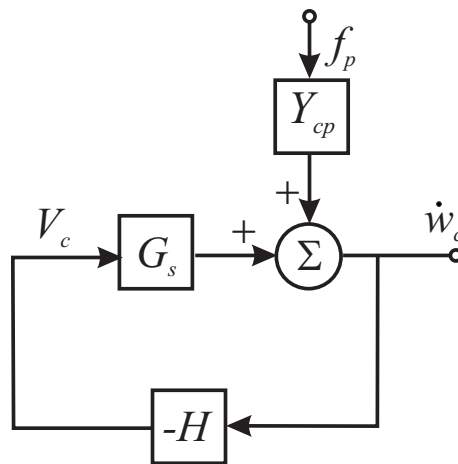


Figure 2.3: Block diagram of the direct velocity feedback control system

2.2 Open Loop Frequency Response Function

In feedback control loops, the control performance is strongly linked to the stability of the control loop. In principle, if the control loop is unconditionally stable, very high control gains can be implemented, such that a perfect cancelation can be generated at the control point. In contrast, when the system is only conditionally stable, a limited range of control gains can be implemented, which may lead to modest vibration reductions at the sensing position.

The stability of a control system is commonly assessed by the open loop sensor-actuator FRF, G_c , between the output signal from the velocity sensor \dot{w}_c and the input signal to the controller:

$$G_c = G_s H. \quad (2.9)$$

For proportional feedback control, the control function H is set to unity, $H = 1$. In this case, the open loop FRF is given by:

$$G_c = G_s = c_\alpha \mathbf{Y}_{cc}^p \mathbf{d}. \quad (2.10)$$

Figure 2.4 shows the Bode plot (left) and the Nyquist plot (right) of the predicted sensor-actuator open loop FRF G_c , assuming that the panel is simply supported along four edges. For the practical damping of the test rig considered in this study, the boundary condition can not be considered neither clamped or simply supported. At lower frequencies up to around 500Hz, the boundary condition is almost clamped on all four edges, and at higher frequencies from around 1kHz, the boundary condition is close to simply supported on all four edges. Therefore, since the stability analysis requires the analysis of the sensor-actuator open loop FRF up to very high frequencies, which means up to 50kHz in this study, the modeling has been carried out considering simply supported boundary condition.

The Bode plot in Figure 2.4 indicates that the amplitude of the sensor-actuator FRF grows when the frequency rises. This is a typical feature of moment-type excitation that is normally encountered with strain actuators[12]. The phase plot indicates that the phase is confined between ± 90 deg up to about 10kHz, and then a phase lag takes place. This effect is due to the non perfect collocation between the position of the error signal detection at the center of the piezoelectric patch and the bending control excitation at the edges of the piezoelectric patch.

The Nyquist plot in Figure 2.4 is characterized by a series of circles, which are determined by the resonant response of the modes of the plate. In low frequencies the locus starts from vicinity of the origin and moves in the right hand side quadrants. As the frequency rises, the locus tends to drift away from the origin. This is due to the residual effect from the resonant response of neighbor resonances. At low frequencies the modal density is low, so that the residual effect of the neighbor modes is negligible. As the plate modal overlap increases with frequency, the residual effect from the resonant response of neighbor resonances on the resonant response becomes more pronounced, and this effect shifts the locus away from the origin. At higher frequencies the locus enters and goes through the left hand side quadrants in a clockwise rotation. This drifting effect is caused by the phase lag generated by the non-perfect collocation between the sensor and the actuator pair.

The phase lag of the flexural waves Φ is given as the product of the circular frequency ω and the time delay t_b [12] it takes the bending waves, generated at the edges of the piezoelectric patch, to travel to its center position, at the error sensor location:

$$\Phi = \omega t_d = \frac{\omega d_s}{c_b}, \quad (2.11)$$

where c_b denotes the propagation speed of the flexural wave, and d_s denotes the distance between the error sensor and the edge of the patch actuator. As the sensor is situated at the center of the square patch, the distance is given as half of the patch length a :

$$d_s = \frac{a}{2}. \quad (2.12)$$

Assuming a single sine wave, the phase velocity of the flexural waves c_b is given by the following formula[13][14]:

$$c_b = \sqrt[4]{\frac{D_s}{\rho_s h_s}} \sqrt{\omega}, \quad (2.13)$$

where ρ_s is the density, and h_s is the thickness of the panel. D_s denotes the bending stiffness, which is given as the product of the module of elasticity E_s and the area moment of inertia per unit width, I_s :

$$I_s = \frac{h_s^3}{12}. \quad (2.14)$$

Thus, using Eq.(2.13), the phase lag Φ can be expressed as follows:

$$\Phi = \frac{a}{2} \sqrt{\omega} \sqrt[4]{\frac{\rho_s h_s}{D_s}}. \quad (2.15)$$

This equation indicates that the phase lag monotonically increases with reference to the square root of the circular frequency. The progressive phase lag of the open loop FRF brings the control system to a positive feedback velocity loop, rather than negative, so that the system becomes unstable.

Considering that the open loop FRF G_c is defined as the ratio between the velocity and the applied excitation, not between the the displacement and the excitation, the simulated phase of G_c is 90deg larger than the predicted phase lag given in Eq.(2.15), thus:

$$\Phi_c = \frac{a}{2} \sqrt{\omega} \sqrt[4]{\frac{\rho_s h_s}{D_s}} - \frac{\pi}{2}. \quad (2.16)$$

The predicted phase lag is plotted in Figure 2.4 by the dashed line, which follows the rough outline of the phase lag of the sensor-actuator open loop FRF.

As a summary, Figure 2.4 highlights the following conclusions.

1. A piezoelectric patch actuator efficiently excites higher frequency resonant modes.
2. As frequencies rises, the locus drifts away from the origin due to the residual effect from the resonant response of neighbor resonances.
3. The sensor-actuator open loop FRF is bound to be positive real only at low frequencies due to the phase lag, which is generated by the non-perfect collocation between the actuation moment along the perimeter of the actuator and the velocity sensing at the center of the actuator.

Thus, when large control gains are implemented there is a potential stability problem. Therefore it is likely that only a limited range of control gains can be implemented and thus rather small control effects are produced in practical systems with a closely located error sensor and the piezoelectric patch with direct velocity feedback control.

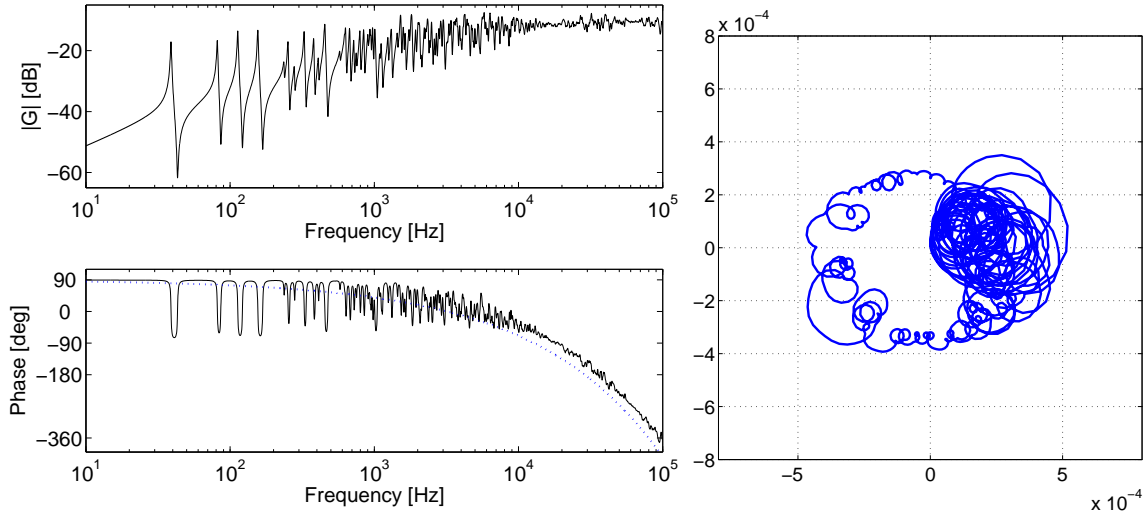


Figure 2.4: The Bode plot (left) and the Nyquist plot(right) of the open loop FRF of a closely located velocity sensor and a square piezoelectric actuator(solid line), and the predicted phase lag (dashed line)

2.3 Control Performance

As discussed in the introduction chapter of this report, the aim of velocity feedback is to generate active damping, which is particularly effective at resonance frequencies, where in fact the response of the structure is principally controlled by damping. The control performance of the feedback system at the k^{th} resonance frequency ω_k can be assessed in terms of a factor ρ_k , which is given by the ratio between absolute value of the the velocity phasor at the error sensor without control and with the maximum control gain H_{max} that guarantees the stability:

$$\begin{aligned}
 \rho_k &= \frac{|\dot{w}(\omega_k)_{max\ control}|}{|\dot{w}(\omega_k)_{no\ control}|} \\
 &= \frac{\left| \frac{Y_{cp}(\omega_k) f_p}{1 + H_{max} G_c(\omega_k)} \right|}{1} \frac{1}{|Y_{cp}(\omega_k) f_p|} \\
 &= \frac{1}{|1 + H_{max} G_c(\omega_k)|}.
 \end{aligned} \tag{2.17}$$

According to Nyquist stability criterion, the maximum control gain H_{max} is given by the reciprocal of δ_0 :

$$H_{max} = \frac{1}{\delta_0}, \tag{2.18}$$

where δ_0 denotes the absolute distance between the origin and the FRF, when the locus of the open loop sensor-actuator FRF crosses the real negative axis at the frequency ω_0 , as shown in the Nyquist plot in Figure 2.5:

$$\begin{aligned}
 \delta_0 &= |G_c(\omega_0)| \\
 &= -Re(G_c(\omega_0)).
 \end{aligned} \tag{2.19}$$

As discussed above, for low frequency resonances the locus-circles start from the origin and are aligned along the real positive axis. In this case, the amplitude of the FRF at ω_k can

be approximated by the amplitude δ_{rk} , where the k^{th} resonance circle crosses the real axis. Therefore, Eq.(2.17) can be simplified into the following formula:

$$\begin{aligned}
 \rho_k &\cong \frac{1}{1 + \frac{|G_c(\omega_k)|}{|G_c(\omega_0)|}} \\
 &= \frac{1}{1 + \frac{\delta_{rk}}{\delta_0}} \\
 &= \frac{1}{1 + \delta_{0k}},
 \end{aligned} \tag{2.20}$$

where $\delta_{0k} = \frac{\delta_{rk}}{\delta_0}$ denotes the ratio between the amplitude of the k^{th} resonance circle δ_{rk} and the maximum control gain δ_0 in the Nyquist plot of the open loop sensor-actuator FRF. The index of the maximum vibration reduction R_k that can be generated by the control loop is defined by the reciprocal of the indicator ρ_k in the unit of decibel:

$$\begin{aligned}
 R_k &= 20 \log_{10} \frac{1}{\rho_k} \\
 &= 20 \log_{10}(1 + \delta_{0k}).
 \end{aligned} \tag{2.21}$$

This equation gives the approximate index of the maximum vibration reduction R_k on the sensor location at the k^{th} resonance frequency. This formulation provides a simple approach to derive the control effectiveness at low frequency resonances based on either the predicted or measured open loop sensor-actuator FRF of the feedback control system. The index of the maximum vibration reduction R_k is plotted in Figure 2.6 for a range of ratios δ_{0k} from 0 to 3. This plot suggests that it is sufficient to have a ratio of 2 in order to obtain a 10 dB reduction of vibration at the error sensor position. This graph is of great importance since it can be used in combination with the Nyquist plot of the sensor-actuator FRF to assess both the stability and the control performance of a velocity feedback loop at resonance frequencies. In fact, it is sufficient to estimate the ratio δ_{0k} from the Nyquist plot of the open loop sensor-actuator FRF and then convert it into the maximum reduction index R_k using the plot in Figure 2.6.

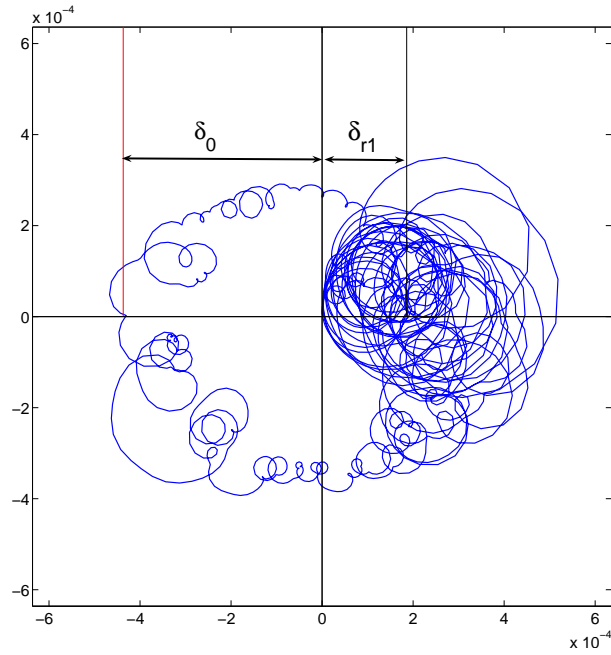


Figure 2.5: Definition of the stability coefficient (δ_0) and the control performance coefficient (δ_{rk})

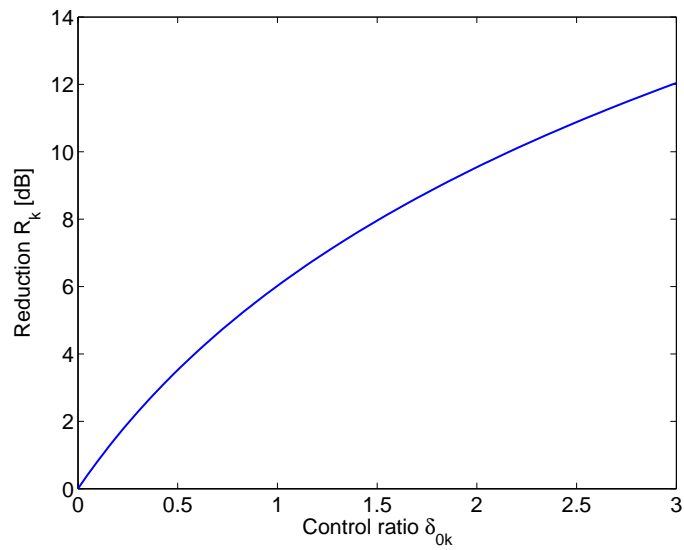


Figure 2.6: Maximum reduction index R_k with reference to the control ratio δ_{0k}

Chapter 3

MODEL PROBLEM

The mobility model considered in the previous chapter neglected several features of the control system, which can be summarized in the following points:

1. physical passive effects of the actuator and the sensor (mass and stiffness of the actuator, and mass of the sensor)
2. dynamic effects of the sensor (fundamental axial resonance)
3. offset effect due to the mounting method of the piezoelectric patch actuator

Intuitively, the compact and lightweight control system justifies these simplifications. However, it is crucial to investigate the effects of these physical properties on the stability in order to design a feasible actuator-sensor pair with good stability properties. In order to study and assess each effect independently, several models are considered in this chapter. Two fully coupled models are introduced, and these models are experimentally verified.

3.1 Actuator Mass Effect

In this section, the inertia effect of the piezoelectric patch actuator mass is modeled and analyzed. A simple model of this mass effect can be formulated by considering that the mass of the piezoelectric patch is concentrated at its center, where the control sensor is attached. Due to the linearity of the system, the phasor of the velocity at the error sensor \dot{w}_c can be expressed as follows:

$$\dot{w}_c = Y_{cp}f_p + \mathbf{Y}_{cc}^p \mathbf{m}_c + Y_{cm}f_m, \quad (3.1)$$

where Y_{cm} is the mobility function between the force generated by the inertia effect of the actuator f_m and the velocity at the error sensor. This force is derived from Newton's second law:

$$\begin{aligned} f_m &= -m_{pzt}\ddot{w}_c \\ &= -j\omega m_{pzt}\dot{w}_c, \end{aligned} \quad (3.2)$$

where m_{pzt} denotes the mass of the piezoelectric actuator. Using Eq.(3.2), Eq.(3.1) can be written as:

$$\dot{w}_c = Y_{cp}f_p + \mathbf{Y}_{cc}^p \mathbf{m}_c - j\omega m_{pzt}\dot{w}_c Y_{cm}$$

$$\begin{aligned}
&= \frac{Y_{cp}}{1 + j\omega m_{pzt} Y_{cm}} f_p + \frac{1}{1 + j\omega m_{pzt} Y_{cm}} \mathbf{Y}_{cc}^p \mathbf{m}_c \\
&= \tilde{Y}_{cp} f_p + \tilde{\mathbf{Y}}_{cc}^p \mathbf{m}_c.
\end{aligned} \tag{3.3}$$

Since the patch actuator is uniformly bonded to the panel, the single lumped mass model can not properly estimate the distributed inertia effect of actuator mass, especially at higher frequencies where the wavelength becomes closer to the patch side dimension. Therefore, instead of a single lumped mass model, a multiple lumped mass model is introduced. The actuator is modeled by a grid of rectangular elements as illustrated in Figure 3.1. The size of these elements has been chosen to be shorter than a quarter of the flexural wavelength at the maximum frequency considered in this study. According to the reference[13], the smallest flexural wavelength is $\lambda_{min}=13.8\text{mm}$ at a maximum frequency of 50kHz. Therefore, the actuator, with the dimension of 25mm x 25mm, has been subdivided into a grid of 8 x 8 elements, with the dimension 3.125mm x 3.125mm.

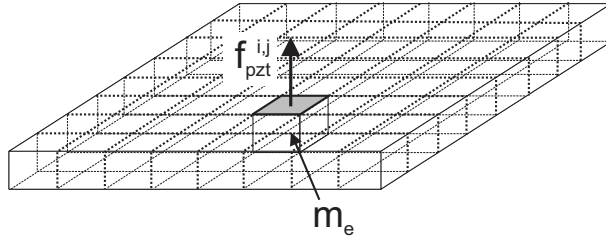


Figure 3.1: Schematic representation of distributed mass model

When inertia effect of the actuator mass is modeled by the multiple elements, the velocity at the sensor position \dot{w}_c is given as follows:

$$\dot{w}_c = Y_{cp} f_p + \mathbf{Y}_{cc}^p \mathbf{m}_c + \mathbf{Y}_{cm} \mathbf{f}_m, \tag{3.4}$$

where \mathbf{Y}_{cm} is a n_m^2 -element row vector with the mobility functions between the forces generated by the inertia effects of elemental masses and the control velocity. n_m is the number of the elements in x- and y-directions. \mathbf{f}_m is a n_m^2 -element column vector with the forces generated by inertia effects of lumped masses:

$$\begin{aligned}
\mathbf{f}_m &= \left[f_m^{1,1} \quad f_m^{1,2} \quad \dots \quad f_m^{i,j} \quad \dots \quad f_m^{n_m,n_m} \right]^T \\
&= -j\omega m_m \dot{\mathbf{w}}_m,
\end{aligned} \tag{3.5}$$

where $f_m^{i,j}$ represents the force due to inertia effect of i^{th} , j^{th} element, and m_m denotes the mass of each element. Assuming that the thickness of the patch is constant, and each element has the same dimension, the mass of each element is given by:

$$m_m = \frac{m_{pzt}}{n_m^2}. \tag{3.6}$$

In Eq.(3.5), $\dot{\mathbf{w}}_m$ is a n_m^2 -element column vector with the phasor of the velocities at the centers of the lumped masses:

$$\begin{aligned}
\dot{\mathbf{w}}_m &= \left[\dot{w}_m^{1,1} \quad \dot{w}_m^{1,2} \quad \dots \quad \dot{w}_m^{i,j} \quad \dots \quad \dot{w}_m^{n_m,n_m} \right]^T \\
&= \mathbf{Y}_{mp} f_p + \mathbf{Y}_{mc} \mathbf{m}_c + \mathbf{Y}_{mm} \mathbf{f}_m,
\end{aligned} \tag{3.7}$$

where $\dot{w}_m^{i,j}$ represents the phasor of the velocity of i^{th} , j^{th} element. \mathbf{Y}_{mp} is a n_m^2 -element column vector with the mobility functions between the primary excitation and the velocities at center of the elements. \mathbf{Y}_{mc} is a $n_m^2 \times 4$ matrix with the mobility functions between the control moments along the edges of the square patch actuator and the velocities at center of the element. \mathbf{Y}_{mm} is a $n_m^2 \times n_m^2$ matrix with the mobility functions between the forces generated by the inertia effect of the lumped masses and the velocities at the centers of the elements. Substituting Eq.(3.7) into Eq.(3.5), the force vector \mathbf{f}_m is given by:

$$\begin{aligned}\mathbf{f}_m &= -j\omega m_m (\mathbf{Y}_{mp} f_p + \mathbf{Y}_{mc} m_c + \mathbf{Y}_{mm} \mathbf{f}_m) \\ &= -j\omega m_m [\mathbf{I} + j\omega m_m \mathbf{Y}_{mm}]^{-1} (\mathbf{Y}_{mp} f_p + \mathbf{Y}_{mc} m_c),\end{aligned}\quad (3.8)$$

where \mathbf{I} denote a $n_m^2 \times n_m^2$ identity matrix. Substituting Eq.(3.8) into Eq.(3.4), the control velocity \dot{w}_c can be expressed as:

$$\dot{w}_c = \tilde{Y}_{cp} f_p + \tilde{\mathbf{Y}}_{cc}^p m_c, \quad (3.9)$$

where \tilde{Y}_{cp} and $\tilde{\mathbf{Y}}_{cc}^p$ are given below:

$$\tilde{Y}_{cp} = Y_{cp} - j\omega m_m \mathbf{Y}_{cm} [\mathbf{I} + j\omega m_m \mathbf{Y}_{mm}]^{-1} \mathbf{Y}_{mp} \quad (3.10)$$

$$\tilde{\mathbf{Y}}_{cc}^p = \mathbf{Y}_{cc}^p - j\omega m_m \mathbf{Y}_{cm} [\mathbf{I} + j\omega m_m \mathbf{Y}_{mm}]^{-1} \mathbf{Y}_{mc}. \quad (3.11)$$

Further details regarding the mobility functions used in this section are given in section 2 of Appendix B.

Figure 3.2 compares the simulated open loop FRF between the ideal sensor and the ideal massless piezoelectric actuator with the simulated open loop FRF between the ideal sensor and the lightweight piezoelectric actuator, in which case, G_c is given by:

$$G_c = c_\alpha \tilde{\mathbf{Y}}_{cc}^p \mathbf{d}. \quad (3.12)$$

The Bode plot in Figure 3.2 indicates that the mass effect becomes important at high frequencies. When the frequency is higher than 5kHz, the phase lag of the FRF with mass effect becomes bigger than phase lag of the FRF without mass effect. At frequencies higher than 10kHz, the difference in phase lag between the two FRFs is almost constant, that is approximately given by 90deg. The inertia effect tends to pull down the amplitude of the FRF in proportion to ω . Therefore, when the mass effect of the patch actuator is considered, the amplitude of the FRF is smaller than that of the open loop FRF between an ideal sensor and ideal actuator, particularly at high frequencies, where the open loop FRF enters the left half of the Nyquist plot. As a result, the Nyquist plot of the sensor-actuator open loop FRF is more squeezed towards the imaginary axis, as shown in Figure 3.2. Therefore, the stability is improved and hence the control system can be operated with a larger control gain. In conclusion, inertia brings a beneficial effect that improves the stability of a feedback control loop.

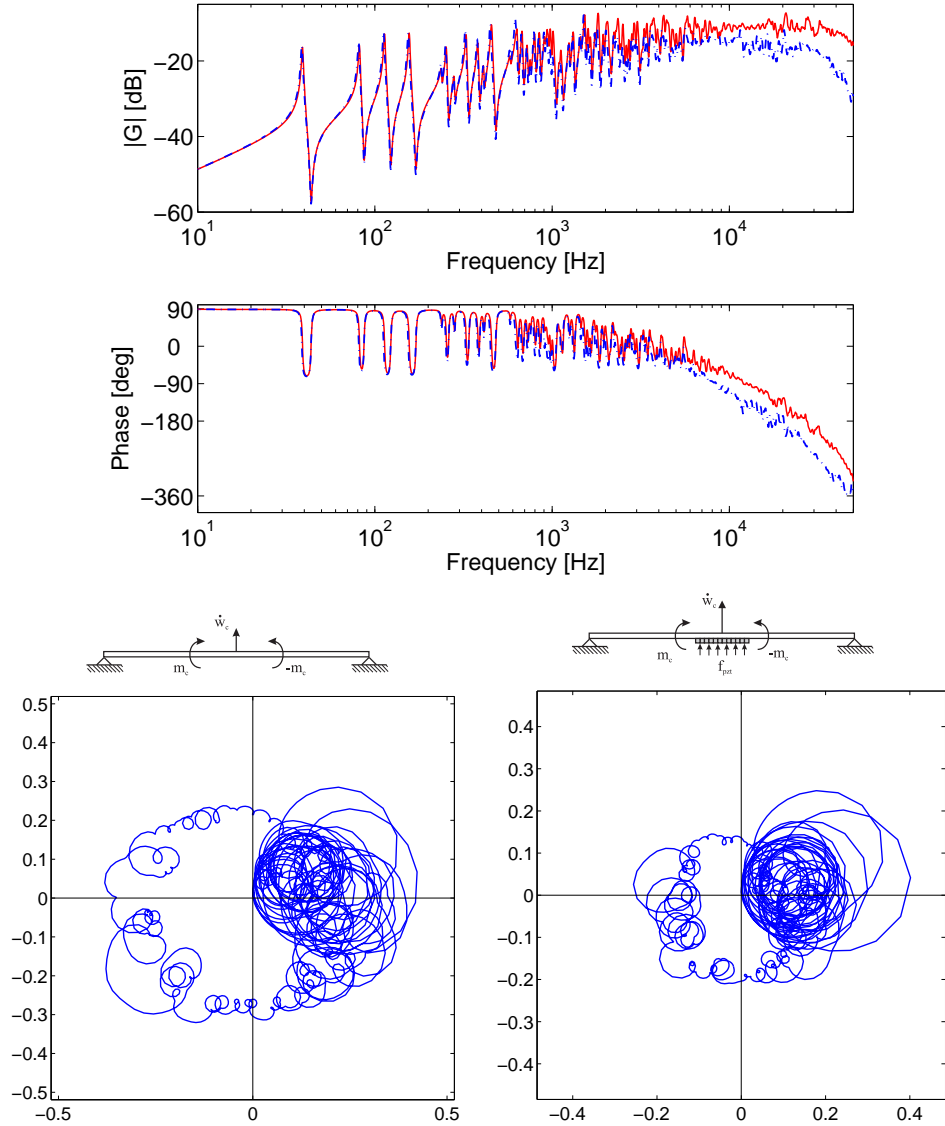


Figure 3.2: The Bode plot (top) and the Nyquist plot (bottom 1 by 2 array) of the open loop FRF between the ideal velocity sensor and either the massless piezoelectric actuator (faint line, left), or the lightweight piezoelectric actuator (dotted line, right)

3.2 Actuator Stiffness Effect

When the actuator is bonded to the panel, the patch locally increases the stiffness of the structure. In this section the passive elastic effect of the piezoelectric patch actuator is modeled and analyzed. At first, in order to simply assess this passive effect of the actuator, the patch actuator is modeled by a single pair of linear springs, as shown in Figure 3.3. Due to the linearity, when the stiffness of the patch actuator is taken into account, the phasor of the velocity at the error sensor can be expressed as:

$$\dot{w}_c = Y_{cp} f_p + \mathbf{Y}_{cM} \mathbf{M}_t, \quad (3.13)$$

where \mathbf{Y}_{cM} denotes a 4-element row vector with the mobility functions between the moments acting on the edges of the patch actuator and the control velocity. \mathbf{M}_t denotes a 4-element column vector with the moments generated by the piezoelectric actuation and the elastic effect of the lumped springs:

$$\mathbf{M}_t = \begin{bmatrix} M_{x1} & M_{x2} & M_{y1} & M_{y2} \end{bmatrix}^T, \quad (3.14)$$

where M_{x1} , M_{x2} , M_{y1} , and M_{y2} are the total moments generated along $y = y_{c1}$ between $x = (x_{c1}, x_{c2})$, and $y = y_{c2}$ between $x = (x_{c1}, x_{c2})$, $x = x_{c1}$ between $y = (y_{c1}, y_{c2})$, and $x = x_{c2}$ between $y = (y_{c1}, y_{c2})$, respectively. When the piezoelectric patch actuator is modeled by a single pair of springs, the total line moments along the edges are concentrated at $(\frac{x_{c1}+x_{c2}}{2}, y_{c1})$, $(\frac{x_{c1}+x_{c2}}{2}, y_{c2})$, $(x_{c1}, \frac{y_{c1}+y_{c2}}{2})$, and $(x_{c2}, \frac{y_{c1}+y_{c2}}{2})$, respectively.

The discretized total moment acting on the panel \mathbf{M}_t is defined as the summation of the discretized effective control actuation moment \mathbf{M}_c and discretized passive moment generated by the elastic effect of the actuator patch \mathbf{M}_k :

$$\mathbf{M}_t = \mathbf{M}_c + \mathbf{M}_k, \quad (3.15)$$

where \mathbf{M}_c is a 4-element column vector:

$$\mathbf{M}_c = m_c \begin{bmatrix} -a_x & a_x & a_y & -a_y \end{bmatrix}^T, \quad (3.16)$$

where a_x and a_y are respectively the length of the actuator in x- and y-directions. Considering the coordinate system defined in Figure 3.4, the vector \mathbf{M}_k with the passive moment on the

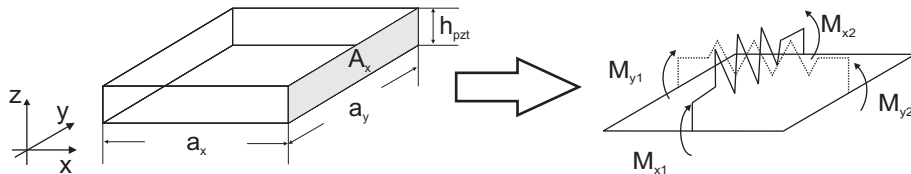


Figure 3.3: Schematic representation of the actuator stiffness model with single pair of springs

panel is given by the following formula:

$$\mathbf{M}_k = -\mathbf{M}_{pzt}^k = \begin{pmatrix} a_x \int_{-\frac{h_s}{2}-h_{pzt}}^{-\frac{h_s}{2}} \sigma_{pzt,y1}^k z dz \\ a_x \int_{-\frac{h_s}{2}-h_{pzt}}^{-\frac{h_s}{2}} \sigma_{pzt,y2}^k z dz \\ -a_y \int_{-\frac{h_s}{2}-h_{pzt}}^{-\frac{h_s}{2}} \sigma_{pzt,x1}^k z dz \\ -a_x \int_{-\frac{h_s}{2}-h_{pzt}}^{-\frac{h_s}{2}} \sigma_{pzt,x2}^k z dz \end{pmatrix} \quad (3.17)$$

where h_s and h_{pzt} are respectively the thickness of the panel and the piezoelectric patch. $\sigma_{pzt,y1}^k$, $\sigma_{pzt,y2}^k$, $\sigma_{pzt,x1}^k$, and $\sigma_{pzt,x2}^k$ are respectively the stress within the piezoelectric patch along $y = y_{c1}$ between $x = (x_{c1}, x_{c2})$, and $y = y_{c2}$ between $x = (x_{c1}, x_{c2})$, $x = x_{c1}$ between $y = (y_{c1}, y_{c2})$, and $x = x_{c2}$ between $y = (y_{c1}, y_{c2})$, which is generated by the passive elastic effect of the actuator. Since a stress is defined as the force perpendicular to the cross section divided by the cross sectional area, the applied moment can be given by using the force applied on the piezoelectric actuator along the edge of the patch, as shown Figure 3.4. Thus, Eq.(3.17) is rewritten as follows:

$$\mathbf{M}_k = \begin{pmatrix} \frac{a_x}{A_{py}} \int_{-\frac{h_s}{2}-h_{pzt}}^{-\frac{h_s}{2}} F_{ky1} z dz \\ \frac{a_x}{A_{py}} \int_{-\frac{h_s}{2}-h_{pzt}}^{-\frac{h_s}{2}} F_{ky2} z dz \\ -\frac{a_y}{A_{px}} \int_{-\frac{h_s}{2}-h_{pzt}}^{-\frac{h_s}{2}} F_{kx1} z dz \\ -\frac{a_y}{A_{px}} \int_{-\frac{h_s}{2}-h_{pzt}}^{-\frac{h_s}{2}} F_{kx2} z dz \end{pmatrix}, \quad (3.18)$$

where F_{k1} and F_{k2} are give by:

$$\begin{aligned} F_{k1} &= k_{pzt}(s_1 - s_2) \\ F_{k2} &= k_{pzt}(s_2 - s_1), \end{aligned} \quad (3.19)$$

where k_{pzt} denote the axial stiffness of the piezoelectric patch. When the elastic effect of the piezoelectric patch is modeled by one pair of springs, the spring coefficient k_{pzt} is given as:

$$k_{pzt}^x = \frac{E_{pzt} A_{px}}{a_x} \quad (3.20)$$

$$k_{pzt}^y = \frac{E_{pzt} A_{py}}{a_y}, \quad (3.21)$$

where E_{pzt} denotes the elastic module of the piezoelectric patch, and A_{px} and A_{py} denote the section area of the actuator normal to x- and y-directions, as shown in Figure 3.3:

$$A_{px} = a_y h_{pzt} \quad (3.22)$$

$$A_{py} = a_x h_{pzt}, \quad (3.23)$$

In Eq.(3.19), s_1 and s_2 denote the displacement along the edge of the patch. Considering the coordinate and sign notation defined in Figure 3.4, these terms can be expressed with reference to the rotation angles of the plate and the distance between the middle plane of the panel and that of the patch, represented by z :

$$\begin{aligned} s_{x1} &= z \tan \theta_{y1} \\ s_{x2} &= z \tan \theta_{y2} \\ s_{y1} &= -z \tan \theta_{x1} \\ s_{y2} &= -z \tan \theta_{x2}. \end{aligned} \quad (3.24)$$

Assuming that the rotation angles are small, the above formulas can be simplified as follows:

$$\begin{aligned} s_{x1} &= z\theta_{y1} \\ s_{x2} &= z\theta_{y2} \\ s_{y1} &= -z\theta_{x1} \\ s_{y2} &= -z\theta_{x2}, \end{aligned} \quad (3.25)$$

in which case, the force F_k is given as follows:

$$\begin{aligned} F_{kx1} &= zk_{pzt}^x(\theta_{y1} - \theta_{y2}) \\ F_{kx2} &= zk_{pzt}^x(\theta_{y2} - \theta_{y1}) \\ F_{ky1} &= -zk_{pzt}^y(\theta_{x1} - \theta_{x2}) \\ F_{ky2} &= -zk_{pzt}^y(\theta_{x2} - \theta_{x1}). \end{aligned} \quad (3.26)$$

After integration of Eq.(3.18), the vector with discretized total moment \mathbf{M}_t can be expressed:

$$\mathbf{M}_t = -\mathbf{C}_k \dot{\boldsymbol{\theta}} + \mathbf{M}_c, \quad (3.27)$$

where \mathbf{C}_k is a 4×4 matrix with the stiffness coefficients:

$$\mathbf{C}_k = \begin{bmatrix} c_{kx} & -c_{kx} & 0 & 0 \\ -c_{kx} & c_{kx} & 0 & 0 \\ 0 & 0 & c_{ky} & -c_{ky} \\ 0 & 0 & -c_{ky} & c_{ky} \end{bmatrix}, \quad (3.28)$$

and c_{kx} and c_{ky} are stiffness coefficients regarding the elastic effect of the patch in x- and y-directions:

$$c_{kx} = \frac{k_{pzt}^y}{12j\omega} (4h_{pzt}^2 + 6h_s h_{pzt} + 3h_s^2) \quad (3.29)$$

$$c_{ky} = \frac{k_{pzt}^x}{12j\omega} (4h_{pzt}^2 + 6h_s h_{pzt} + 3h_s^2). \quad (3.30)$$

In Eq.(3.27), $\dot{\boldsymbol{\theta}}$ represents a 4-element column vector with the angular velocities along the edges of the patch actuator:

$$\begin{aligned} \dot{\boldsymbol{\theta}} &= \begin{bmatrix} \dot{\theta}_{x1} & \dot{\theta}_{x2} & \dot{\theta}_{y1} & \dot{\theta}_{y2} \end{bmatrix}^T \\ &= \mathbf{Y}_{\theta p} f_p + \mathbf{Y}_{\theta M} \mathbf{M}_t, \end{aligned} \quad (3.31)$$

where $\dot{\theta}_{x1}$, $\dot{\theta}_{x2}$, $\dot{\theta}_{y1}$, and $\dot{\theta}_{y2}$ are the angular velocities at $\left(\frac{x_{c1}+x_{c2}}{2}, y_{c1}\right)$, $\left(\frac{x_{c1}+x_{c2}}{2}, y_{c2}\right)$, $\left(x_{c1}, \frac{y_{c1}+y_{c2}}{2}\right)$, and $\left(x_{c2}, \frac{y_{c1}+y_{c2}}{2}\right)$, respectively. $\mathbf{Y}_{\theta p}$ is a 4-element row vector with the mobility functions between the primary excitation at (x_p, y_p) and the angular velocities at the edges of the patch actuator. $\mathbf{Y}_{\theta M}$ represents a 4×4 matrix with the mobility functions between the discretized total moments and the angular velocities at the edges of the patch actuator. Substituting Eq.(3.31) into Eq.(3.27), the discretized total moment vector \mathbf{M}_t is given by:

$$\mathbf{M}_t = -[\mathbf{I} + \mathbf{C}_k \mathbf{Y}_{\theta M}]^{-1} \mathbf{C}_k \mathbf{Y}_{\theta p} f_p + [\mathbf{I} + \mathbf{C}_k \mathbf{Y}_{\theta M}]^{-1} \mathbf{M}_c. \quad (3.32)$$

Substituting Eq.(3.32) into Eq.(3.13), the complex velocity at the control position \dot{w}_c is expressed as:

$$\dot{w}_c = \tilde{\mathbf{Y}}_{cp} f_p + \tilde{\mathbf{Y}}_{cM} \mathbf{M}_c, \quad (3.33)$$

where $\tilde{\mathbf{Y}}_{cp}$ and $\tilde{\mathbf{Y}}_{cM}$ are defined below:

$$\tilde{\mathbf{Y}}_{cp} = \mathbf{Y}_{cp} - \mathbf{Y}_{cM} [\mathbf{I} + \mathbf{C}_k \mathbf{Y}_{\theta M}]^{-1} \mathbf{C}_k \mathbf{Y}_{\theta p} \quad (3.34)$$

$$\tilde{\mathbf{Y}}_{cM} = \mathbf{Y}_{cM} [\mathbf{I} + \mathbf{C}_k \mathbf{Y}_{\theta M}]^{-1}. \quad (3.35)$$

Since the patch is in practice a distributed system, a single pair of springs is not sufficient to model the actuator induced bending moment. Therefore, instead of single pair of springs, the actuator has been modeled with n_k pairs of springs as shown in Figure 3.5. When the elastic effect of the patch actuator is modeled by n_k pairs of springs, the phasor of the control velocity \dot{w}_c is given by the same formula as Eq.(3.13), however in this case \mathbf{Y}_{cM} is a $4n_k$ -element row vector with the mobility functions between the elemental moments and the control velocity. The discretized total moment vector \mathbf{M}_t is defined by a similar formula as Eq.(3.27):

$$\begin{aligned} \mathbf{M}_t &= [\mathbf{M}_{x1} \quad \mathbf{M}_{x2} \quad \mathbf{M}_{y2} \quad \mathbf{M}_{y1}]^T \\ &= -\mathbf{C}_k \dot{\boldsymbol{\theta}} + \mathbf{M}_c, \end{aligned} \quad (3.36)$$

where in this case \mathbf{C}_k is a $4n_k \times 4n_k$ matrix:

$$\mathbf{C}_k = \begin{bmatrix} \frac{c_{kx}}{n_k} \mathbf{I} & -\frac{c_{kx}}{n_k} \mathbf{I} & \mathbf{0} & \mathbf{0} \\ -\frac{c_{kx}}{n_k} \mathbf{I} & \frac{c_{kx}}{n_k} \mathbf{I} & \mathbf{0} & \mathbf{0} \\ \mathbf{0} & \mathbf{0} & \frac{c_{ky}}{n_k} \mathbf{I} & -\frac{c_{ky}}{n_k} \mathbf{I} \\ \mathbf{0} & \mathbf{0} & -\frac{c_{ky}}{n_k} \mathbf{I} & \frac{c_{ky}}{n_k} \mathbf{I} \end{bmatrix}, \quad (3.37)$$

where \mathbf{I} is a $n_k \times n_k$ identity matrix, and c_{kx} and c_{ky} are stiffness coefficients, defined in Eq.(3.29) and Eq.(3.30). \mathbf{M}_c is a $4n_k$ -element row vector with the control moments:

$$\begin{aligned} \mathbf{M}_c &= \frac{m_c}{n_k} [-a_x \mathbf{K} \quad a_x \mathbf{K} \quad a_y \mathbf{K} \quad -a_y \mathbf{K}]^T \\ &= \frac{m_c}{n_k} \mathbf{D}_a, \end{aligned} \quad (3.38)$$

where \mathbf{K} is a n_k dimension row vector consisting of 1:

$$\mathbf{K} = [1 \quad 1 \quad \cdots \quad 1]. \quad (3.39)$$

In Eq.(3.36), $\dot{\boldsymbol{\theta}}$ denotes a $4n_k$ -element column vector with the angular velocities along the edges of the patch. The formula for $\dot{\boldsymbol{\theta}}$ is already given in Eq.(3.13), however in this case $\mathbf{Y}_{\theta p}$ is a $4n_k$ -element row vector with the mobility functions between the primary excitation at (x_p, y_p) and the angular velocity of the elements at the edges of the patch actuator. $\mathbf{Y}_{\theta M}$ represents a $4n_k \times 4n_k$ matrix with the mobility functions between the discretized total moments and the angular velocities of the elements at the edges of the patch. According to Eq.(3.13), Eq.(3.36), and Eq.(3.31), when the multiple pairs of springs are taken into account, the control velocity \dot{w}_c is given by the same formula as the single pair of springs is considered, as given in Eq.(3.33). Details regarding the mobility functions used in this section are given in section 3 of Appendix B.

Figure 3.6 compares the simulated open loop FRF between the ideal sensor and the ideal actuator with the simulated open loop FRF between the ideal sensor and the elastic actuator, in which case G_c is given by:

$$G_c = \frac{c_\alpha}{n_k} \tilde{\mathbf{Y}}_{cM} \mathbf{D}_a. \quad (3.40)$$

Figure 3.6 highlights that the amplitude of sensor-actuator FRF using the stiffness-coupled model is slightly lower than that of the ideal model at low frequencies. This is due to the fact that the distributed elastic effect of the patch locally increases the stiffness of the smart panel at low frequencies. Although this plot shows the passive stiffness effect of the actuator is small, Eq.(3.29) and Eq.(3.30) indicate that the stiffness coefficient c_s is proportional to the thickness cubed, so that the passive moment generated by the stiffness effect of the actuator effectively increases as the thickness of the actuator increases. Thus, it is expected that the difference between the two FRFs increases as the thickness of the actuator grows. However, the magnitude of the actuation moment m_c , given in Eq.(C.17), is also a function of actuator thickness h_{pzt} . Therefore, it is important to compare the magnitude of the active moment with that of the passive moment, with reference to the actuator thickness in order to design an actuator that can generate a stronger control moment.

Figure 3.7 compares the actuation moment with the total moment at 1st resonant frequency, around 39Hz. The left hand side plot shows the moment per unit length, per unit voltage. This plot highlights that the actuation moment m_c increases with reference to the thickness up to $h_{pzt} \simeq 0.4\text{mm}$, and then starts decreasing. This is due to the fact that the static actuation strength of the piezoelectric actuator decreases because of its static stiffness effect. Similarly, the total moment m_t increases with reference to the thickness up to $h_{pzt} \simeq 0.2\text{mm}$, beyond which the total moment also starts decreasing. Furthermore, while the actuator is thin, the total moment is just slightly smaller than the active moment. However, as the thickness of the actuator increases, the difference between the two moments grows. This indicates that the passive moment generated by the stiffness of the patch actuator increases, as thickness rises.

The right hand side plot in Figure 3.7 shows the moment per unit length with the maximum operating voltage V_{max} , which can be applied to the actuator without impairing piezoelectric functionality. This term is given as a product of a constant c_m and the thickness of the actuator:

$$V_{max} = c_m h_{pzt}. \quad (3.41)$$

This plot highlights that, when the maximum operating voltage is considered, the total moment generated by the active and passive effects of the piezoelectric patch actuator increase with reference to the thickness up to $h_{pzt} = 0.86\text{mm}$. In this case the maximum operating

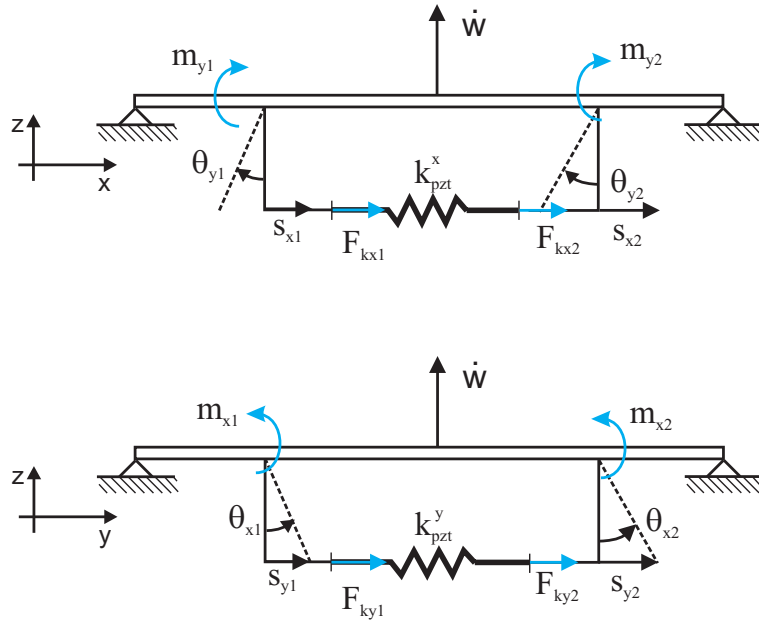


Figure 3.4: Schematic representation of the lumped spring model of the actuator patch with the notation of the forces and displacements at the connecting points between the lumped spring and the smart panel in x-direction (top) and y-direction (bottom)

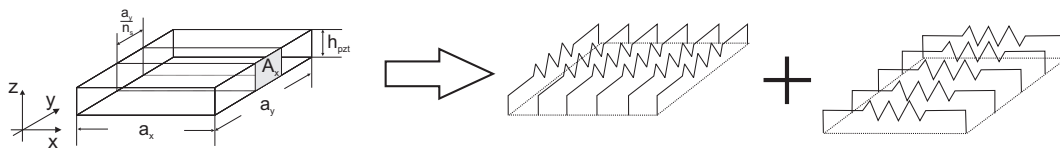


Figure 3.5: Schematic representation of the actuator stiffness model with multiple pairs of springs

voltage is $V_{max} \simeq 200V$, which is in the range of standard voltages to operate the piezoelectric patch actuator. If the feedback control system allows a large feedback gain, which implies a high control signal close to the maximum operating voltage of the piezoelectric actuator, the maximum operating voltage must be considered to define the desired thickness of the actuator.

In conclusion, the increase of the actuator thickness brings beneficial effects only up to a certain limit. Excessive increase beyond that limit results in decreasing the total induced moment.

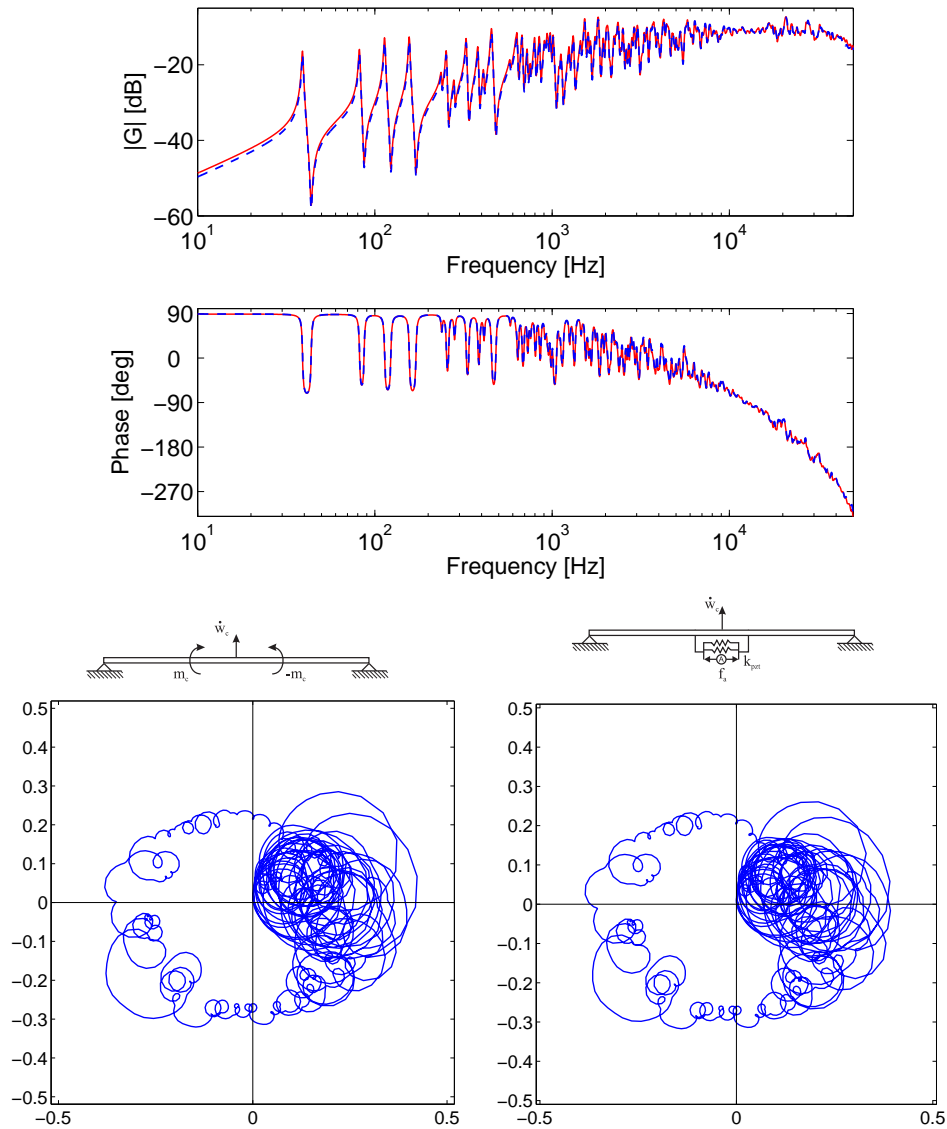


Figure 3.6: The Bode plot (top) and the Nyquist plot (bottom 1 by 2 array) of the open loop FRF of the ideal velocity sensor and the piezoelectric actuator without (faint line, left) and with (dotted line, right) stiffness effect of the piezoelectric actuator

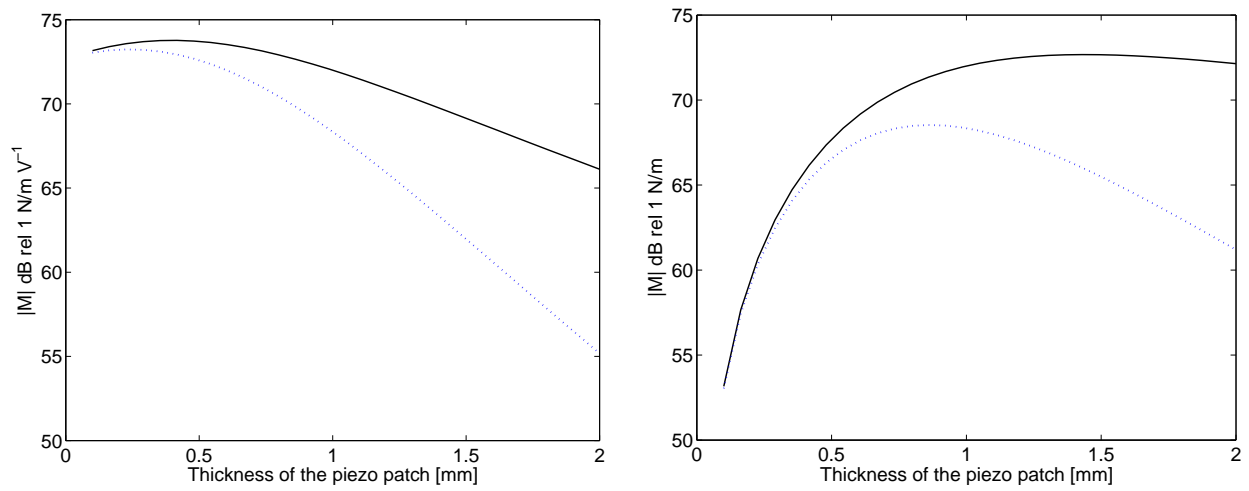


Figure 3.7: Actuation moment (solid black line) and total moment including the stiffness effect of the actuator patch (blue dotted line) without(left) and with(right) the factor of the maximum operating voltage

3.3 Actuator-Panel Fully Coupled Model

In this section a fully coupled model of the panel and the actuator is considered. This model includes both the mass effect and elastic effect of the piezoelectric patch actuator considered in the previous two sections. In this case the velocity at the sensing position \dot{w}_c is given as a function of the primary excitation f_p , the inertia effect of the actuator mass \mathbf{f}_m , and the induced moment generated by the piezoelectric and elastic effects of the patch actuator \mathbf{M}_t . Thus the velocity can be formulated by the following mobility matrix expression:

$$\dot{w}_c = Y_{cp}f_p + \mathbf{Y}_{cm}\mathbf{f}_m + \mathbf{Y}_{cM}\mathbf{M}_t, \quad (3.42)$$

where \mathbf{Y}_{cm} is a n_m^2 -element row vector with the mobility functions between the forces generated by the inertia effects of the elemental masses and the control velocity, given in Eq.(B.11). \mathbf{Y}_{cM} is a $4n_k$ -element row vector with the mobility functions between the discretized moment and the control velocity, given in Eq.(B.25). \mathbf{f}_m is a n_m^2 -element column vector with the force generated by the inertia effects of the actuator, given in Eq.(3.8), and \mathbf{M}_t denotes a $4n_k$ -elements row vector with the discretized total moments produced along the four edges of the piezoelectric patch actuator, given in Eq.(3.36)

The angular velocities of the plate in correspondence to the actuator springs are grouped into the $4n_k$ -element row vector $\dot{\boldsymbol{\theta}}$, and the velocities of the plate in correspondence to the centers of the actuator mass elements are grouped into the n_m^2 -element row vector $\dot{\mathbf{w}}_m$. These two vectors are defined as a function of the primary excitation f_p , the force vector generated by the inertia effect of the actuator mass, represented by \mathbf{f}_m , and the discretized total moment vector induced by the control actuation and the elastic effect of the actuator, represented by \mathbf{M}_t :

$$\dot{\boldsymbol{\theta}} = \mathbf{Y}_{\theta p}f_p + \mathbf{Y}_{\theta m}\mathbf{f}_m + \mathbf{Y}_{\theta M}\mathbf{M}_t \quad (3.43)$$

$$\dot{\mathbf{w}}_m = \mathbf{Y}_{mp}f_p + \mathbf{Y}_{mm}\mathbf{f}_m + \mathbf{Y}_{mM}\mathbf{M}_t, \quad (3.44)$$

where $\mathbf{Y}_{\theta p}$ is a $4n_k$ -element row vector with the mobility functions between the primary excitation and the angular velocities in correspondence to the actuator springs, given in Eq.(B.31). \mathbf{Y}_{mp} is a n_m^2 -element column vector with the mobility functions between the primary excitation and the velocities at the center of the mass elements, given in Eq.(B.15). \mathbf{Y}_{mm} is a $n_m^2 \times n_m^2$ matrix with the mobility functions between the forces generated by the inertia effect of the lumped masses and the velocities at the center of the mass elements, given in Eq.(B.22). $\mathbf{Y}_{\theta M}$ is a $4n_k \times 4n_k$ matrix with the mobility functions between the discretized total moments and the angular velocities along the edges of the patch in correspondence to the actuator springs, given in Eq.(B.36). $\mathbf{Y}_{\theta m}$ is a $4n_k \times n_m^2$ matrix with the mobility functions between the discretized angular velocities in correspondence to the actuator springs and the forces generated by the inertia effect of the lumped masses, and \mathbf{Y}_{mM} is a $n_m^2 \times 4n_k$ matrix with the mobility functions between the elemental velocities and the discretized total moments in correspondence to the actuator springs. Further details regarding $\mathbf{Y}_{\theta m}$ and \mathbf{Y}_{mM} are given in section 4 of Appendix B. After some algebraic manipulation, the control velocity \dot{w}_c can be expressed as follows:

$$\dot{w}_c = \tilde{Y}_{cp}f_p + \tilde{\mathbf{Y}}_{cM}\mathbf{M}_c. \quad (3.45)$$

where \tilde{Y}_{cp} and $\tilde{\mathbf{Y}}_{cM}$ are given in Appendix B.

Figure 3.8 compares the open loop FRF between the ideal sensor and actuator with the open loop FRF between the ideal sensor and lightweight elastic actuator, in which case G_c is given by:

$$G_c = c_\alpha \widetilde{Y}_{cM} D_a. \quad (3.46)$$

At low frequencies, the amplitude of the open loop FRF predicted using the fully coupled model is slightly lower than that of the FRF predicted using ideal sensor actuator model, due to the actuator stiffness effect. At higher frequencies, the inertia effect of actuator mass tends to pull down the amplitude and increases the phase lag of the open loop FRF predicted using the fully coupled model.

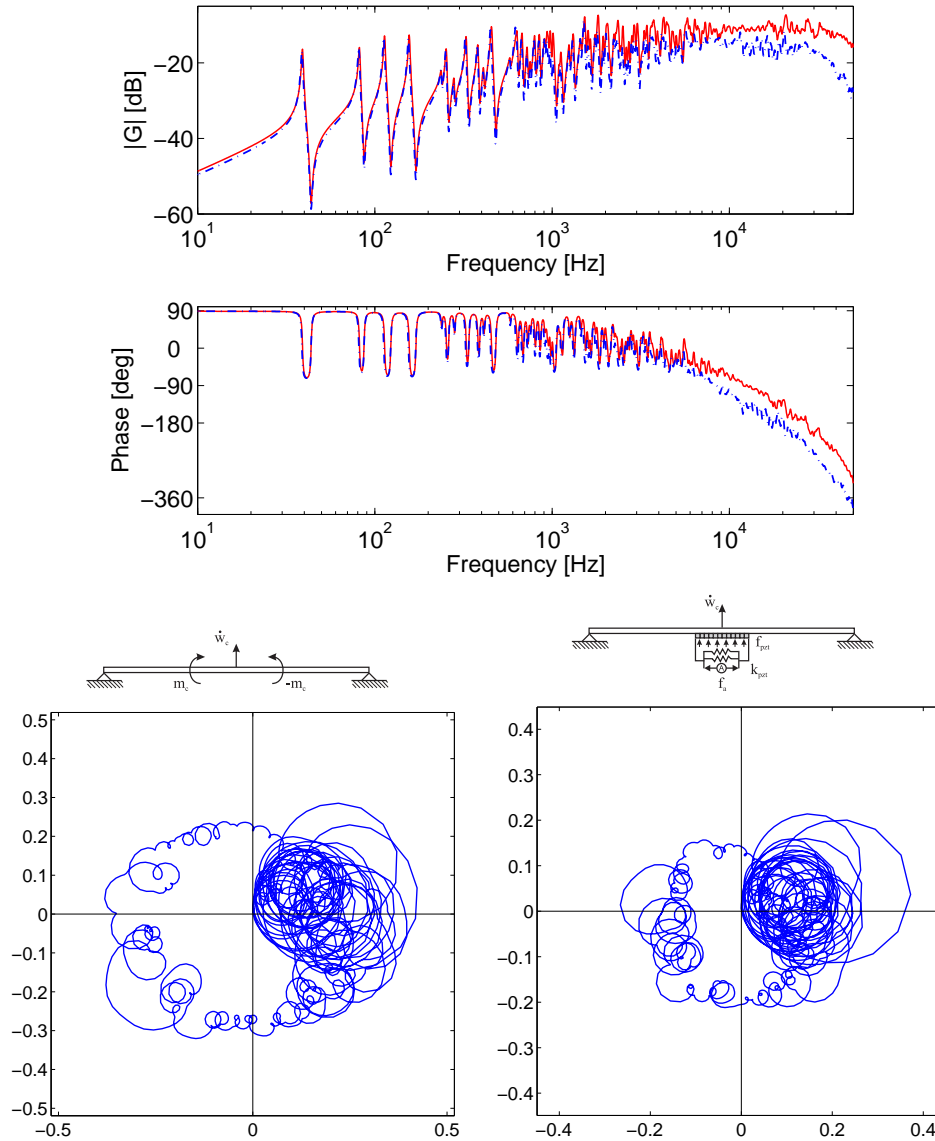


Figure 3.8: The Bode plot (top) and the Nyquist plot (bottom 1 by 2 array) of the open loop FRF between the ideal velocity sensor and the piezoelectric actuator without (faint line, left) and with (dotted line, right) inertia and elastic effects of the piezoelectric actuator

3.4 Sensor-Actuator Fully Coupled Model

The stability analysis presented in the previous sections considered a practical actuator with an ideal sensor. In this section the passive dynamic effect of a practical accelerometer sensor is taken into account. Accelerometers are sensing transducers, which provide an output proportional to acceleration, vibration, and shock. Piezoelectric accelerometers are one of the most popular sensing transducers, as piezoelectric materials have the ability to output an electrical signal proportional to the applied stress. In this study, tri-shear mode accelerometers, shown in Figure 3.9, are considered. A tri-shear accelerometer consists of seismic masses, base, piezoelectric material, preloaded ring, and a center post. Shear mode accelerometers sandwich the sensing material between a center post and the seismic mass. A compression ring or stud applies a preload force to create a rigid linear structure. Under acceleration, the mass applies a shear stress to the sensing material. The result is an electrical output that is collected by the electrodes and transmitted by lightweight lead wires to the built-in signal conditioning circuitry. By isolating the sensing crystals from the base and housing, shear mode accelerometers excel in rejecting thermal transient and base-strain effects. Furthermore, the shear geometry's small size promotes high-frequency response while minimizing mass loading effects on the test structure.

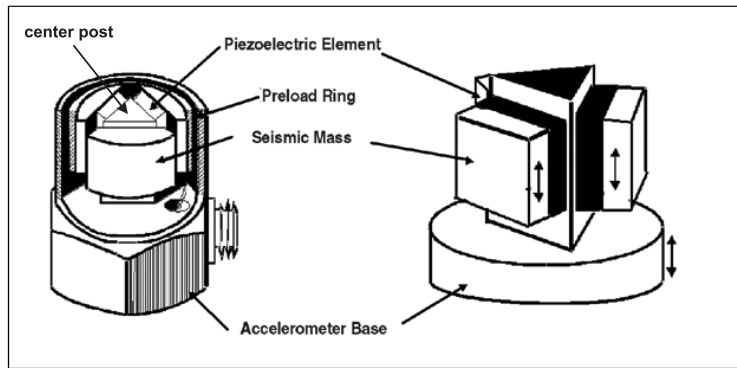


Figure 3.9: Internal structure of tri-shear piezoelectric sensing accelerometer 352C67

3.4.1 Sensor dynamics

When a shear accelerometer is considered, as a first approximation the piezoelectric elements act as a spring with a stiffness k_a and dashpot c_a , and connect the base of the accelerometer to the seismic masses. The sensor operates on Newton's second law of motion: $F = m_a a$. An input at the base of the accelerometer creates a force, F , on the piezoelectric material proportional to the applied acceleration, a , and size of the seismic mass, m_a . The frequency response of the sensor is determined by the resonant frequency, which can be modeled as a simple single-degree-of-freedom system, as shown in Figure 3.10, where k_a represents the stiffness constant, and c_a represents the damping coefficient of the piezoelectric element. As the piezoelectric element is made out of high density material, the mass of the spring is not negligible. m_a denotes the summation of the seismic mass and part of the piezoelectric element mass. The mass of the other components of the accelerometer is collectively represented by the housing mass m_h .

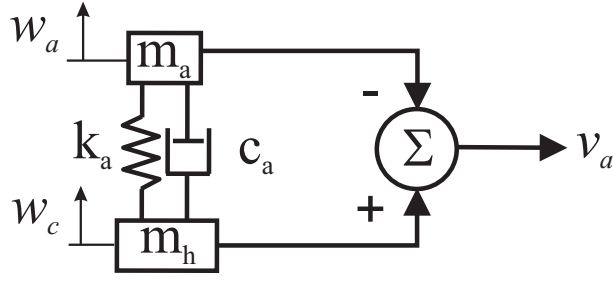


Figure 3.10: Schematic representation of the piezoelectric accelerometer transducer, which is modeled as a single degree-of-freedom system

Under the base motion, the sensor generates a voltage signal v_a , which is proportion to the relative displacement between the seismic mass and the base mass:

$$v_a = c_\sigma(w_c - w_a), \quad (3.47)$$

where c_σ is the detection constant of the piezoelectric elastic element, and w_a and w_c are the time harmonic displacement of the seismic mass and base mass, respectively. Since the accelerometer is firmly fixed to the smart panel, the base of the accelerometer, illustrated in Figure 3.10, has the vibratory displacement of the plate.

According to Newton's second law, the equation of motion for this single degree of freedom system is given by the following expression:

$$m_a \ddot{w}_a = c_a(\dot{w}_c - \dot{w}_a) + k_a(w_c - w_a), \quad (3.48)$$

or

$$(\ddot{w}_c - \ddot{w}_a) + 2\zeta_a \omega \omega_a (\dot{w}_c - \dot{w}_a) + \omega_a^2 (w_c - w_a) = -\ddot{w}_c, \quad (3.49)$$

where ω_a is the natural frequency of the single degree of freedom system, and ζ_a represents the viscous damping factor:

$$\omega_a = \sqrt{\frac{k_a}{m_a}} \quad (3.50)$$

$$\zeta_a v = \frac{c_a}{2\sqrt{k_a m_a}}. \quad (3.51)$$

Normally, the natural frequency of seismic actuators varies between 35kHz and 50kHz. In this study, the possible highest natural frequency, 50kHz, is used as a representative value.

The given data sheet of the accelerometer used in the experiments presented in this report does not cover all the required information in order to model the accelerometer as a single-degree-of-freedom mass-damper system. The following parameters are not listed in the given data sheet; 1) viscous damping factor ζ_a , 2) damping factor c_a , and 3) spring coefficient k_a . In order to calculate these parameters, it is sufficient to determine viscous damping ratio ζ_a , as these three parameters are dependent on each other according to the following formulas:

$$k_a^2 = m_a^2 \omega_a^4, \quad (3.52)$$

$$c_a = 2\omega_a m_a \zeta_a. \quad (3.53)$$

According to the manufacturer, the seismic mass is approximately $0.6g$. Considering the given structure schematics, the mass of the piezoelectric element can not be larger than $0.3g$. Assuming that one third of spring mass contributes to the proof mass [22], the inertia mass m_a is set to be $0.7g$. The viscous damping factor ζ_a is set to be 0.05 , which is in the range of standard values for piezoelectric elements. When the variables discussed above are given, the spring coefficient k_a and damping factor c_a can be calculated. The physical properties of the single degree of freedom system are shown in Table 3.1.

Assuming a harmonic excitation, the following equation is derived from Eq.(3.49):

$$(-\omega^2 + j\zeta_a\omega\omega_a + \omega_a^2)(w_c - w_a) = \omega^2 w_c. \quad (3.54)$$

According to Eq.(3.47) and Eq.(3.54), the transfer function between the complex acceleration of the plate $\ddot{w}_c(\omega)$ and the signal output from the sensor $v_a(\omega)$ is given by:

$$\begin{aligned} \frac{v_a}{\ddot{w}_c} &= \frac{c_\sigma(w_c - w_a)}{-\omega^2 w_c} \\ &= c_\sigma \frac{-\frac{1}{\omega_a^2}}{1 - \frac{\omega^2}{\omega_a^2} + 2j\zeta_a \frac{\omega}{\omega_a}}. \end{aligned} \quad (3.55)$$

When the harmonic frequency ω is much smaller than the natural frequency ω_a , the module of the transfer function is approximately constant, and the phase angle is approximately zero. Therefore, as shown in Figure 3.11, while the frequency of the harmonic excitation is below the resonance frequency of the accelerometer, the output voltage of the accelerometer sensor v_a is proportional to the opposite of the acceleration at its base:

$$v_a \cong -\frac{c_\sigma}{\omega_a^2} \ddot{w}_c. \quad (3.56)$$

Eq.(3.56) shows that the output signal is proportional to the reciprocal of the squared natural frequency. It indicates that if the frequency range of the operation rises, i.e. the resonance frequency of the accelerometer sensor rises, the sensitivity of the sensor is reduced.

In order to implement Direct Velocity Feedback (DVFB) in the control loop, an integrator is used which provides the velocity as the error signal to the controller. With time harmonic excitation, the integration can be expressed by the reciprocal of $j\omega$, so that the accelerometer with integrator provides the following control voltage \hat{v}_a :

$$\hat{v}_a = \frac{c_\sigma}{j\omega} (w_c - w_a). \quad (3.57)$$

Eq.(3.57) can be grouped into the following matrix form:

$$\begin{aligned} \hat{v}_a &= \frac{c_\sigma}{j\omega} \mathbf{d}_c \mathbf{w} \\ &= -\frac{c_\sigma}{\omega^2} \mathbf{d}_c \dot{\mathbf{w}}, \end{aligned} \quad (3.58)$$

where $\dot{\mathbf{w}}$ is a 2-element column vector with the velocity of the plate at the control position \dot{w}_c and that of the inertia mass in the accelerometer sensor \dot{w}_a :

$$\dot{\mathbf{w}} = \begin{Bmatrix} \dot{w}_c \\ \dot{w}_a \end{Bmatrix}. \quad (3.59)$$

\mathbf{d}_c is a 2-element row vector given below:

$$\mathbf{d}_c = [1 \quad -1]. \quad (3.60)$$

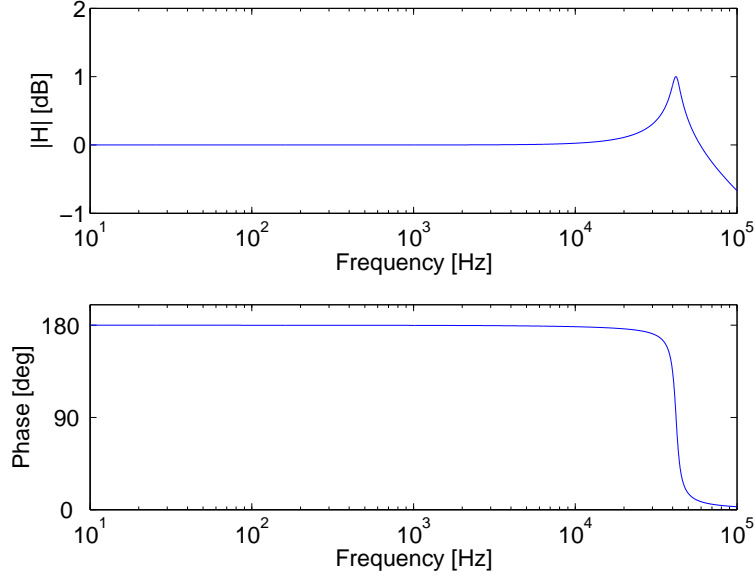


Figure 3.11: Transfer function between the acceleration of the panel at the sensor position and the voltage signal output of the accelerometer

3.4.2 Fully coupled model

In this section the open loop FRF is derived by taking into account the response of an accelerometer sensor modeled as a suspended mass with spring and dashpot. In this case, the velocity at sensor location \dot{w}_c is given by the following matrix expression:

$$\dot{w}_c = Y_{cp}f_p + \mathbf{Y}_{cm}\mathbf{f}_m + \mathbf{Y}_{cM}\mathbf{M}_t + Y_{cc}(f_{a1} + f_h), \quad (3.61)$$

where Y_{cc} is the mobility function between the collocated point force and the velocity at the control position, where the accelerometer is fixed. f_h represents the inertia effect of the housing mass of the accelerometer, and f_{a1} is the reaction force of the seismic mass of the accelerometer, transmitted via the elastic piezoelectric elements. f_h and f_{a1} are simply modeled as a single lumped mass acting at (x_c, y_c) . Figure 3.12 illustrates details regarding the displacement and forces acting on the elements of the accelerometer, which is mounted on the plate at the center of the piezoelectric patch actuator. Since the displacement of housing mass is corresponding to that of the plate, the force generated by inertia effect of the housing mass f_h is given as:

$$f_h = -j\omega m_h \dot{w}_c. \quad (3.62)$$

In Eq.(3.61), the force generated by the inertia effect of the actuator \mathbf{f}_m is given in Eq.(3.8) as a function of the velocity at the centers of lumped elements. \mathbf{M}_t is given in Eq.(3.32) as a

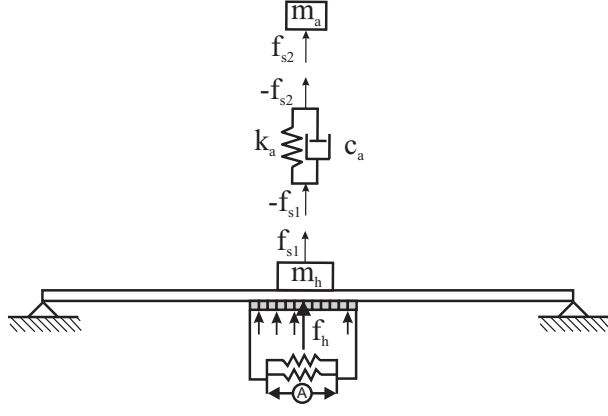


Figure 3.12: Schematic representation of a piezoelectric accelerometer transducer, and the notation of the forces and displacement at the connecting points between the elements of the accelerometer and the smart panel

function of the angular velocity along the edges of the patch in correspondence to the spring elements $\dot{\theta}$.

When the dynamics effect of the sensor is taken into account, the vectors of the elemental velocities $\dot{\mathbf{w}}_e$ and the angular velocities $\dot{\theta}$ are given by:

$$\dot{\mathbf{w}}_m = \mathbf{Y}_{mp}f_p + \mathbf{Y}_{mm}\mathbf{f}_m + \mathbf{Y}_{mM}\mathbf{M}_t + \mathbf{Y}_{mc}(f_{a1} + f_h), \quad (3.63)$$

$$\dot{\theta} = \mathbf{Y}_{\theta p}f_p + \mathbf{Y}_{\theta m}\mathbf{f}_m + \mathbf{Y}_{\theta M}\mathbf{M}_t + \mathbf{Y}_{\theta c}(f_{a1} + f_h), \quad (3.64)$$

where \mathbf{Y}_{mc} is a n_m^2 -element column vector with the mobility functions between the point force on the plate generated by the dynamics effect of the accelerometer acting at the sensing point and the velocities at the center of the actuator mass elements. $\mathbf{Y}_{\theta c}$ is a $4n_k$ -element column vector with the mobility functions between the point force generated by the dynamics effect of the accelerometer acting at the sensing point and the angular velocities along the edges of the patch in correspondence to the actuator springs. Details regarding the mobility functions \mathbf{Y}_{mc} and $\mathbf{Y}_{\theta c}$ are given in section 5 of Appendix B. After some algebraic manipulations, the velocity of the plate at sensor's position \dot{w}_c can be written as a function of the primary excitation f_p , reaction force of the accelerometer sensor f_{a1} and the control moment \mathbf{M}_c :

$$\dot{w}_c = \tilde{Y}_{cp}f_p + \tilde{Y}_{cM}\mathbf{M}_c + \tilde{Y}_{cc}f_{a1}. \quad (3.65)$$

where \tilde{Y}_{cp} , \tilde{Y}_{cM} and \tilde{Y}_{cc} are given in Appendix B.

The reaction force of the accelerometer f_{a1} is identical to the force applied on the inertia mass f_{a2} with opposite sign:

$$f_{a1} = -f_{a2}. \quad (3.66)$$

The force applied to the inertia mass f_{a2} was already given in Eq.(3.48):

$$\begin{aligned} f_{a2} &= m_a\ddot{w}_a \\ &= c_a(\dot{w}_c - \dot{w}_a) + \frac{k_a}{j\omega}(\dot{w}_c - \dot{w}_a) \\ &= \left(c_a + \frac{k_a}{j\omega} \right) (\dot{w}_c - \dot{w}_a). \end{aligned} \quad (3.67)$$

The velocity of the seismic mass \dot{w}_a is given using the mobility term:

$$\dot{w}_a = \frac{1}{j\omega m_a} f_{a2} = Y_{aa} f_{a2}. \quad (3.68)$$

Eq.(3.65) and Eq.(3.68) can be grouped in a matrix form as follows:

$$\begin{Bmatrix} \dot{w}_c \\ \dot{w}_a \end{Bmatrix} = \dot{\mathbf{w}} = \mathbf{Y}_a \mathbf{f}_a + \mathbf{Y}_p f_p + \mathbf{Y}_M \mathbf{M}_c, \quad (3.69)$$

where the 2×2 matrix \mathbf{Y}_a , the 2-element column vector \mathbf{Y}_p , and the $2 \times 4n_k$ matrix \mathbf{Y}_M are given as follows:

$$\mathbf{Y}_a = \begin{bmatrix} \tilde{Y}_{cc} & 0 \\ 0 & Y_{aa} \end{bmatrix} \quad (3.70)$$

$$\mathbf{Y}_p = \begin{bmatrix} \tilde{Y}_{cp} \\ 0 \end{bmatrix} \quad (3.71)$$

$$\mathbf{Y}_M = \begin{bmatrix} \tilde{\mathbf{Y}}_{cM} \\ 0 \end{bmatrix}, \quad (3.72)$$

and \mathbf{f}_a is a 2-element column vector that consists of the forces acting on the seismic mass and base mass:

$$\mathbf{f}_a = \begin{bmatrix} f_{a1} \\ f_{a2} \end{bmatrix}. \quad (3.73)$$

Using Eq.(3.66) and Eq.(3.67), the force vector \mathbf{f}_a is derived in terms of the following impedance relation:

$$\mathbf{f}_a = \mathbf{Z}_a \dot{\mathbf{w}}, \quad (3.74)$$

where the impedance matrix \mathbf{Z}_a is given as:

$$\mathbf{Z}_a = \begin{bmatrix} \frac{k_a}{j\omega} + c_a & -\frac{k_a}{j\omega} - c_a \\ -\frac{k_a}{j\omega} - c_a & \frac{k_a}{j\omega} + c_a \end{bmatrix}. \quad (3.75)$$

Substituting Eq.(3.74) into Eq.(3.69), and solving the equation with respect to $\dot{\mathbf{w}}$ leads to the following result:

$$\begin{aligned} \dot{\mathbf{w}} &= [\mathbf{I} + \mathbf{Y}_a \mathbf{Z}_a]^{-1} (\mathbf{Y}_p f_p + \mathbf{Y}_M \mathbf{M}_c) \\ &= \tilde{\mathbf{Y}}_p f_p + \tilde{\mathbf{Y}}_M \mathbf{M}_c, \end{aligned} \quad (3.76)$$

where \mathbf{I} denote a 2×2 identity matrix, and $\tilde{\mathbf{Y}}_p$ and $\tilde{\mathbf{Y}}_M$ are given by:

$$\tilde{\mathbf{Y}}_p = [\mathbf{I} + \mathbf{Y}_a \mathbf{Z}_a]^{-1} \mathbf{Y}_p \quad (3.77)$$

$$\tilde{\mathbf{Y}}_M = [\mathbf{I} + \mathbf{Y}_a \mathbf{Z}_a]^{-1} \mathbf{Y}_M \quad (3.78)$$

Substituting Eq.(3.76) and Eq.(3.38) into Eq.(3.58), the open loop sensor-actuator FRF G_c between the integrated output signal voltage from the accelerometer sensor \hat{v}_a and the input signal voltage to the piezoelectric actuator V_c is given as:

$$G_c = \frac{\hat{v}_a}{V_c} = -\frac{c_\alpha c_\sigma}{n_k \omega^2} \mathbf{d}_c \tilde{\mathbf{Y}}_M \mathbf{D}_a. \quad (3.79)$$

Figure 3.13 shows the Bode plot of the open loop sensor-actuator FRF using the actuator-plate (solid line) and actuator-plate-sensor (dotted line) fully coupled models. At low frequencies, below about 8kHz, the sensor-actuator FRF derived with the actuator-plate-sensor fully coupled model is very similar to that of the actuator-plate model. In fact, up to 3kHz, the FRFs are characterized by an alternating sequence of resonances and anti-resonances, so that the phase is constrained between 90deg. Above 3kHz the modal density of the plate is so high that the FRFs are characterized by a smoother curve. The mean value of the FRF tends to raise with the frequency. This is a typical feature of strain actuators, which is due to the fact that the piezoelectric patch generates bending moments on the plate along the four edges of the patch itself and thus better excites the plate as the flexural wavelength approaches or becomes smaller than the size of the actuator, i.e. at higher frequencies. The FRFs are also characterised by a constant phase lag, which is due to the non perfect collocation between the position of the error signal detection at the centre of the piezoelectric patch and the bending control excitation at the edges of the piezoelectric patch [15].

At high frequencies, above 10kHz, the FRF of the actuator-plate-sensor coupled model is characterized by a constant amplitude roll off and additional phase lag followed by a wide frequency band peak with a 180deg phase lag. The amplitude roll off is due to the mass effect introduced by the accelerometer. Also, the extra peak and 180deg phase lag are caused by the resonance of the accelerometer which, according to the given parameter of the sensor considered here, has been calculated at about 50kHz. The simulated FRF shows this resonance peak at 54.8kHz due to the fully coupled response of the plate and accelerometer sensor.

Table 3.1: Geometric and physical properties of the accelerometer

Parameter	value
Total mass	$m_{ta} = 2.0$ [g]
Inertia mass	$m_a = 0.6(0.7)$ [g]
Stiffness	$k_a = 59.22 \times 10^6$ [N/m]
Viscous damping	$\zeta_a = 0.05$
Damping	$c_a = 18.85$ [Nsec/m]
Natural frequency	$\omega_a = 50$ [kHz]

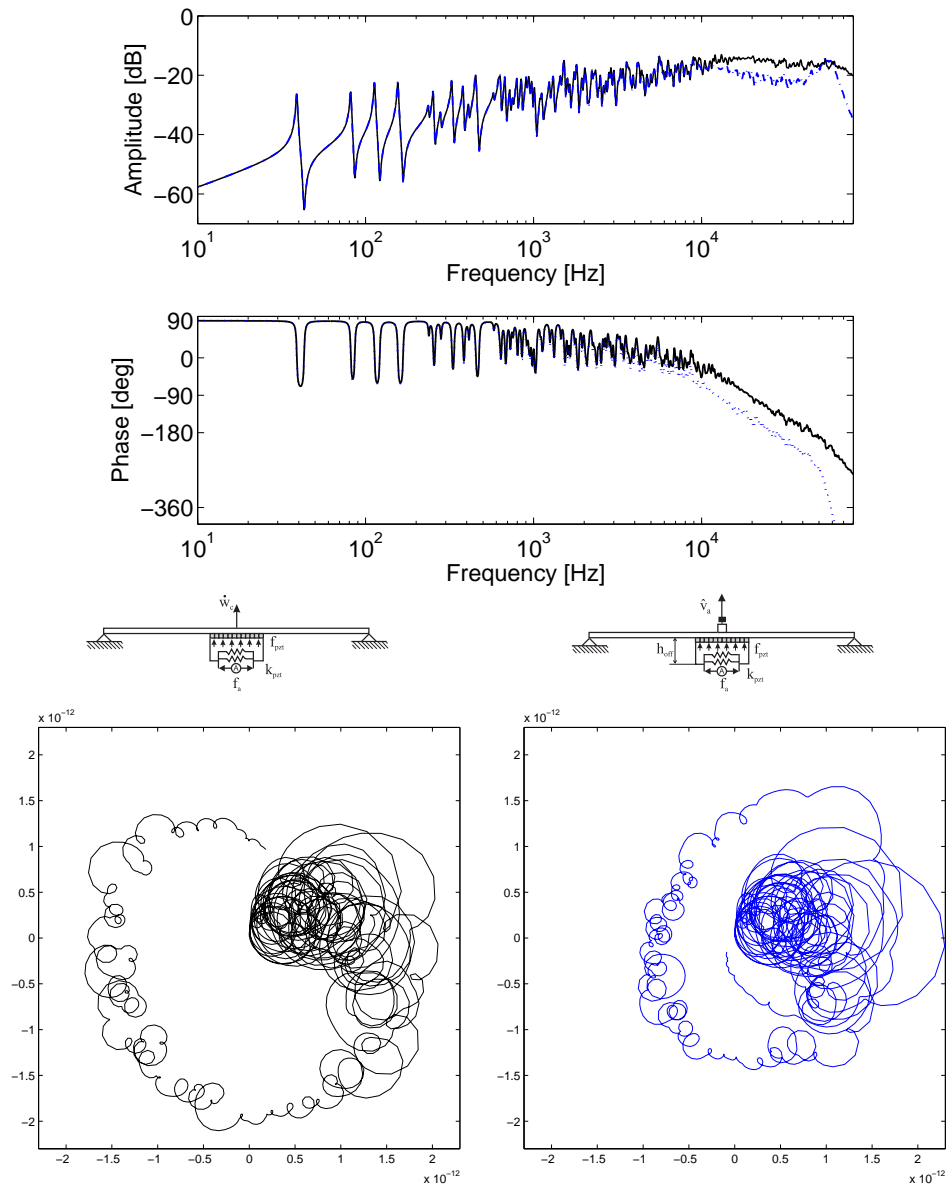


Figure 3.13: The Bode plot (top) and the Nyquist plot (bottom, 1 by 2 array) of the open loop FRF between the ideal accelerometer sensor and the practical piezoelectric actuator (faint line), the open loop FRF between the integrated signal from the accelerometer sensor and the practical piezoelectric actuator (dotted line, right)

3.5 Models Validation

In this section the two simulated open loop frequency response functions using

1. actuator-plate fully coupled model, discussed in section 3.3, and
2. actuator-plate-accelerometer fully coupled model, discussed in section 3.4

are compared with experimental measured open loop FRFs, which are obtained by either using a remote sensing system (laser vibrometer), or an accelerometer. For the measurements, the panel is clamped on a rigid frame, which is placed on the top of a rectangular wooden box with thick rigid walls. The accelerometer sensor is positioned at the center of the square actuator on the opposite side of the panel. When the sensor-actuator FRF is measured by the laser vibrometer, the accelerometer is removed from the panel in order to isolate the physical effect produced by the accelerometer itself.

Figure 3.14 shows that the solid line, which represents the simulated open loop sensor-actuator FRF of the actuator-plate fully coupled model, agrees well with the dotted line for the measured FRF using a laser vibrometer. This result confirms the accuracy of the proposed model for the mass and stiffness loading effects of the piezoelectric patch on the panel. Of particular importance is the offset feature, which enables the modeling of the effect produced by the bonding layer. Compared to the predicted one, the measured FRF is characterized by a larger number resonances. These are probably acoustic resonances of the cavity under the panel.

Figure 3.15 shows that the simulated (solid line) open loop sensor-actuator FRF of the actuator-plate-accelerometer fully coupled model is also in quite good agreement with the co-respective measured FRF (dotted line). Above about 8kHz, the amplitude of the measured FRF is slightly larger than that of the simulated one. Also, above about 6kHz the measured FRF is characterized by a larger phase lag than that of the simulated one. Finally, above the actuator resonance frequency, the measured FRF shows a sudden drop of the amplitude, which leads to an anti-resonance.

These differences between simulated and measured FRFs can be ascribed to two problems: first, the exact estimate of the case/seismic masses and transducer stiffness of the accelerometer, second the detailed modeling of the accelerometer and its mounting on the panel. It is likely that the anti-resonance at about 52kHz is the result of a much complicated dynamic response of the accelerometer than that simulated with a mass-spring-mass model. Also, the accelerometer has a certain contact area with the panel, which is not taken into account by the single lumped mass model. In this way the inertia effect of the accelerometer is over estimated, so that the amplitude of the simulated FRF decreases and phase lag effects of the simulated FRF are more pronounced than the measured ones.

This chapter has represented advanced mathematical models of a rectangular panel with a feedback control system, which consists of a small square piezoelectric patch actuator with an accelerometer sensor at its center. First, full details regarding the coupled models have been introduced, which consider loading and elastic effects of the actuator, and mounting effect, and the transfer function of the sensor. The piezoelectric patch actuator loading effect has been modeled by a grid of small lumped masses, and the stiffness effect has been modeled by arrays of lumped springs oriented in directions parallel to the lateral edges. The mounting offset effect is modeled as the increase of the moment arm length of the piezoelectric elastic effects.

The accelerometer has been modeled by a case and seismic lumped masses connected via a transducer lumped spring and dash-pot in parallel. The analyzes of the response obtained with these models have highlighted each physical effect of the actuator and sensor:

1. Inertia effect of actuator and sensor: Generate a constant amplitude roll off and phase lag effects in the higher frequency range
2. Stiffness: Locally increases the stiffness of the smart panel, and thus lowers the amplitude of the FRF in low frequencies
3. Offset: Globally rises the amplitude of the FRF at all frequencies, but more efficiently in higher frequencies.
4. Dynamic response of the accelerometer: Introduce an extra peak at relatively high frequency

Two fully coupled models has been derived, which consider the response of the plate and the piezoelectric actuator, and the response of the plate and both piezoelectric patch actuator and accelerometer sensor. The predicted responses of these two fully coupled model have been compared with two measurements taken on a panel with the piezoelectric patch actuator using either a laser vibrometer or an accelerometer sensor. The two measured responses confirm quite well the validity of the actuator and sensor models. The actuator-plate-accelerometer fully coupled model does not exactly match the corresponding measurements at relatively higher frequencies around the fundamental resonance of the accelerometer. This has been associated to the lack of details in the model of the accelerometer and transverse vibration of the piezoelectric patch.

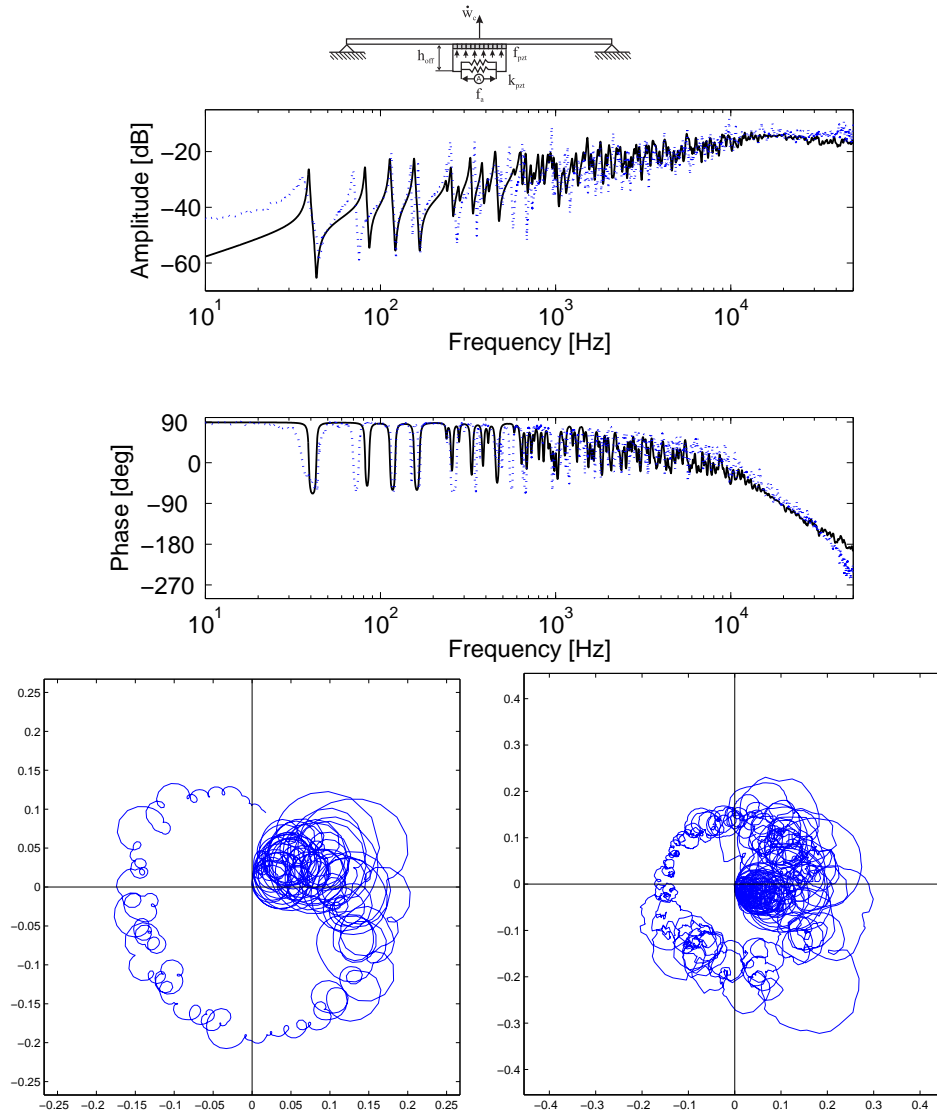


Figure 3.14: The Bode plot (top) and the Nyquist plot (bottom, 1 by 2 array) of simulated open loop FRF using the plate-actuator fully coupled model (solid line, left), and measured open loop FRF between the input signal to the piezoelectric actuator and the output signal obtained by laser vibrometer (dotted line, right)

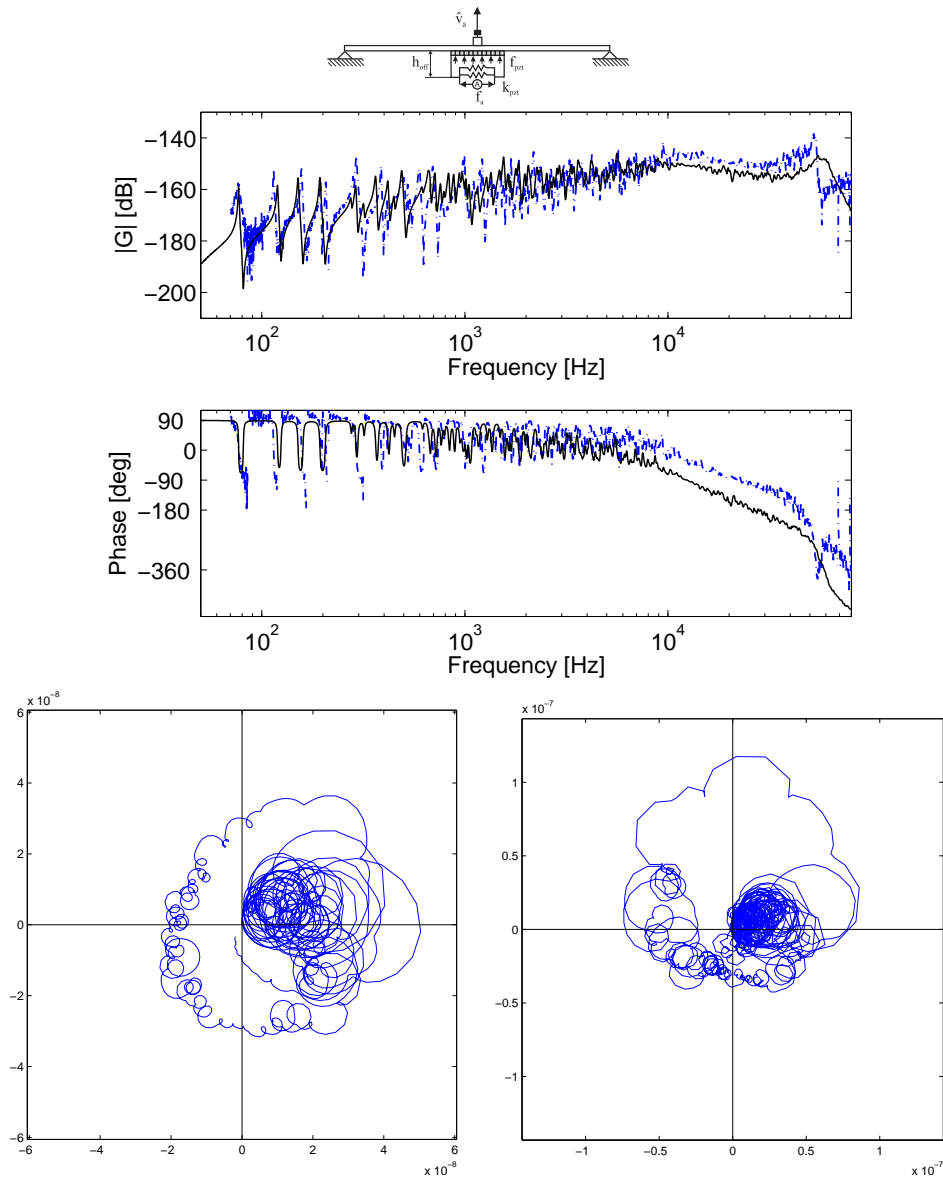


Figure 3.15: The Bode plot (top) and the Nyquist plot (bottom, 1 by 2 array) of the simulated open loop FRF using the plate-actuator-sensor fully coupled model (solid line, left), and the measured open loop FRF between the input signal to the piezoelectric actuator and the digitally integrated output signal obtained by the accelerometer sebsor (dotted line, right)

Chapter 4

PARAMETRIC STUDY OF PIEZOELECTRIC PATCH ACTUATOR

In the previous chapter, two fully coupled mathematical models are introduced and experimentally validated. Using these two models, parametric studies are carried out in this section with reference to:

1. size;
2. thickness;
3. combined size-thickness;
4. offset length.

For the third parametric study, the size and the thickness are modified in such a way as that the volume, and hence the weight, of the actuator is kept constant. For the fourth parametric study, the bonding of the actuator patch, that is the thickness of the bonding layer, varies.

The aim of this parametric study is to provide general guidelines for the design of a feasible actuator with good stability properties allowing high feedback gains in order to obtain good control performance and thus high active damping effects. All parametric studies have been carried out with reference to the Bode plot of the open loop sensor-actuator FRF and the maximum reduction index R_k for the 1st, 4th, 8th, and 11th resonances which occur respectively at approximately 39Hz, 134Hz, 322Hz and 446Hz.

4.1 Size

Figure 4.1 shows the four open loop FRFs between the ideal velocity sensor and the input signal to the practical piezoelectric patch actuator, and Figure 4.2 shows the four open loop FRFs between the integrated signal from the piezoceramic tri-shear accelerometer sensor and the input signal to the practical piezoelectric patch actuator. The four lines in the bode plots correspond to four patch actuators with different size. The parameters of the actuator are shown in Table 4.1.

The Bode plot in Figure 4.2 shows that the accelerometer introduces the additional peak at high frequency due to the accelerometer's resonance as discussed in section 3.4. Except for the additional peak, the two Bode plots in Figures 4.1 and Figures 4.2 are quite similar.

The Bode plots in Figures 4.1 and Figure 4.2 highlight that, at low frequency up to about 450Hz, the bigger is the actuator the larger tends to be the amplitude of the FRF. At higher frequencies this effect becomes less important, so that above about 5kHz the amplitudes of the FRF obtained for the four sizes are quite close to each other. This effect is caused by two factors. The first factor is a mass effect; this effect rolls off the amplitude of the FRF at high frequency. The increase of size results in a increase of the weight, so that at high frequency the amplitude of the FRF using the bigger actuator is more efficiently rolled off. The second factor is the ratio between the bending wavelength and the size of the actuator; the smaller is the ratio between the flexural wavelength and the size of the piezoelectric patch, the greater is the flexural actuation effect. Thus the flexural actuation generated by a piezoelectric patch rises monotonically with frequency and with the size of the patch. This trend is valid up to the frequencies, where the flexural wavelength is equal to the size of the patch[16]. According to Figure 4.3, with 20x20mm, 30x30mm, 40x40mm, and 50x50mm square piezoelectric patch actuators, this cut-off frequency is given as approximately 20kHz, 9kHz, 5kHz, and 3kHz, respectively. Therefore, the amplitude of the FRF using smaller actuator keeps increasing up to higher frequencies. As a result, at high frequencies the amplitudes of the FRF for various size of the actuators become similar. Thus at higher frequencies the actuation strength levels to a maximum value.

The Bode plots also show that, the bigger is the actuator the lower is the frequency, where the constant phase lag of the open loop sensor-actuator FRF starts. As discussed in section 2.3, this phase lag is due to the non-perfect collocation between the actuation around the perimeter of the piezoelectric patch and the sensing at the centre of the patch. Thus the phase lag occurs between the moment actuation at the four edges of the piezoelectric patch and the velocity detection at the centre of the piezoelectric patch.

In summary increasing the size of the actuator brings a beneficial effect in terms of control performance, since the low frequency the amplitude of the open loop sensor-actuator FRF is bigger, and therefore the direct velocity feedback loop produces higher damping effects. However, it also reduces the cut off frequency where the open loop sensor-actuator FRF is not anymore minimum phase and thus may bring to instabilities. The combination of these two effects can be assessed by looking to Figure 4.4 with the maximum reduction index R_k for the 1st, 4th, 8th, and 11th resonances. The right hand side plot shows the result with plate-actuator fully coupled model, and left hand side plot shows the result with plate-actuator-accelerometer fully coupled model.

Both plots in Figure 4.4 show that the maximum vibration reduction is globally increasing with small oscillation, as the size of the actuator rises. This oscillation is caused by the fact that the value δ_0 , where the FRF crosses the real negative axis, does not monotonically increase. Even if the part of locus of the FRF in negative quadrants becomes smaller, the crossing value over the real negative axis is strongly dependent on whether it occurs at either resonance or anti-resonance. Nevertheless, this plot clearly indicates the maximum vibration reduction at the control point for 1st, 4th, 8th, and 11th resonances increases as size grows. Therefore, it can be concluded that the bigger is the size, the bigger is the maximum vibration reduction at the control point at least up to 11th resonances.

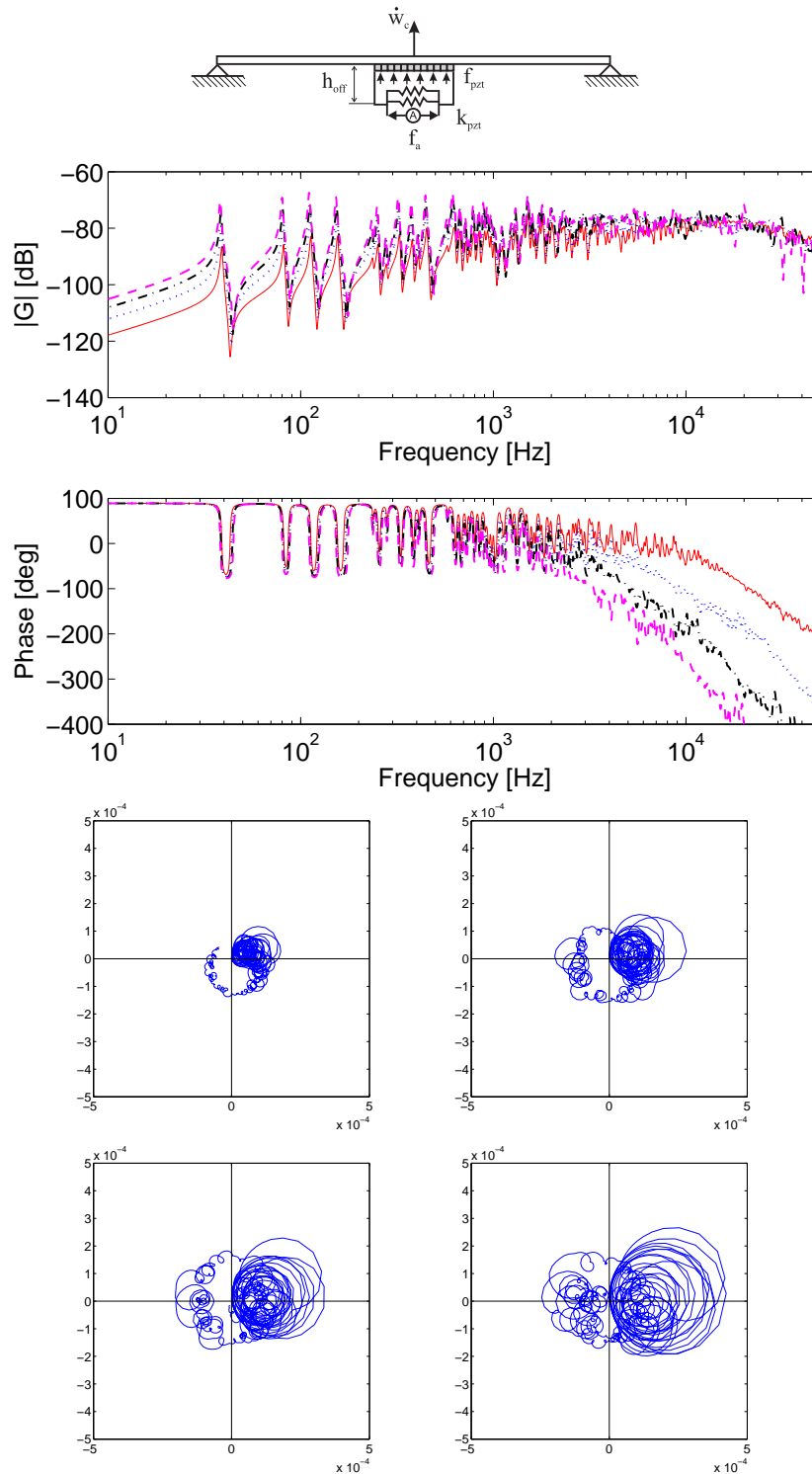


Figure 4.1: The Bode plot (top) and the Nyquist plot (bottom 2 x 2 array) of the open loop FRF between the ideal velocity sensor and various size actuators; Case 1: 20x20mm (faint line, left top), Case 2: 30x30mm (dotted line, right top), Case 3: 40x40mm (dash-dotted line, left down), Case 4: 50x50mm (dashed line, right down)

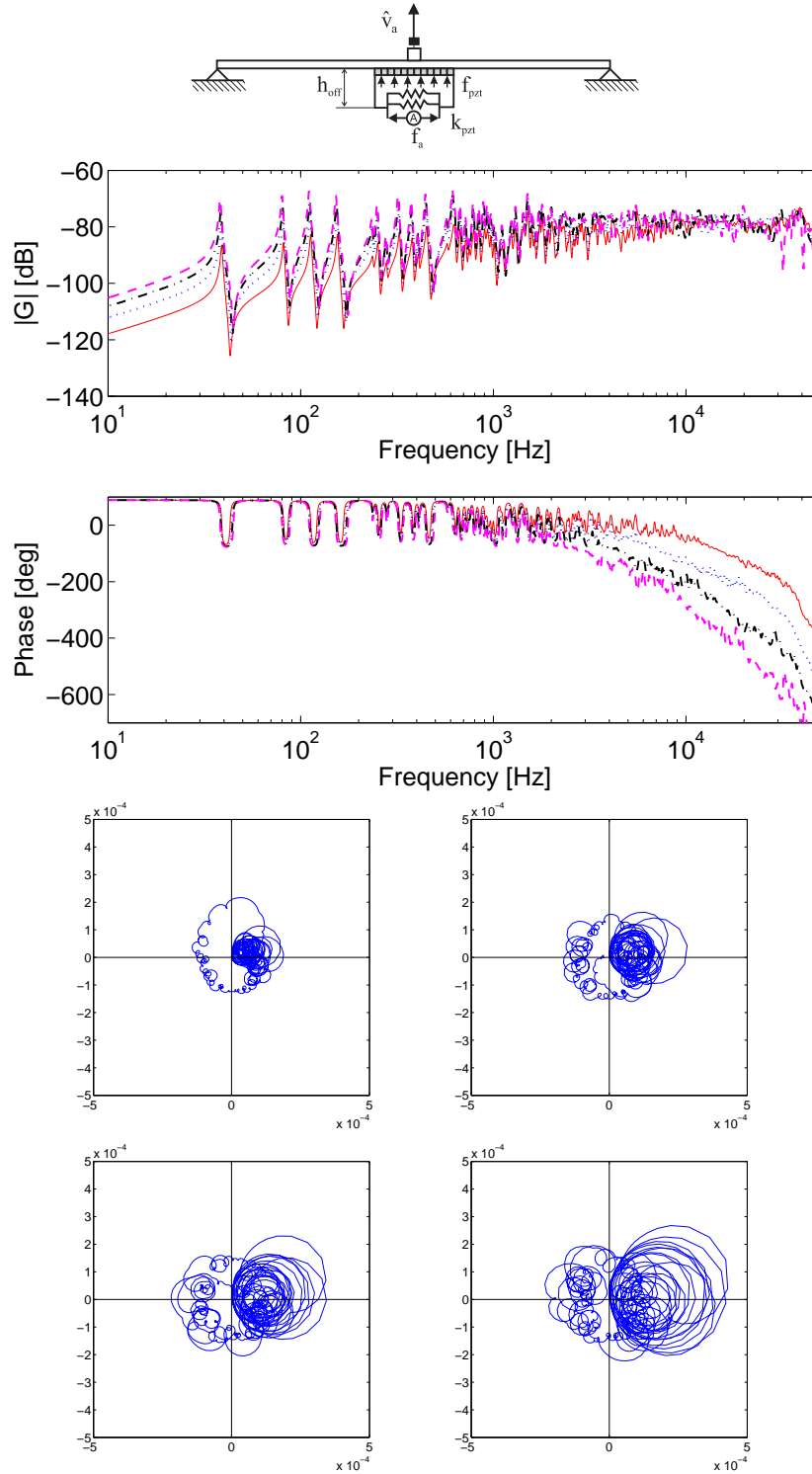


Figure 4.2: The Bode plot (top) and the Nyquist plot (bottom 2 x 2 array) of the open loop FRF between the integrated signal of the accelerometer sensor and various size actuators; Case 1: 20x20mm (faint line, left top), Case 2: 30x30mm (dotted line, right top), Case 3: 40x40mm (dash-dotted line, left down), Case 4: 50x50mm (dashed line, right down)

Table 4.1: Geometric parameter of the piezoelectric patch actuator considered in the parametric study regarding the actuator size

simulation	Size	thickness	weight
case1	20x20mm	0.5mm	1.530g
case2	30x30mm	0.5mm	3.443g
case3	40x40mm	0.5mm	6.120g
case4	50x50mm	0.5mm	9.563g

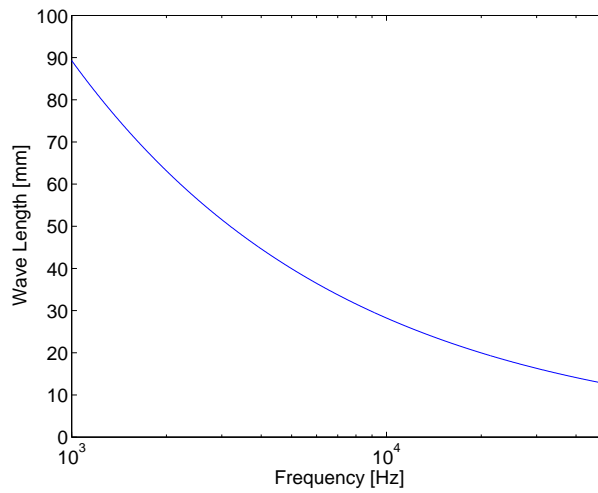


Figure 4.3: Flexural wavelength with reference to frequency

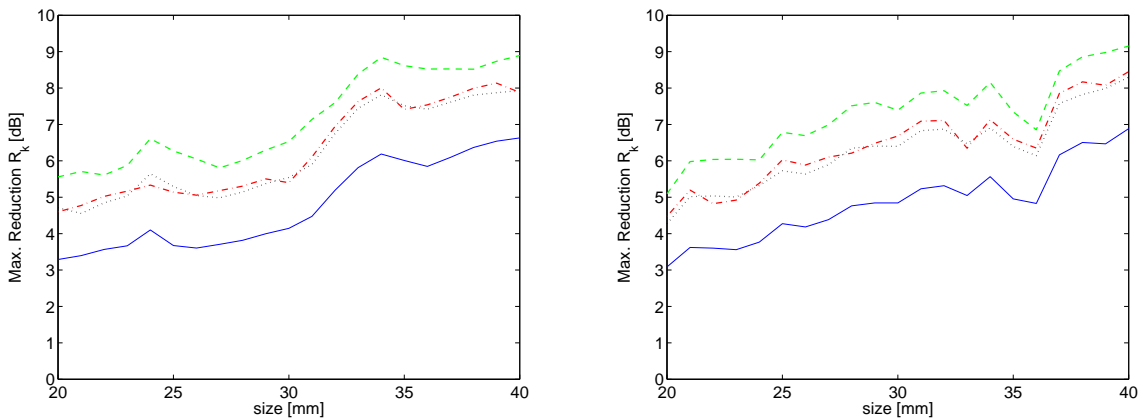


Figure 4.4: Maximum vibration reduction at 1st(blue solid line), 4th (black dotted line), 8th (red dot dashed line), and 11th resonance (green dashed line) with reference to the size length, using the ideal velocity sensor-actuator pair (left) or accelerometer sensor-actuator pair (right)

4.2 Thickness

Figures 4.5 shows the four open loop FRFs between the ideal velocity sensor and the input signal to the practical piezoelectric patch actuator, and Figures 4.6 shows the four open loop FRFs between the integrated signal from the piezoceramic tri-shear accelerometer sensor and the input signal to the practical piezoelectric patch actuator. The four lines in the bode plots correspond to four patch actuators with different thickness. The parameters of the actuator are shown in Table 4.2.

The Bode plots in Figures 4.5 and 4.6 indicate that, at low frequencies the thicker is the actuator the larger is the amplitude of the sensor-actuator open loop FRF. In contrast, at higher frequencies, the amplitude of the FRF goes down as thickness increases. These results are due to the fact that the increase of thickness results in two effects: a) increase of weight and b) increase of the moment arm. Increase of weight results in more attenuation of the amplitude of the FRF at high frequencies. Increasing moment arm subsequently causes a) increase of the stiffness effect of the patch actuator b) increase of actuation induced moment. The first effect attenuates the amplitude of the FRF at low frequencies, and the second one makes the overall amplitude of the FRF go up. The increase effect produced by the actuation induced moment is slightly bigger than the attenuation effect produced by the stiffness of the piezoelectric patch, so that the overall effect results in a small increment of the amplitude at low resonance frequency. In contrast the mass effect produces a clear reduction of the amplitude of the FRF at higher frequencies.

In summary thicker patches result in better control performance, since at low frequency the amplitude of the open loop sensor-actuator FRF is bigger, and therefore the direct velocity feedback loop produces higher damping effects. However it also reduces the cut off frequency where the open loop sensor-actuator FRF is not anymore minimum phase and thus may bring to instabilities. The combination of the stiffness, mass and moment actuation effects can be assessed by looking at the maximum reduction index R_k for the 1st, 4th, 8th, and 11th resonances shown in Figure 4.7. The left hand plot is obtained by using the plate-actuator-ideal sensor fully coupled model, and the right hand side plot is obtained by using plate-actuator-accelerometer sensor fully coupled model. Both plots clearly indicate that, the thicker is the actuator, the higher is the maximum vibration reduction at the control point that can be obtained with a stable system. However, this increasing trend is relatively smaller than that obtained by increasing the size of the actuator. For instance, even if the thickness is doubled, the maximum vibration reduction for the first resonance R_1 is approximately 0.5 dB bigger than that of the reference setting. In contrast doubling the size produces an increase of about 4 dB of the maximum vibration reduction. It is important to note that the greater is the thickness of the piezoelectric patch actuator the greater is the maximum driving voltage that can be applied to it. This feature has not been taken into account in this study. However it could be of great importance when large control gains are implemented.

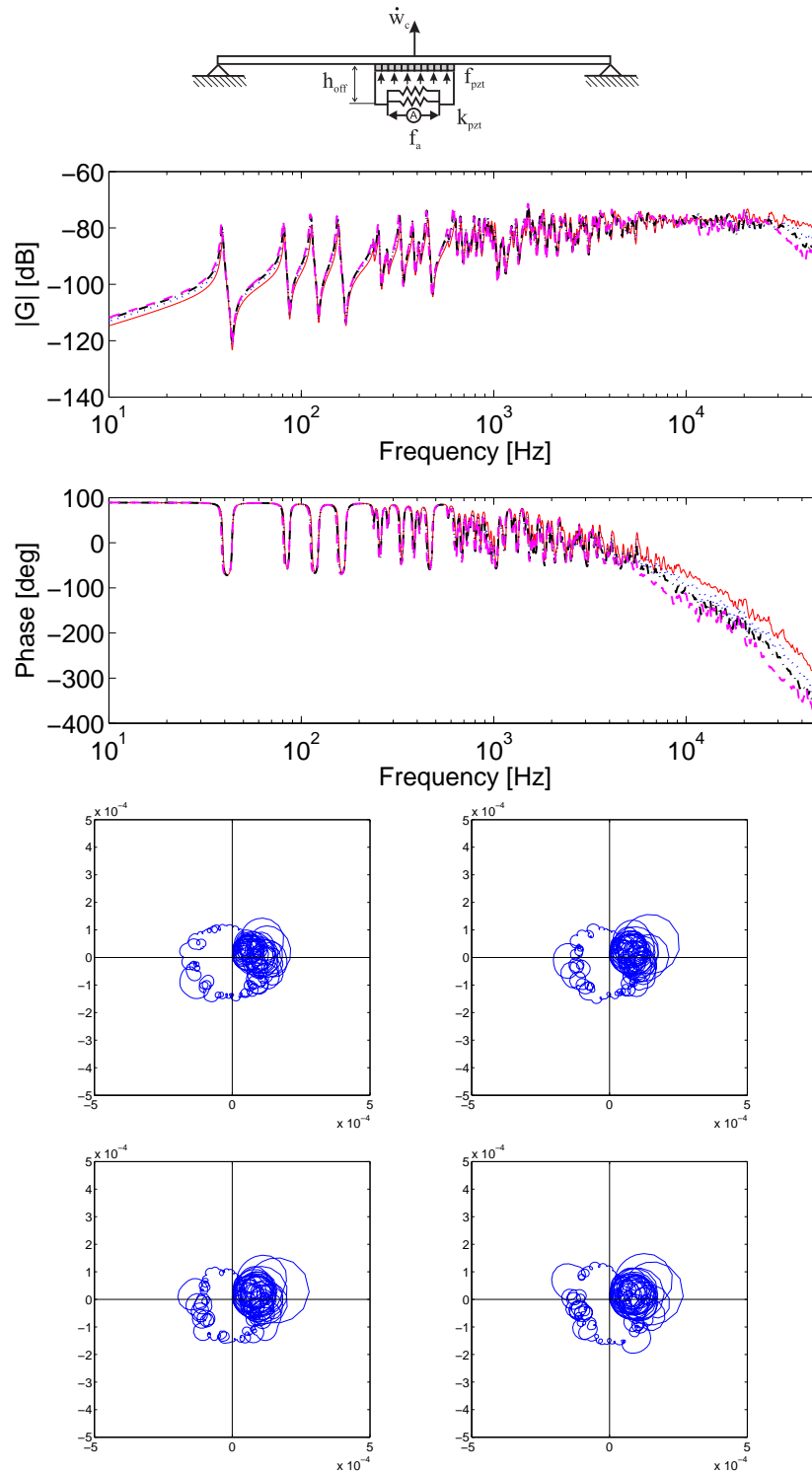


Figure 4.5: The Bode plot (top) and the Nyquist plot (bottom 2 x 2 array) of the open loop FRF between the ideal velocity sensor and various thickness actuators; Case 1: 0.001mm (faint line, left top), Case 2: 0.25mm (dotted line, right top), Case 3: 0.5mm (dash-dotted line, left down), Case 4: 1.0mm (dashed line, right down)

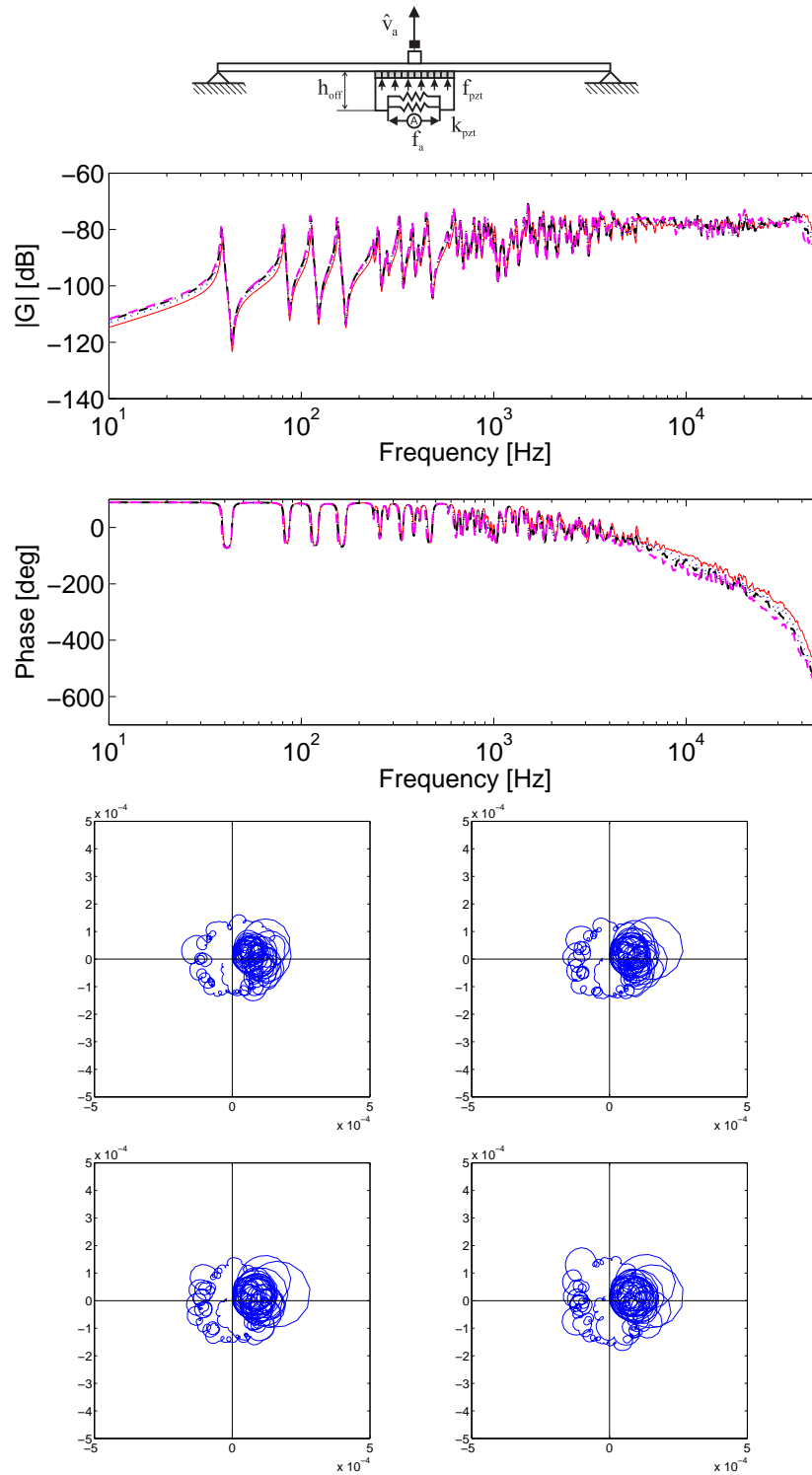


Figure 4.6: The Bode plot (top) and the Nyquist plot (bottom 2 x 2 array) of the open loop FRF between the integrated signal of the accelerometer sensor and various thickness actuators; Case 1: 0.001mm (faint line, left top), Case 2: 0.25mm (dotted line, right top), Case 3: 0.5mm (dash-dotted line, left down), Case 4: 1.0mm (dashed line, right down)

Table 4.2: Geometric parameter of the piezoelectric patch actuator considered in the parametric study regarding the actuator thickness

simulation	Size	thickness	weight
case1	30x30mm	0.0001mm	0.000g
case2	30x30mm	0.25mm	1.721g
case3	30x30mm	0.50mm	3.443g
case4	30x30mm	1.00mm	6.885g

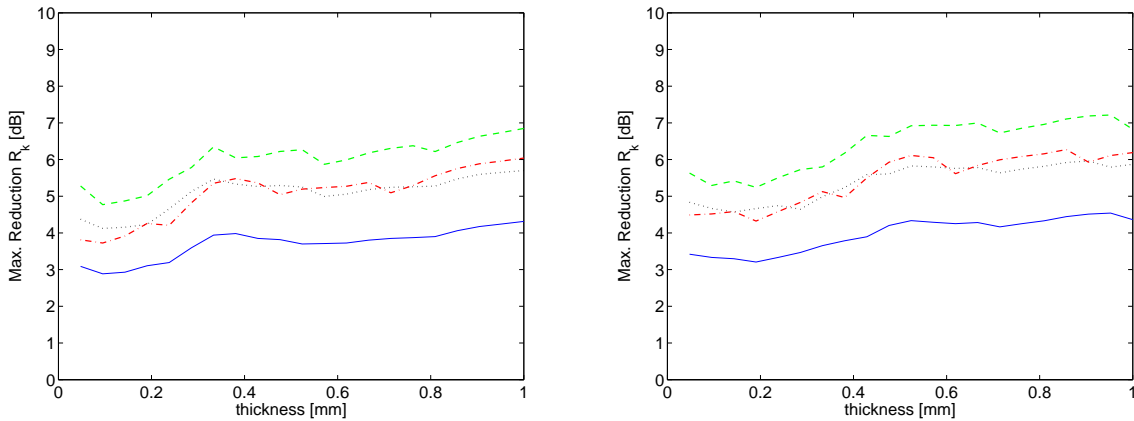


Figure 4.7: Maximum vibration reduction at 1st(blue solid line), 4th (black dotted line), 8th (red dot dashed line) ,and 11th resonances (green dashed line) with reference to the thickness of the actuator using the ideal velocity sensor-actuator pair (left) or using accelerometer sensor-actuator pair (right)

4.3 Combined Size and Thickness with Constant Volume

Figure 4.8 shows the four open loop FRFs between the ideal velocity sensor and the input signal to the practical piezoelectric patch actuator, and Figure 4.9 shows the four open loop FRFs between the integrated signal from the piezoceramic tri-shear accelerometer sensor and the input signal to the practical piezoelectric patch actuator. The four lines in the bode plots correspond to four patch actuators with different size and thickness, while the volume is kept constant. The parameters of the actuator are shown in Table 4.3.

The Bode plots in Figure 4.8 and Figure 4.9 indicate that, at low frequency up to about the 11th resonance, the thinner but bigger is the actuator, the larger tends to be the amplitude of the open loop sensor-actuator FRF. At higher frequencies, this trend becomes small so that the amplitudes of the FRF obtained for the four sizes are quite close to each other. However, as the actuator gets bigger and thinner, the cut off frequency where the phase lag exceeds -90deg is brought down and thus greater phase lags are generated at higher frequencies. This result is quite similar to that of the parametric study with reference to the size shown in Figures 4.1 and 4.2. This fact indicates that the improvement of the maximum vibration reduction at the control position achieved by enlarging the size, is greater than the degradation of the control performance caused by the decrease of the thickness.

In summary, assuming constant volume, thinner but bigger actuator brings a beneficial effect in terms of control performance, since at low frequency the amplitude of the open loop sensor-actuator FRF is bigger, and therefore the direct velocity feedback loop produces higher damping effects. However, it also reduces the cut off frequency, where the open loop sensor-actuator FRF is not anymore minimum phase and thus may bring to instabilities. The combination of these two effects can be assessed by looking two plots in Figure 4.10 with the maximum reduction index R_k for the 1st, 4th, 8th, and 11th resonances using either ideal velocity sensor (left) or piezoceramic accelerometer sensor (right). The two plots clearly indicate that, the thinner but bigger actuator is, the bigger is the maximum vibration reduction at the control point that can be obtained with a stable system. Comparing this plot with that in Figures 4.4 and 4.7, it is preferable to select a thin piezoelectric patch and increase the size as much as practical construction constraints allow. However, it should be noted that as the thickness of the piezoelectric patch decreases, the maximum input voltage goes down.

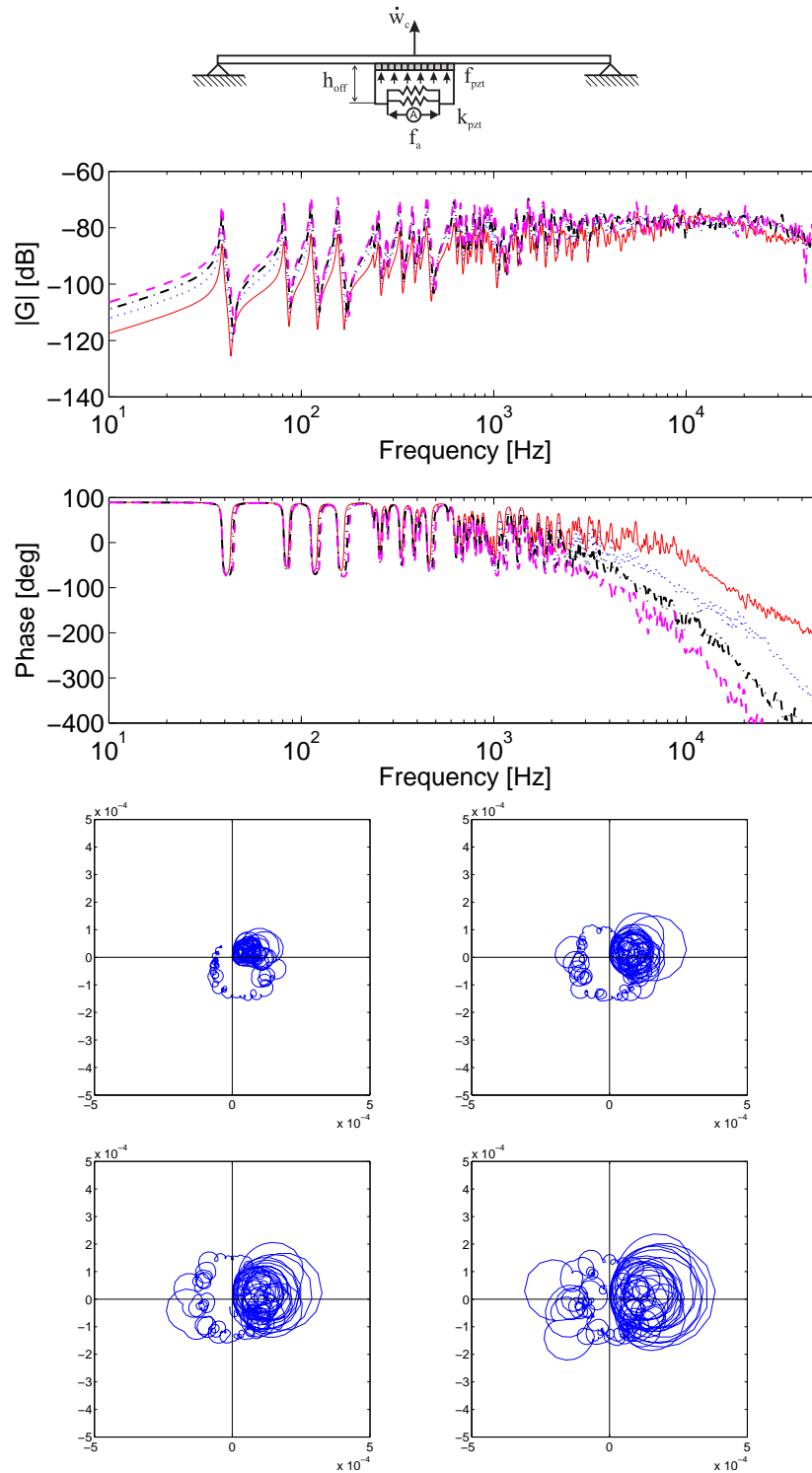


Figure 4.8: The Bode plot (top) and the Nyquist plot (bottom 2 x 2 array) of the open loop FRF between the ideal velocity sensor and various size and thickness actuators; Case 1: 20x20mm 1.125mm (faint line, left top), Case 2: 30x30mm 0.5mm (dotted line, right top), Case 3: 40x40mm 0.28mm (dash-dotted line, left down), Case 4: 50x50mm 0.18mm (dashed line, right down)

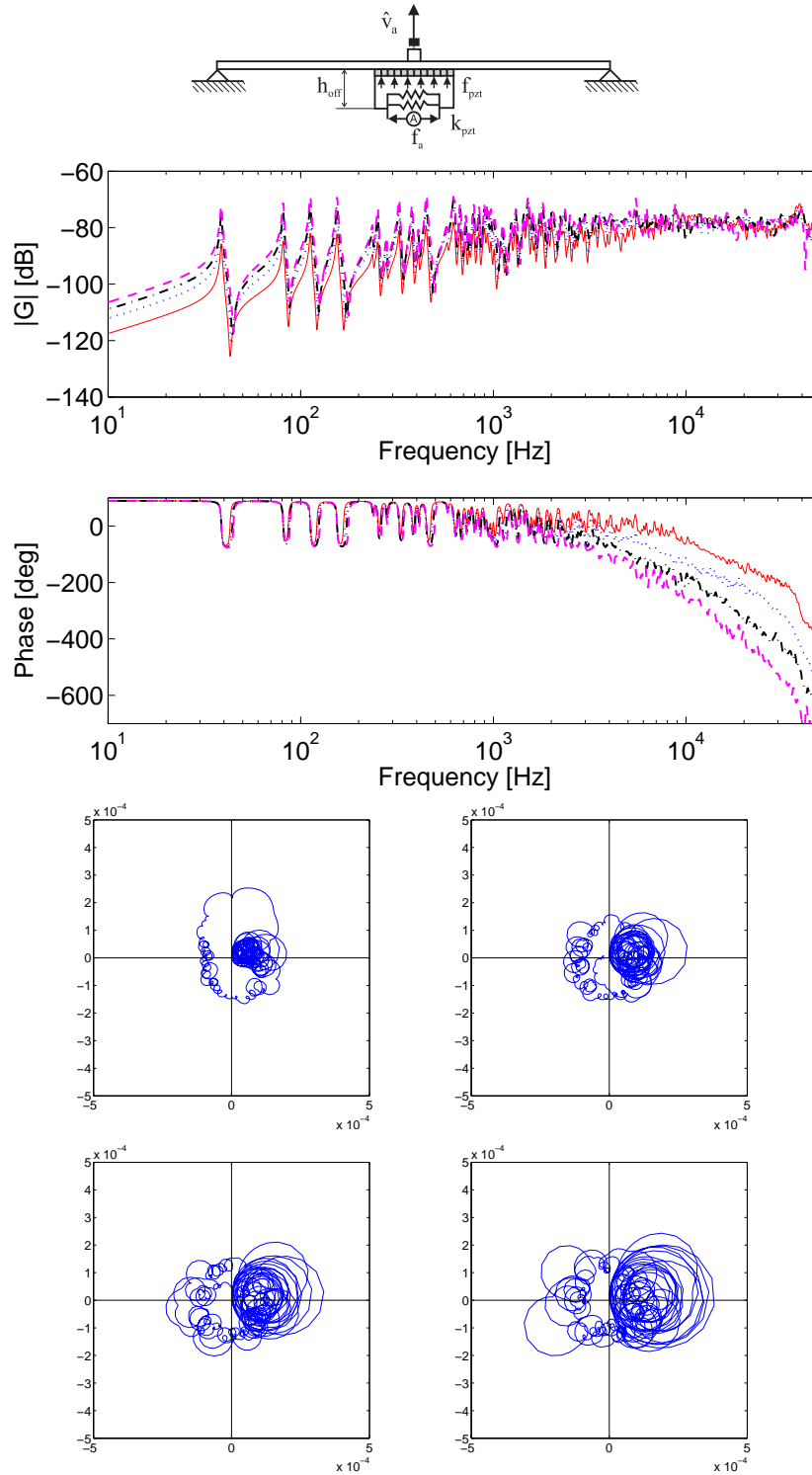


Figure 4.9: The Bode plot (top) and the Nyquist plot (bottom 2 x 2 array) of the open loop FRF between the integrated signal of the accelerometer sensor and various size and thickness actuators; Case 1: 20x20mm 1.125mm (faint line, left top), Case 2: 30x30mm 0.5mm (dotted line, right top), Case 3: 40x40mm 0.28mm (dash-dotted line, left down), Case 4: 50x50mm 0.18mm (dashed line, right down)

Table 4.3: Parameter of the actuator considered in the parametric study regarding the actuator size and thickness

simulation	Size	thickness	weight
case1	20x20mm	1.125mm	3.443g
case2	30x30mm	0.500mm	3.443g
case3	40x40mm	0.2813mm	3.443g
case4	50x50mm	0.1800mm	3.443g

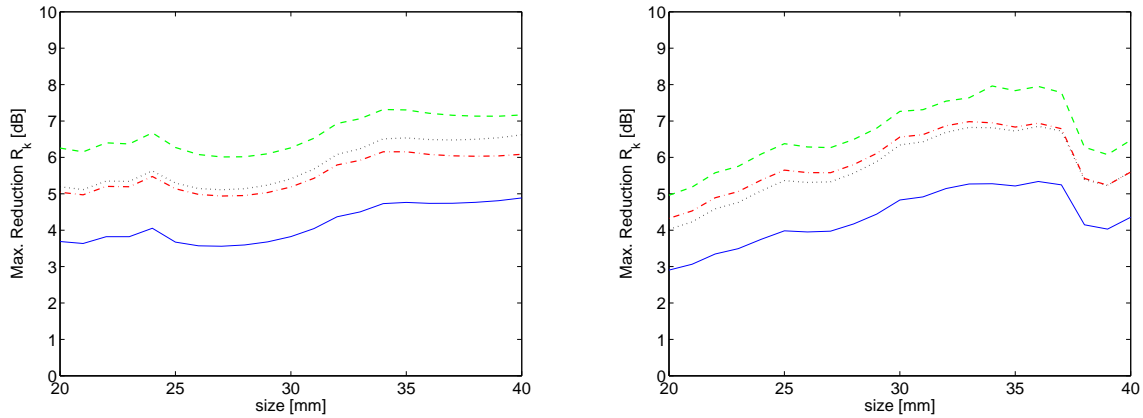


Figure 4.10: Maximum vibration reduction at 1st(blue solid line), 4th (black dotted line), 8th (red dot dashed line), and 11th resonance (green dashed line) with reference to the size of the actuator using the ideal velocity sensor-actuator pair (left) or using accelerometer sensor-actuator pair (right)

4.4 Offset Length

In the previous cases, the piezoelectric patch actuator was always directly attached on the surface of the panel. Figure 4.11 shows the four open loop FRFs between the ideal velocity sensor and the input signal to the practical piezoelectric patch actuator that is bonded on the plate via a bonding layer, which generates offset between the surface of the plate and of the piezoelectric patch. Figure 4.12 shows the four open loop FRFs between the integrated signal from the piezoceramic tri-shear accelerometer sensor and the input signal to the practical piezoelectric patch actuator that is bonded on the plate via a bonding layer. The four lines in the bode plots correspond to four different offset, raised from 0mm, i.e. ideal bonding, to +1mm. The thickness of the bonding layer is called bonding offset in this section. The parameters of the actuator are shown in Table 4.4.

The Bode plots in Figure 4.11 and Figure 4.12 indicate that as the bonding offset increases, the amplitude of the sensor-actuator open loop FRF tends to rise at all frequencies although it is much bigger at higher frequencies. This result is due to the fact that the increase of the bonding offset results in increase of the moment actuation effects of the piezoelectric patch and of the passive stiffness effect. The increase of moment actuation tends to increase the amplitude of the FRF in the entire frequency range. In contrast, the increase of stiffness tends to reduce the amplitude of the FRF particularly at low frequency. The first effect is much greater than the second one so that there is a mean increase of amplitude of the FRF as the offset raises. However, there is also a relative increase of the amplitudes at high frequencies. This effect reduces the maximum control gain that guarantees stability, because the phase lag remains almost the same as the offset increases. The overall result indicates that, it is preferable to bond the piezoelectric path on the panel using thinner glue.

In summary bonding the actuator on the panel via a thick bonding layer results in a decrease of the stability, since the open loop FRF is bigger at high frequencies, where the open loop FRF is located in the left half of the Nyquist plot. As a result, smaller control gains can be implemented and thus the direct velocity feedback loop produces lower damping effects. However, it also improve the amplitude of the FRF in the low frequency so that higher control effects are obtained for a given control gain. The combination of these two effects can be assessed by looking the two plots in Figure 4.13 with the maximum reduction index R_k for the 1st, 4th, 8th, and 11th resonances. The right hand side plot shows the simulation results using the ideal velocity sensor with the patch actuator, and left plot shows the result using the accelerometer sensor instead. Both plots clearly indicate that the thickness of the bonding layer reduces the maximum reduction vibration at the control point that can be obtained with a stable system.

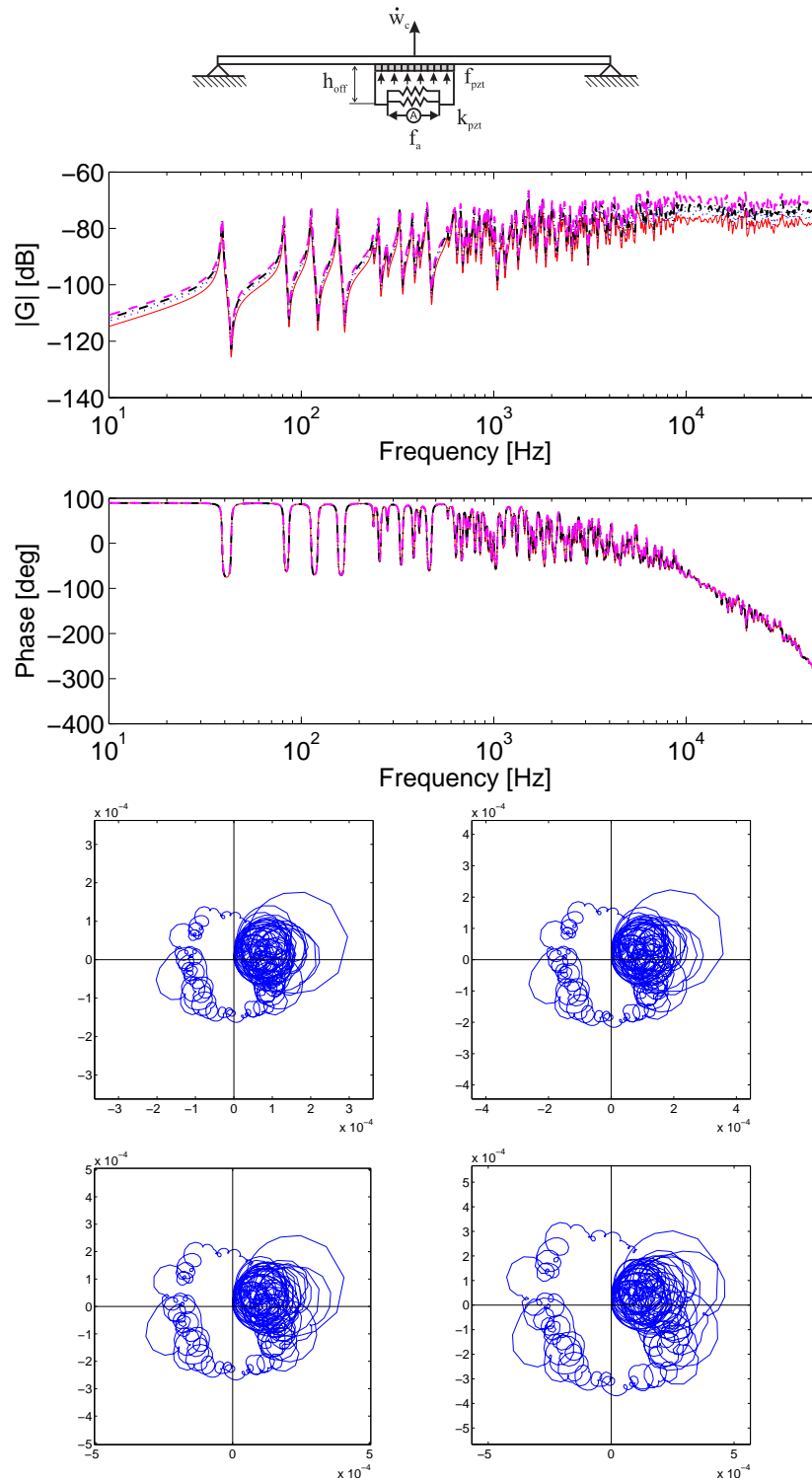


Figure 4.11: The Bode plot (top) and the Nyquist plot (bottom 2 x 2 array) of the open loop FRF between the ideal velocity sensor and the actuator with various offset length; Case 1: no offset (faint line, left top), Case 2: 0.25mm offset(dotted line, right top), Case 3: 0.5mm offset (dash-dotted line, left down), Case 4: 1.0mm offset(dashed line, right down)

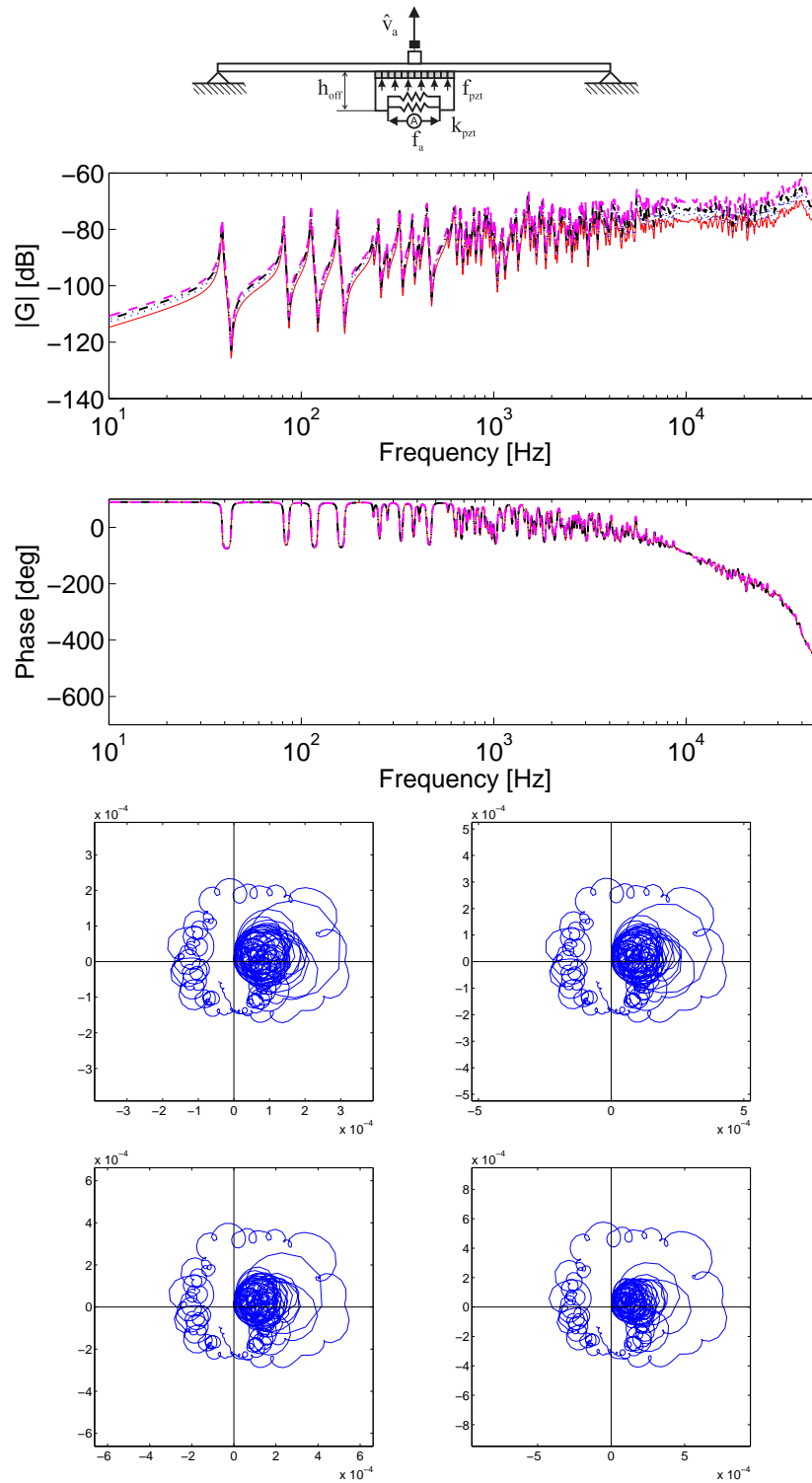


Figure 4.12: The Bode plot (top) and the Nyquist plot (bottom 2 x 2 array) of the open loop FRF between the ideal velocity sensor and the actuator with various offset length; Case 1: no offset (faint line, left top), Case 2: 0.25mm offset(dotted line, right top), Case 3: 0.5mm offset (dash-dotted line, left down), Case 4: 1.0mm offset(dashed line, right down)

Table 4.4: Geometric parameter of the piezoelectric patch actuator considered in the parametric study regarding the offset length

simulation	Size	thickness	weight	offset length
case1	25x25mm	0.500mm	3.443g	0mm
case2	25x25mm	0.500mm	3.443g	0.25mm
case3	25x25mm	0.500mm	3.443g	0.50mm
case4	25x25mm	0.500mm	3.443g	1.0mm

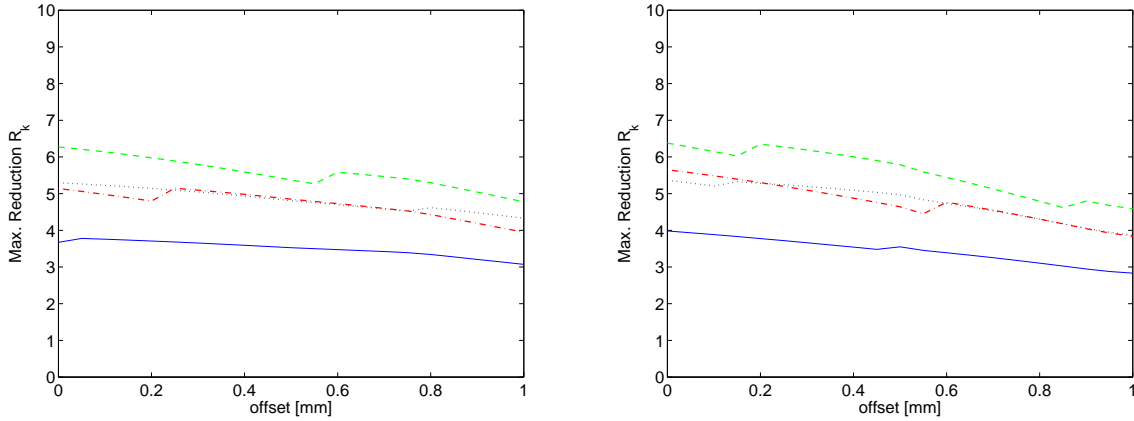


Figure 4.13: Maximum vibration reduction at 1st(blue solid line), 4th (black dotted line), 8th (red dot dashed line), and 11th resonance (green dashed line) with reference to the offset length, using the ideal velocity sensor-actuator pair (left) or using accelerometer sensor-actuator pair (right)

Chapter 5

CONCLUSION

This report describes the simulation study of a smart panel with closely located accelerometer sensor and square piezoelectric actuator feedback control system. The study presents the effect of the piezoelectric patch actuator on the control effectiveness and stability issues of the velocity feedback control loop. The stability and control performance analysis has been carried out with reference to the Bode and the Nyquist plots of the open loop sensor-actuator FRF. In particular a simple formula has been derived which gives the maximum vibration reduction at the error sensor position for the low frequency resonances with reference to the ratio between real parts of the locus at the resonance frequency and at the cross over frequency to the real negative axis.

This report presents the fully coupled model between a rectangular panel and a feedback control system, which consists of a small square piezoelectric patch actuator with an accelerometer sensor at its centre. Chapter 3 describes the detailed description of two fully coupled models, which consider the fully coupled response of the plate and the piezoelectric actuator, and the fully coupled response of the plate and both piezoelectric patch actuator and accelerometer sensor. The first model, plate actuator fully coupled model, is used to simulate the mass and stiffness effects produced by the piezoelectric patch actuator, and the offset effect due to the bonding layer of glue. The piezoelectric patch actuator loading effect has been modeled by a grid of small lumped masses and arrays of lumped springs oriented in directions parallel to the lateral edges. For the second model, the accelerometer has been modeled by a case and seismic lumped masses connected via a transducer lumped spring and dash-pot in parallel. The analyses of the response obtained with the two models have highlighted that the dynamic response of the accelerometer introduces an extra peak at relatively high frequency. Furthermore, due to the inertia effect of the accelerometer, a constant amplitude roll off and phase lag effects are generated in the higher frequency range.

The predicted FRFs have been compared with two measurements taken on a panel with the piezoelectric patch actuator using either a laser vibrometer or an accelerometer sensor. The two measured responses confirm quite well the validity of the two mathematical models. The actuator-plate-accelerometer fully coupled model does not exactly match the corresponding measurements at relatively higher frequencies around the fundamental resonance of the accelerometer. This has been associated to the lack of details in the model of the accelerometer and transverse vibration of the piezoelectric patch.

Using these verified models, a parametric study has then been carried out in order to assess the stability and control performance effects produced by: a) the size, b) the thickness, and c) the combined size and thickness with constant mass. The principal effects produced by

these parameters can be classified into three categories: first, a low frequency stiffness effect that tends to reduce the amplitude of the open loop sensor-actuator FRF; second, a bending moment actuation effect that tends to increase the amplitude of the open loop sensor-actuator FRF and third, a high frequency mass effect that tends to reduce the amplitude and increases the phase lag effects of the open loop sensor-actuator FRF. The weight of these three effects varies in different ways for the four parameters considered in the study. As a result, it has been found that the increase of size produces the significant improvement on control performance. In contrast, the thickness of the piezoelectric patch seems to have comparatively little effects to the other parameters although the simulations indicate that thicker patches are preferable.

Appendix A

Classical thin plate theory

A.1 Equation of Motion

This chapter presents the theory of a thin plate. The equation of motion of a thin plate with an external force excitation is given as follows [1]:

$$D_s \left(\frac{\partial^4 w}{\partial x^4} + 2 \frac{\partial^4 w}{\partial x^2 \partial y^2} + \frac{\partial^4 w}{\partial y^4} \right) + \rho_s h_s \frac{\partial^2 w}{\partial t^2} = f_p \delta^p, \quad (\text{A.1})$$

where h_s represents the thickness of the plate, ρ_s denotes the density of the plate, and w is the displacement normal to the plane. f_p is the primary point excitation, performed on (x_p, y_p) . δ^p represents the Dirac delta function defined as:

$$\delta^p = \delta(x - x_p) \delta(y - y_p). \quad (\text{A.2})$$

D_s is the flexural rigidity of the plate, given below:

$$D_s = \frac{E_s}{1 - \nu_s^2} \int_{-\frac{h_s}{2}}^{\frac{h_s}{2}} z^2 dz = \frac{E_s h_s^3}{12(1 - \nu_s^2)}, \quad (\text{A.3})$$

where E_s is the elastic module, and ν_s is the Poisson ratio of the panel.

Assuming a time-harmonic vibration, the out-plate transverse displacement in (m,n)th natural mode w_{mn} can be written as:

$$w_{mn}(x, y, \omega, t) = \tilde{w}_{mn}(x, y, \omega) e^{i\omega t}, \quad (\text{A.4})$$

where ω represents the circular frequency, and the phasor \tilde{w} is given as follows:

$$\tilde{w}_{mn}(x, y, \omega) = \phi_{mn}(x, y) q_{mn}^p(\omega), \quad (\text{A.5})$$

where ϕ_{mn} represents the mode shape function of the (m,n)th natural mode of the plate, and q_{mn}^p is the corresponding modal amplitude excited by the primary excitation. The mode function of the plate can be written as the product of two beam functions which has the same boundary condition as the plate:

$$\phi_{mn} = \phi_m^x \phi_n^y. \quad (\text{A.6})$$

For a simply supported plate, the beam function is given in the following formula:

$$\phi_m^x = \sin\left(\frac{m\pi x}{l_x}\right) \quad (\text{A.7})$$

$$\phi_n^y = \sin\left(\frac{n\pi y}{l_y}\right), \quad (\text{A.8})$$

where l_x is the x-direction length of the plate, and l_y is the y-direction length. For a clamped plate, the beam function is given below:

$$\phi_m^x = \cosh\left(\frac{\lambda_m x}{l_x}\right) - \cos\left(\frac{\lambda_m x}{l_x}\right) - \sigma_m \left\{ \sinh\left(\frac{\lambda_m x}{l_x}\right) - \sin\left(\frac{\lambda_m x}{l_x}\right) \right\} \quad (\text{A.9})$$

$$\phi_n^y = \cosh\left(\frac{\lambda_n y}{l_y}\right) - \cos\left(\frac{\lambda_n y}{l_y}\right) - \sigma_n \left\{ \sinh\left(\frac{\lambda_n y}{l_y}\right) - \sin\left(\frac{\lambda_n y}{l_y}\right) \right\}. \quad (\text{A.10})$$

σ_m and σ_n can be defined as follows:

$$\sigma_k = \frac{\cosh \lambda_k - \cos \lambda_k}{\sinh \lambda_k - \sin \lambda_k}, \quad (\text{A.11})$$

where λ_k denotes the wavelength, and it can be obtained by numerically solving the following equation:

$$\tan \frac{\lambda_i}{2} + \tanh \frac{\lambda_i}{2} = 0, \quad i = \frac{k+1}{2} \quad (\text{A.12})$$

$$\tan \frac{\lambda_j}{2} - \tanh \frac{\lambda_j}{2} = 0, \quad j = \frac{k}{2}. \quad (\text{A.13})$$

After substituting Eq.(A.4) into Eq.(A.1), multiplying it with the (p, q) th mode shape function $\phi_{pq}(x, y)$ and taking the integral over the area, the following formula results:

$$\begin{aligned} D_s \int_0^{l_x} \int_0^{l_y} \phi_{pq} q_{mn}^p e^{i\omega t} \left(\frac{\partial^4 \phi_{mn}}{\partial x^4} + 2 \frac{\partial^4 \phi_{mn}}{\partial x^2 \partial y^2} + \frac{\partial^4 \phi_{mn}}{\partial y^4} \right) dx dy \\ + \int_0^{l_x} \int_0^{l_y} \phi_{pq} q_{mn}^p \rho_s h_s \phi_{mn} \frac{\partial^2 e^{i\omega t}}{\partial t^2} dx dy \\ = \int_0^{l_x} \int_0^{l_y} f_p(\omega, t) \delta^p \phi_{pq} dx dy. \end{aligned} \quad (\text{A.14})$$

When $(p, q) \neq (m, n)$, the above equation is equal to zero due to orthogonality. When $(p, q) = (m, n)$, the first term of the left hand-side formula is given as[1]:

$$D_s \int_0^{l_x} \int_0^{l_y} \phi_{mn} q_{mn}^p e^{i\omega t} \left(\frac{\partial^4 \phi_{mn}}{\partial x^4} + 2 \frac{\partial^4 \phi_{mn}}{\partial x^2 \partial y^2} + \frac{\partial^4 \phi_{mn}}{\partial y^4} \right) dx dy = \Lambda \omega_{mn}^2 q_{mn}^p e^{i\omega t}, \quad (\text{A.15})$$

where Λ is the modal mass calculated as follows:

$$\begin{aligned} \int_0^{l_x} \int_0^{l_y} \rho_s h_s \phi_{mn}^2 dx dy &= \frac{\rho_s h_s l_x l_y}{4} \\ &= \frac{m_s}{4} \\ &= \Lambda, \end{aligned} \quad (\text{A.16})$$

where m_s denotes the mass of the plate, and ω_{mn} is the $(m, n)^{th}$ mode natural frequency of the plate, expressed below:

$$\omega_{mn} = \sqrt{\frac{D_s}{\rho_s h_s}} \pi^2 F_{mn}. \quad (\text{A.17})$$

F_{mn} from the above equation is defined below:

$$F_{mn} = \sqrt{\frac{G_x^4(m)}{l_x^4} + \frac{G_y^4(n)}{l_y^4} + \frac{2H_x(m)H_y(n)}{l_x^2 l_y^2}}. \quad (\text{A.18})$$

The constants G_x , H_x and G_y , H_y for simple supported, clamped plates are given in Table A.1.

The second term of the left hand-side Eq.(A.14) can be written as:

$$\begin{aligned} \int_0^{l_x} \int_0^{l_y} \rho_s h_s q_{mn}^p \phi_{mn} \phi_{mn} \frac{\partial^2 e^{i\omega t}}{\partial t^2} dx dy &= -\omega^2 q_{mn}^p e^{i\omega t} \int_0^{l_x} \int_0^{l_y} \rho_s h_s \phi_{mn}^2 dx dy \\ &= -\omega^2 \Lambda q_{mn}^p e^{i\omega t}. \end{aligned} \quad (\text{A.19})$$

Due to the delta function $\delta(x, y)$, the right hand-side term of Eq.(A.14) can be expressed as:

$$\int_0^{l_x} \int_0^{l_y} f_p(\omega, t) \delta^p \phi_{mn}(x, y) dx dy = f_p(\omega, t) \phi_{mn}^p, \quad (\text{A.20})$$

where ϕ_{mn}^p defines as the shape function at (x_p, y_p) on the plate:

$$\phi_{mn}^p = \phi_{mn}(x_p, y_p). \quad (\text{A.21})$$

The primary excitation f_p can be expressed using the phasor $\tilde{f}_p(\omega)$ as follows:

$$f_p(\omega, t) = \tilde{f}_p(\omega) e^{i\omega t}. \quad (\text{A.22})$$

Substituting Eq.(A.15), Eq.(A.19) and Eq.(A.20) into Eq.(A.14), and dividing the equation by $e^{i\omega t}$ leads to the following formula:

$$\Lambda(\omega_{mn}^2 q_{mn}^p - \omega^2 q_{mn}^p) = \tilde{f}_p \phi_{mn}^p. \quad (\text{A.23})$$

Therefore, q_{mn}^p is given as:

$$q_{mn}^p = \frac{\tilde{f}_p \phi_{mn}^p}{\Lambda(\omega_{mn}^2 - \omega^2)}. \quad (\text{A.24})$$

Considering the structural loss factor η_s , the previous equation can be modified as:

$$q_{mn}^p = \frac{\tilde{f}_p \phi_{mn}^p}{\Lambda(\omega_{mn}^2 (1 + j\eta_s) - \omega^2)}. \quad (\text{A.25})$$

Due to linearity, the velocity of the panel is given as the summation of all resonant modes:

$$\tilde{w}(x, y, \omega) = \sum_{m=1}^{\infty} \sum_{n=1}^{\infty} \phi_{mn} q_{mn}^p. \quad (\text{A.26})$$

By substituting Eq.(A.25) into Eq.(A.26) the phasor of the velocity for a thin plate with external point force excitation can be calculated:

$$\tilde{w}(x, y, \omega) = \sum_{m=1}^{\infty} \sum_{n=1}^{\infty} \frac{\phi_{mn} \phi_{mn}^p}{\Lambda(\omega_{mn}^2(1 + j\eta_s) - \omega^2)} \tilde{f}_p. \quad (\text{A.27})$$

With harmonic excitation, the phasor of the transverse velocity $\dot{\tilde{w}}$ is given by multiplying the vertical displacement $j\omega$, i.e.:

$$\dot{\tilde{w}}(x, y, \omega) = j\omega \tilde{w}. \quad (\text{A.28})$$

Using the concept of mobility, the previous equation is modified as follows:

$$\dot{\tilde{w}} = Y_{sp} f_p, \quad (\text{A.29})$$

where the mobility Y_{sp} is defined as the ratio between the velocity of the plate and the primary excitation:

$$Y_{sp} = Y_{\dot{w}, f_p} = \frac{\dot{\tilde{w}}}{f_p} = j\omega \sum_{m=1}^{\infty} \sum_{n=1}^{\infty} \frac{\phi_{mn} \phi_{mn}^p}{\Lambda(\omega_{mn}^2(1 + j\eta_s) - \omega^2)}. \quad (\text{A.30})$$

Table A.1: Values for the constants G_x and H_x

Boundary conditions	m	G_x	H_x
Simply supported	1,2,3,...	m	m^2
Clamped	1	1.506	1.248
	2,3,4,...	$m + \frac{1}{2}$	$\left(m + \frac{1}{2}\right)^2 \left[1 - \frac{4}{(2m+1)\pi}\right]$

A.2 Force Actuator

When a second point force is added to the system as a secondary excitation, the law of superposition can be applied due to linearity. Therefore, the equation of motion can be modified as follows:

$$D_s \left(\frac{\partial^4 w}{\partial x^4} + 2 \frac{\partial^4 w}{\partial x^2 \partial y^2} + \frac{\partial^4 w}{\partial y^4} \right) + \rho_s h_s \frac{\partial^2 w}{\partial t^2} = f_p \delta^p + f_c \delta^c, \quad (\text{A.31})$$

where f_c is the secondary point force, and δ^c is the Dirac delta function defined below:

$$\delta^c = \delta(x - x_c) \delta(y - y_c), \quad (\text{A.32})$$

where (x_c, y_c) are the coordinates of the point, where the secondary point force is acting on the plate. The displacement of the plate can be given as the summation of the displacement excited by the primary excitation and the displacement excited by the control force. Therefore, Eq.(A.5) can be written as:

$$\tilde{w}_{mn}(x, y, \omega) = \phi_{mn}(x, y) q_{mn}^p(\omega) + \phi_{mn}(x, y) q_{mn}^c(\omega), \quad (\text{A.33})$$

where q_{mn}^p is already given in Eq.(A.25), and q_{mn}^c can be obtained by replacing ϕ_{mn}^p with ϕ_{mn}^c , and \tilde{f}_p with \tilde{f}_c in Eq.(A.25):

$$q_{mn}^c = \frac{\tilde{f}_c \phi_{mn}^c}{\Lambda(\omega_{mn}^2(1 + j\eta_s) - \omega^2)}. \quad (\text{A.34})$$

Therefore, the displacement at an arbitral point of the plate \tilde{w} is given as follows:

$$\tilde{w}(x, y, \omega) = \sum_{m=1}^{\infty} \sum_{n=1}^{\infty} \frac{\phi_{mn} \phi_{mn}^p}{\Lambda(\omega_{mn}^2(1 + j\eta_s) - \omega^2)} \tilde{f}_p + \sum_{m=1}^{\infty} \sum_{n=1}^{\infty} \frac{\phi_{mn} \phi_{mn}^c}{\Lambda(\omega_{mn}^2(1 + j\eta_s) - \omega^2)} \tilde{f}_c. \quad (\text{A.35})$$

Using the mobility term, the transverse velocity of the plate is simply given by:

$$\tilde{w} = Y_{sp} \tilde{f}_p + Y_{sc}^F \tilde{f}_c, \quad (\text{A.36})$$

where Y_{sc}^F is the mobility between the secondary point force and the out-plate velocity:

$$Y_{sc}^F = Y_{\dot{w}, f_c} = \frac{\dot{\tilde{w}}}{\tilde{f}_c} = j\omega \sum_{m=1}^{\infty} \sum_{n=1}^{\infty} \frac{\phi_{mn} \phi_{mn}^c}{\Lambda(\omega_{mn}^2(1 + j\eta_s) - \omega^2)}. \quad (\text{A.37})$$

The velocity at the secondary excitation point \tilde{w}_c is given by:

$$\dot{w}_c = Y_{cp} \tilde{f}_p + Y_{cc}^F \tilde{f}_c. \quad (\text{A.38})$$

The two mobility terms Y_{cp} and Y_{cc}^F are given below:

$$Y_{cp} = j\omega \sum_{m=1}^{\infty} \sum_{n=1}^{\infty} \frac{\phi_{mn}^c \phi_{mn}^p}{\Lambda(\omega_{mn}^2(1 + j\eta_s) - \omega^2)} \quad (\text{A.39})$$

$$Y_{cc}^F = j\omega \sum_{m=1}^{\infty} \sum_{n=1}^{\infty} \frac{\phi_{mn}^c \phi_{mn}^c}{\Lambda(\omega_{mn}^2(1 + j\eta_s) - \omega^2)}. \quad (\text{A.40})$$

A.3 Strain Actuator

It is assumed that the piezoelectric actuator induces internal moments in both x and y directions, which are only present under the piezoelectric patch extent. Therefore, the excitation of the piezoelectric patch actuator can be approximated by four line moments, all with equal magnitude acting along the edges of the patch. Thus, the equation of motion can be modified as:

$$D_s \left(\frac{\partial^4 w}{\partial x^4} + 2 \frac{\partial^4 w}{\partial x^2 \partial y^2} + \frac{\partial^4 w}{\partial y^4} \right) + \rho_s h_s \frac{\partial^2 w}{\partial t^2} = f_p \delta^p + m_{cx} (\delta'_{x1} - \delta'_{x2}) (H_{y1} - H_{y2}) + m_{cy} (H_{x1} - H_{x2}) (\delta'_{y1} - \delta'_{y2}), \quad (\text{A.41})$$

where m_{cx} and m_{cy} represent the actuator induced bending moment per unit length along the x - and y -axis, respectively. H is the unit Heaviside step function defined as:

$$H(x) = \begin{cases} 1, & x > 0 \\ 0, & x < 0 \end{cases} \quad (\text{A.42})$$

The terms of the Heaviside function in Eq.(A.31) are defined below:

$$\begin{aligned}
H_{x1} &= H(x - x_{c1}) \\
H_{x2} &= H(x - x_{c2}) \\
H_{y1} &= H(y - y_{c1}) \\
H_{y2} &= H(y - y_{c2}),
\end{aligned} \tag{A.43}$$

where (x_{c1}, y_{c1}) and (x_{c2}, y_{c2}) are the coordinates of the square, along which the line moment is exerted. δ' represents the first derivative of the Dirac delta function with reference to its argument:

$$\begin{aligned}
\delta'_{x1} &= \frac{\partial}{\partial x} \delta(x - x_{c1}) \\
\delta'_{x2} &= \frac{\partial}{\partial x} \delta(x - x_{c2}) \\
\delta'_{y1} &= \frac{\partial}{\partial y} \delta(y - y_{c1}) \\
\delta'_{y2} &= \frac{\partial}{\partial y} \delta(y - y_{c2}).
\end{aligned} \tag{A.44}$$

Using the mobility term, the transverse velocity of the plate is given below:

$$\tilde{w} = Y_{sp} \tilde{f}_p + Y_{sc}^P \tilde{m}_c, \tag{A.45}$$

where \tilde{m}_c is the phasor of the line moments given as:

$$m_c = \tilde{m}_c e^{j\omega t}. \tag{A.46}$$

Y_{sc}^P is the mobility between the secondary line moments and the out-plate velocity:

$$Y_{sc}^P = Y_{\dot{w}, m_c} = \frac{\tilde{w}}{m_c} = j\omega \sum_{m=1}^{\infty} \sum_{n=1}^{\infty} \frac{\phi_{mn} \psi_{mn}^c}{\Lambda(\omega_{mn}^2(1 + j\eta_s) - \omega^2)}. \tag{A.47}$$

ψ_{mn}^c is the (m,n)th bending natural mode, defined as follows:

$$\psi_{mn}^c = \int_{x_{c1}}^{x_{c2}} \psi_{mn}^y(x_c, y_{c1}) - \psi_{mn}^y(x_c, y_{c2}) dx_c + \int_{y_{c1}}^{y_{c2}} \psi_{mn}^x(x_{c1}, y_c) - \psi_{mn}^x(x_{c2}, y_c) dy_c, \tag{A.48}$$

where ψ_{mn}^x and ψ_{mn}^y are the first derivatives of $\phi_{mn}(x, y)$ with reference to x and y , respectively:

$$\psi_{mn}^x = \frac{\partial \phi_{mn}}{\partial x} = \frac{\partial \phi_m^x}{\partial x} \phi_n^y \tag{A.49}$$

$$\psi_{mn}^y = \frac{\partial \phi_{mn}}{\partial y} = \phi_m^x \frac{\partial \phi_n^y}{\partial y}. \tag{A.50}$$

When a simply supported plate is considered, the (m,n)th bending natural mode ψ_{mn}^c is given as follows:

$$\psi_{mn} = \left(\frac{n}{m} \frac{l_x}{l_y} + \frac{m}{n} \frac{l_y}{l_x} \right) \left(\cos \left(\frac{m\pi x_{c1}}{l_x} \right) - \cos \left(\frac{m\pi x_{c2}}{l_x} \right) \right) \left(\cos \left(\frac{n\pi y_{c1}}{l_y} \right) - \cos \left(\frac{n\pi y_{c2}}{l_y} \right) \right). \tag{A.51}$$

The velocity at the secondary excitation point \tilde{w}_c is given by:

$$\dot{w}_c = Y_{cp}f_p + Y_{cc}^P m_c. \quad (\text{A.52})$$

The mobility due to the line moments excitation is defined below:

$$Y_{cc}^P = j\omega \sum_{m=1}^{\infty} \sum_{n=1}^{\infty} \frac{\phi_{mn}^c \psi_{mn}^c}{\Lambda(\omega_{mn}^2(1 + j\eta_s) - \omega^2)}. \quad (\text{A.53})$$

Appendix B

Mobility

In this chapter, the formulas for the mobility functions discussed in Chapter 3 are given.

B.1 Ideal Sensor and Ideal Actuator

When the panel is excited by the primary excitation f_p and the control moment m_c that is generated by the ideal piezoelectric actuator, the phasor of the velocity in z-direction at the sensor position \dot{w}_c can be written using the following mobility expression:

$$\dot{w}_c = Y_{cp}f_p + \mathbf{Y}_{cc}^p \mathbf{m}_c, \quad (\text{B.1})$$

where Y_{cp} is given by:

$$Y_{cp} = j\omega \sum_{m=1}^{\infty} \sum_{n=1}^{\infty} \frac{\phi_{mn}^c \phi_{mn}^p}{\Lambda[\omega_{mn}^2(1+j\eta_s) - \omega^2]}. \quad (\text{B.2})$$

\mathbf{Y}_{cc}^p is a 4-element row vector:

$$\mathbf{Y}_{cc}^p = \begin{Bmatrix} Y_{cx1} \\ Y_{cx2} \\ Y_{cy1} \\ Y_{cy2} \end{Bmatrix}^T = \begin{Bmatrix} j\omega \sum_{m=1}^{\infty} \sum_{n=1}^{\infty} \frac{\phi_{mn}^c \psi_{x1}}{\Lambda[\omega_{mn}^2(1+j\eta_s) - \omega^2]} \\ j\omega \sum_{m=1}^{\infty} \sum_{n=1}^{\infty} \frac{\phi_{mn}^c \psi_{x2}}{\Lambda[\omega_{mn}^2(1+j\eta_s) - \omega^2]} \\ j\omega \sum_{m=1}^{\infty} \sum_{n=1}^{\infty} \frac{\phi_{mn}^c \psi_{y1}}{\Lambda[\omega_{mn}^2(1+j\eta_s) - \omega^2]} \\ j\omega \sum_{m=1}^{\infty} \sum_{n=1}^{\infty} \frac{\phi_{mn}^c \psi_{y2}}{\Lambda[\omega_{mn}^2(1+j\eta_s) - \omega^2]} \end{Bmatrix}^T, \quad (\text{B.3})$$

where

$$\psi_{x1} = - \int_{x_{c1}}^{x_{c2}} \psi_{mn}^y(x, y_{c1}) dx \quad (\text{B.4})$$

$$\psi_{x2} = - \int_{x_{c1}}^{x_{c2}} \psi_{mn}^y(x, y_{c2}) dx \quad (\text{B.5})$$

$$\psi_{y1} = \int_{y_{c1}}^{y_{c2}} \psi_{mn}^y(x_{c1}, y) dy \quad (\text{B.6})$$

$$\psi_{y2} = \int_{y_{c1}}^{y_{c2}} \psi_{mn}^x(x_{c2}, y) dy, \quad (\text{B.7})$$

where ψ_{mn}^x and ψ_{mn}^y are the first derivatives of $\phi_{mn}(x, y)$ with reference to x and y , respectively:

$$\psi_{mn}^x = \frac{\partial \phi_{mn}}{\partial x} = \frac{\partial \phi_x^m}{\partial x} \phi_n^y \quad (\text{B.8})$$

$$\psi_{mn}^y = \frac{\partial \phi_{mn}}{\partial y} = \phi_m^x \frac{\partial \phi_n^y}{\partial y}. \quad (\text{B.9})$$

B.2 Ideal Sensor and Lightweight Actuator

When the panel is excited by the primary excitation f_p and the control moment m_c that is generated by the lightweight elastic piezoelectric actuator, the phasor of the velocity in z-direction at the sensor position \dot{w}_c can be written using the following mobility expression:

$$\dot{w}_c = Y_{cp} f_p + \mathbf{Y}_{cc}^p m_c + \mathbf{Y}_{cm} \mathbf{f}_m, \quad (\text{B.10})$$

where Y_{cp} is given in Eq.(B.2), and \mathbf{Y}_{cc}^p is given in Eq.(B.3). \mathbf{Y}_{cm} is a n_m^2 -element row vector:

$$\mathbf{Y}_{cm} = \left[Y_{cm}^{1,1} \quad Y_{cm}^{1,2} \quad \dots \quad Y_{cm}^{h,k} \quad \dots \quad Y_{cm}^{n_m,n_m} \right]. \quad (\text{B.11})$$

h^{th}, k^{th} element of the row vector \mathbf{Y}_{cm} is given by:

$$Y_{cm}^{h,k} = j\omega \sum_{m=1}^{\infty} \sum_{n=1}^{\infty} \frac{\phi_{mn}^c \phi_{mn}^{h,k}}{\Lambda(\omega_{mn}^2(1+j\eta_s) - \omega^2)}, \quad (\text{B.12})$$

where $\phi_{mn}^{h,k}$ is a mode shape function at (x_h, y_k)

$$\phi_{mn}^{h,k} = \phi_m(x_h) \phi_n(y_k) \quad (\text{B.13})$$

The complex velocities at the centers of the lumped masses are given in the vector form:

$$\dot{\mathbf{w}}_m = \mathbf{Y}_{mp} f_p + \mathbf{Y}_{mc} m_c + \mathbf{Y}_{mm} \mathbf{f}_m, \quad (\text{B.14})$$

where \mathbf{Y}_{mp} is a n_m^2 -element column vector:

$$\mathbf{Y}_{mp} = \left[Y_{mp}^{1,1} \quad Y_{mp}^{1,2} \quad \dots \quad Y_{mp}^{h,k} \quad \dots \quad Y_{mp}^{n_m,n_m} \right]^T \quad (\text{B.15})$$

where h^{th}, k^{th} element of the column vector \mathbf{Y}_{mp} is given by:

$$Y_{mp}^{h,k} = j\omega \sum_{m=1}^{\infty} \sum_{n=1}^{\infty} \frac{\phi_{mn}^p \phi_{mn}^{h,k}}{\Lambda(\omega_{mn}^2(1+j\eta_s) - \omega^2)}. \quad (\text{B.16})$$

In Eq.(B.14), \mathbf{Y}_{mc} is a $n_m^2 \times 4$ matrix, which consists of 4 arrays of n_m^2 -element column vectors, $\mathbf{Y}_{mc_{x1}}$, $\mathbf{Y}_{mc_{x2}}$, $\mathbf{Y}_{mc_{y1}}$, and $\mathbf{Y}_{mc_{y2}}$.

$$\mathbf{Y}_{mc} = \left[\mathbf{Y}_{mc_{x1}} \quad \mathbf{Y}_{mc_{x2}} \quad \mathbf{Y}_{mc_{y1}} \quad \mathbf{Y}_{mc_{y2}} \right] \quad (\text{B.17})$$

where g^{th} element of each vector is given by:

$$Y_{mc_{x1}}^g = j\omega \sum_{m=1}^{\infty} \sum_{n=1}^{\infty} \frac{\psi_{x1} \phi_{mn}^{h,k}}{\Lambda(\omega_{mn}^2(1+j\eta_s) - \omega^2)} \quad (\text{B.18})$$

$$Y_{mc_{x2}}^g = j\omega \sum_{m=1}^{\infty} \sum_{n=1}^{\infty} \frac{\psi_{x2} \phi_{mn}^{h,k}}{\Lambda(\omega_{mn}^2(1+j\eta_s) - \omega^2)} \quad (\text{B.19})$$

$$Y_{mc_{y1}}^g = j\omega \sum_{m=1}^{\infty} \sum_{n=1}^{\infty} \frac{\psi_{y1} \phi_{mn}^{h,k}}{\Lambda(\omega_{mn}^2(1+j\eta_s) - \omega^2)} \quad (\text{B.20})$$

$$Y_{mc_{y2}}^g = j\omega \sum_{m=1}^{\infty} \sum_{n=1}^{\infty} \frac{\psi_{y2} \phi_{mn}^{h,k}}{\Lambda(\omega_{mn}^2(1+j\eta_s) - \omega^2)}, \quad (\text{B.21})$$

where $g = (n_s h + k)$.

In Eq.(B.14), \mathbf{Y}_{mm} is a $n_m^2 \times n_m^2$ matrix:

$$\mathbf{Y}_{mm} = \begin{bmatrix} Y_{mm}^{1,1} & Y_{mm}^{1,2} & \cdots & Y_{mm}^{1,n_m^2} \\ Y_{mm}^{2,1} & \ddots & & \\ \vdots & & & \\ Y_{mm}^{n_m^2,1} & & & Y_{mm}^{n_m^2,n_m^2} \end{bmatrix}, \quad (\text{B.22})$$

where g^{th}, u^{th} element of $\mathbf{Y}_{mm}^{g,u}$ are given by:

$$Y_{mm}^{g,u} = j\omega \sum_{m=1}^{\infty} \sum_{n=1}^{\infty} \frac{\phi_{mn}^{h,k} \phi_{mn}^{s,t}}{\Lambda(\omega_{mn}^2(1+j\eta_s) - \omega^2)}, \quad (\text{B.23})$$

where $u = (n_s t + s)$.

B.3 Ideal Sensor and Elastic Actuator

When the panel is excited by the primary excitation f_p and the control moment m_c that is generated by the elastic piezoelectric actuator, the phasor of the velocity in z-direction at the sensor position \dot{w}_c can be written using the following mobility expression:

$$\dot{w}_c = Y_{cp} f_p + \mathbf{Y}_{cM} \mathbf{M}_t, \quad (\text{B.24})$$

where Y_{cp} is already given in Eq.(B.2). \mathbf{Y}_{cM} is a $4n_k$ -element row vector, which consists of 4 arrays of n_k -element row vectors, $\mathbf{Y}_{cM_{x1}}$, $\mathbf{Y}_{cM_{x2}}$, $\mathbf{Y}_{cM_{y1}}$, and $\mathbf{Y}_{cM_{y2}}$:

$$\mathbf{Y}_{cM} = \left[\mathbf{Y}_{cM_{x1}} \quad \mathbf{Y}_{cM_{x2}} \quad \mathbf{Y}_{cM_{y1}} \quad \mathbf{Y}_{cM_{y2}} \right], \quad (\text{B.25})$$

where a^{th} element of each vector is given by:

$$Y_{cM_{x1}}^a = -j\omega \sum_{m=1}^{\infty} \sum_{n=1}^{\infty} \frac{\phi_{mn}^c \frac{\partial \phi}{\partial y} \Big|_{xa,yc1}}{\Lambda(\omega_{mn}^2(1+j\eta_s) - \omega^2)} \quad (\text{B.26})$$

$$Y_{cM_{x2}}^a = -j\omega \sum_{m=1}^{\infty} \sum_{n=1}^{\infty} \frac{\phi_{mn}^c \frac{\partial \phi}{\partial y} \Big|_{xa,yc2}}{\Lambda(\omega_{mn}^2(1+j\eta_s) - \omega^2)} \quad (\text{B.27})$$

$$Y_{cM_{y1}}^a = j\omega \sum_{m=1}^{\infty} \sum_{n=1}^{\infty} \frac{\phi_{mn}^c \frac{\partial \phi}{\partial x} \Big|_{xc1,ya}}{\Lambda(\omega_{mn}^2(1+j\eta_s) - \omega^2)} \quad (\text{B.28})$$

$$Y_{cM_{y2}}^a = j\omega \sum_{m=1}^{\infty} \sum_{n=1}^{\infty} \frac{\phi_{mn}^c \frac{\partial \phi}{\partial x} \Big|_{xc2,ya}}{\Lambda(\omega_{mn}^2(1+j\eta_s) - \omega^2)}. \quad (\text{B.29})$$

The complex angular velocities along the edges of the patch actuator are given in the vector form:

$$\dot{\boldsymbol{\theta}} = \mathbf{Y}_{\theta_p} f_p + \mathbf{Y}_{\theta_M} \mathbf{M}_t, \quad (\text{B.30})$$

where \mathbf{Y}_{θ_p} is a $4n_k$ -element row vector, which consists of 4 arrays of n_k -element row vectors, $\mathbf{Y}_{\theta_{x1p}}$, $\mathbf{Y}_{\theta_{x2p}}$, $\mathbf{Y}_{\theta_{y1p}}$, and $\mathbf{Y}_{\theta_{y2p}}$:

$$\mathbf{Y}_{\theta_p} = \left[\mathbf{Y}_{\theta_{x1p}} \quad \mathbf{Y}_{\theta_{x2p}} \quad \mathbf{Y}_{\theta_{y1p}} \quad \mathbf{Y}_{\theta_{y2p}} \right]^T, \quad (\text{B.31})$$

where a^{th} element of each vector in \mathbf{Y}_{θ_p} , is given by:

$$Y_{\theta_{x1p}}^a = -j\omega \sum_{m=1}^{\infty} \sum_{n=1}^{\infty} \frac{\phi_{mn}^p \frac{\partial \phi}{\partial y} \Big|_{xa,yc1}}{\Lambda(\omega_{mn}^2(1+j\eta_s) - \omega^2)} \quad (\text{B.32})$$

$$Y_{\theta_{x2p}}^a = -j\omega \sum_{m=1}^{\infty} \sum_{n=1}^{\infty} \frac{\phi_{mn}^p \frac{\partial \phi}{\partial y} \Big|_{xa,yc2}}{\Lambda(\omega_{mn}^2(1+j\eta_s) - \omega^2)} \quad (\text{B.33})$$

$$Y_{\theta_{y1p}}^a = j\omega \sum_{m=1}^{\infty} \sum_{n=1}^{\infty} \frac{\phi_{mn}^p \frac{\partial \phi}{\partial x} \Big|_{xc1,ya}}{\Lambda(\omega_{mn}^2(1+j\eta_s) - \omega^2)} \quad (\text{B.34})$$

$$Y_{\theta_{y2p}}^a = j\omega \sum_{m=1}^{\infty} \sum_{n=1}^{\infty} \frac{\phi_{mn}^p \frac{\partial \phi}{\partial x} \Big|_{xc2,ya}}{\Lambda(\omega_{mn}^2(1+j\eta_s) - \omega^2)}. \quad (\text{B.35})$$

In Eq.(B.30), \mathbf{Y}_{θ_M} is a $4n_k \times 4n_k$ matrix, which consists of 4×4 arrays of matrices with $n_k \times n_k$ element:

$$\mathbf{Y}_{\theta_M} = \begin{bmatrix} \mathbf{Y}_{\theta_{x1}M_{x1}} & \mathbf{Y}_{\theta_{x1}M_{x2}} & \mathbf{Y}_{\theta_{x1}M_{y1}} & \mathbf{Y}_{\theta_{x1}M_{y2}} \\ \mathbf{Y}_{\theta_{x2}M_{x1}} & \mathbf{Y}_{\theta_{x2}M_{x2}} & \mathbf{Y}_{\theta_{x2}M_{y1}} & \mathbf{Y}_{\theta_{x2}M_{y2}} \\ \mathbf{Y}_{\theta_{y1}M_{x1}} & \mathbf{Y}_{\theta_{y1}M_{x2}} & \mathbf{Y}_{\theta_{y1}M_{y1}} & \mathbf{Y}_{\theta_{y1}M_{y2}} \\ \mathbf{Y}_{\theta_{y2}M_{x1}} & \mathbf{Y}_{\theta_{y2}M_{x2}} & \mathbf{Y}_{\theta_{y2}M_{y1}} & \mathbf{Y}_{\theta_{y2}M_{y2}} \end{bmatrix}, \quad (\text{B.36})$$

where $a^{\text{th}}, b^{\text{th}}$ element of each matrix in \mathbf{Y}_{θ_M} are given below:

$$Y_{\theta_{x1},M_{x1}}^{a,b} = j\omega \sum_{m=1}^{\infty} \sum_{n=1}^{\infty} \frac{\frac{\partial \phi}{\partial y} \Big|_{xa,yc1} \frac{\partial \phi}{\partial y} \Big|_{xb,yc1}}{\Lambda(\omega_{mn}^2(1+j\eta_s) - \omega^2)} \quad (\text{B.37})$$

$$Y_{\theta_{x1},M_{x2}}^{a,b} = j\omega \sum_{m=1}^{\infty} \sum_{n=1}^{\infty} \frac{\frac{\partial \phi}{\partial y} \Big|_{xa,yc2} \frac{\partial \phi}{\partial y} \Big|_{xb,yc1}}{\Lambda(\omega_{mn}^2(1+j\eta_s) - \omega^2)} \quad (\text{B.38})$$

$$Y_{\theta_{x2},M_{x1}}^{a,b} = j\omega \sum_{m=1}^{\infty} \sum_{n=1}^{\infty} \frac{\frac{\partial \phi}{\partial y} \Big|_{xa,yc1} \frac{\partial \phi}{\partial y} \Big|_{xb,yc2}}{\Lambda(\omega_{mn}^2(1+j\eta_s) - \omega^2)} \quad (\text{B.39})$$

$$Y_{\theta_{x2}, M_{x2}}^{a,b} = j\omega \sum_{m=1}^{\infty} \sum_{n=1}^{\infty} \frac{\frac{\partial \phi}{\partial y} \Big|_{xa,yc2} \frac{\partial \phi}{\partial y} \Big|_{xb,yc2}}{\Lambda(\omega_{mn}^2(1+j\eta_s) - \omega^2)} \quad (\text{B.40})$$

$$Y_{\theta_{x1}, M_{y1}}^{a,b} = -j\omega \sum_{m=1}^{\infty} \sum_{n=1}^{\infty} \frac{\frac{\partial \phi}{\partial x} \Big|_{xc1,ya} \frac{\partial \phi}{\partial y} \Big|_{xb,yc1}}{\Lambda(\omega_{mn}^2(1+j\eta_s) - \omega^2)} \quad (\text{B.41})$$

$$Y_{\theta_{x1}, M_{y2}}^{a,b} = -j\omega \sum_{m=1}^{\infty} \sum_{n=1}^{\infty} \frac{\frac{\partial \phi}{\partial x} \Big|_{xc2,ya} \frac{\partial \phi}{\partial y} \Big|_{xb,yc1}}{\Lambda(\omega_{mn}^2(1+j\eta_s) - \omega^2)} \quad (\text{B.42})$$

$$Y_{\theta_{x2}, M_{y1}}^{a,b} = -j\omega \sum_{m=1}^{\infty} \sum_{n=1}^{\infty} \frac{\frac{\partial \phi}{\partial x} \Big|_{xc1,ya} \frac{\partial \phi}{\partial y} \Big|_{xb,yc2}}{\Lambda(\omega_{mn}^2(1+j\eta_s) - \omega^2)} \quad (\text{B.43})$$

$$Y_{\theta_{x2}, M_{y2}}^{a,b} = -j\omega \sum_{m=1}^{\infty} \sum_{n=1}^{\infty} \frac{\frac{\partial \phi}{\partial x} \Big|_{xc2,ya} \frac{\partial \phi}{\partial y} \Big|_{xb,yc2}}{\Lambda(\omega_{mn}^2(1+j\eta_s) - \omega^2)} \quad (\text{B.44})$$

$$Y_{\theta_{y1}, M_{x1}}^{a,b} = -j\omega \sum_{m=1}^{\infty} \sum_{n=1}^{\infty} \frac{\frac{\partial \phi}{\partial y} \Big|_{xa,yc1} \frac{\partial \phi}{\partial x} \Big|_{xc1,yb}}{\Lambda(\omega_{mn}^2(1+j\eta_s) - \omega^2)} \quad (\text{B.45})$$

$$Y_{\theta_{y1}, M_{x2}}^{a,b} = -j\omega \sum_{m=1}^{\infty} \sum_{n=1}^{\infty} \frac{\frac{\partial \phi}{\partial y} \Big|_{xa,yc2} \frac{\partial \phi}{\partial x} \Big|_{xc1,yb}}{\Lambda(\omega_{mn}^2(1+j\eta_s) - \omega^2)} \quad (\text{B.46})$$

$$Y_{\theta_{y2}, M_{x1}}^{a,b} = -j\omega \sum_{m=1}^{\infty} \sum_{n=1}^{\infty} \frac{\frac{\partial \phi}{\partial y} \Big|_{xa,yc1} \frac{\partial \phi}{\partial x} \Big|_{xc2,yb}}{\Lambda(\omega_{mn}^2(1+j\eta_s) - \omega^2)} \quad (\text{B.47})$$

$$Y_{\theta_{y2}, M_{x2}}^{a,b} = -j\omega \sum_{m=1}^{\infty} \sum_{n=1}^{\infty} \frac{\frac{\partial \phi}{\partial y} \Big|_{xa,yc2} \frac{\partial \phi}{\partial x} \Big|_{xc2,yb}}{\Lambda(\omega_{mn}^2(1+j\eta_s) - \omega^2)} \quad (\text{B.48})$$

$$Y_{\theta_{y1}, M_{y1}}^{a,b} = j\omega \sum_{m=1}^{\infty} \sum_{n=1}^{\infty} \frac{\frac{\partial \phi}{\partial x} \Big|_{xc1,ya} \frac{\partial \phi}{\partial x} \Big|_{xc1,yb}}{\Lambda(\omega_{mn}^2(1+j\eta_s) - \omega^2)} \quad (\text{B.49})$$

$$Y_{\theta_{y1}, M_{y2}}^{a,b} = j\omega \sum_{m=1}^{\infty} \sum_{n=1}^{\infty} \frac{\frac{\partial \phi}{\partial x} \Big|_{xc2,ya} \frac{\partial \phi}{\partial x} \Big|_{xc1,yb}}{\Lambda(\omega_{mn}^2(1+j\eta_s) - \omega^2)} \quad (\text{B.50})$$

$$Y_{\theta_{y2}, M_{y1}}^{a,b} = j\omega \sum_{m=1}^{\infty} \sum_{n=1}^{\infty} \frac{\frac{\partial \phi}{\partial x} \Big|_{xc1,ya} \frac{\partial \phi}{\partial x} \Big|_{xc2,yb}}{\Lambda(\omega_{mn}^2(1+j\eta_s) - \omega^2)} \quad (\text{B.51})$$

$$Y_{\theta_{y2}, M_{y2}}^{a,b} = j\omega \sum_{m=1}^{\infty} \sum_{n=1}^{\infty} \frac{\frac{\partial \phi}{\partial x} \Big|_{xc2,ya} \frac{\partial \phi}{\partial x} \Big|_{xc2,yb}}{\Lambda(\omega_{mn}^2(1+j\eta_s) - \omega^2)} \quad (\text{B.52})$$

B.4 Actuator-Plate Fully Coupled Model

When the panel is excited by the primary excitation f_p and the control moment m_c that is generated by the lightweight elastic piezoelectric actuator, the phasor of the velocity in z-direction at the sensor position \dot{w}_c can be written using the following mobility expression:

$$\dot{w}_c = Y_{cp}f_p + \mathbf{Y}_{cm}\mathbf{f}_m + \mathbf{Y}_{cM}\mathbf{M}_t, \quad (\text{B.53})$$

where Y_{cp} is given in Eq.(B.2), \mathbf{Y}_{cm} is given in Eq.(B.11), and \mathbf{Y}_{cM} is given in Eq.(B.25).

The complex velocities at the centers of the lumped masses are given in the vector form:

$$\dot{\mathbf{w}}_m = \mathbf{Y}_{mp} \mathbf{f}_p + \mathbf{Y}_{mm} \mathbf{f}_m + \mathbf{Y}_{mM} \mathbf{M}_t, \quad (\text{B.54})$$

where \mathbf{Y}_{mp} is given in Eq.(B.15), and \mathbf{Y}_{mm} is given in Eq.(B.22). \mathbf{Y}_{mM} is a $n_m^2 \times 4n_k$ matrix, which consists of 4 arrays of matrices with $n_m^2 \times n_k$ elements, $\mathbf{Y}_{mM_{x1}}$, $\mathbf{Y}_{mM_{x2}}$, $\mathbf{Y}_{mM_{y1}}$, and $\mathbf{Y}_{mM_{y2}}$:

$$\mathbf{Y}_{mM} = \begin{bmatrix} \mathbf{Y}_{mM_{x1}} & \mathbf{Y}_{mM_{x2}} & \mathbf{Y}_{mM_{y1}} & \mathbf{Y}_{mM_{y2}} \end{bmatrix}, \quad (\text{B.55})$$

where g^{th} , a^{th} element of each matrix is given below:

$$Y_{mM_{x1}}^{g,a} = -j\omega \sum_{m=1}^{\infty} \sum_{n=1}^{\infty} \frac{\phi_{mn}^{h,k} \frac{\partial \phi}{\partial y} \Big|_{xa,yc1}}{\Lambda(\omega_{mn}^2(1+j\eta_s) - \omega^2)} \quad (\text{B.56})$$

$$Y_{mM_{x2}}^{g,a} = -j\omega \sum_{m=1}^{\infty} \sum_{n=1}^{\infty} \frac{\phi_{mn}^{h,k} \frac{\partial \phi}{\partial y} \Big|_{xa,yc2}}{\Lambda(\omega_{mn}^2(1+j\eta_s) - \omega^2)} \quad (\text{B.57})$$

$$Y_{mM_{y1}}^{g,a} = j\omega \sum_{m=1}^{\infty} \sum_{n=1}^{\infty} \frac{\phi_{mn}^{h,k} \frac{\partial \phi}{\partial x} \Big|_{xc1,ya}}{\Lambda(\omega_{mn}^2(1+j\eta_s) - \omega^2)} \quad (\text{B.58})$$

$$Y_{mM_{y2}}^{g,a} = j\omega \sum_{m=1}^{\infty} \sum_{n=1}^{\infty} \frac{\phi_{mn}^{h,k} \frac{\partial \phi}{\partial x} \Big|_{xc2,ya}}{\Lambda(\omega_{mn}^2(1+j\eta_s) - \omega^2)}. \quad (\text{B.59})$$

The complex angular velocities along the edges of the patch actuator are given in the vector form:

$$\dot{\boldsymbol{\theta}} = \mathbf{Y}_{\theta p} \mathbf{f}_p + \mathbf{Y}_{\theta m} \mathbf{f}_m + \mathbf{Y}_{\theta M} \mathbf{M}_t, \quad (\text{B.60})$$

where $\mathbf{Y}_{\theta p}$ is given in Eq.(B.31), $\mathbf{Y}_{\theta M}$ is given in Eq.(B.36). $\mathbf{Y}_{\theta m}$ is a $4n_k \times n_m^2$ matrix, which consists of 4 arrays of $n_k \times n_m^2$ matrices, $\mathbf{Y}_{\theta_{x1}m}$, $\mathbf{Y}_{\theta_{x2}m}$, $\mathbf{Y}_{\theta_{y1}m}$, and $\mathbf{Y}_{\theta_{y2}m}$:

$$\mathbf{Y}_{\theta m} = \begin{bmatrix} \mathbf{Y}_{\theta_{x1}m} & \mathbf{Y}_{\theta_{x2}m} & \mathbf{Y}_{\theta_{y1}m} & \mathbf{Y}_{\theta_{y2}m} \end{bmatrix}, \quad (\text{B.61})$$

where a^{th} , g^{th} element of each matrix is given below:

$$Y_{\theta_{x1}m}^{a,g} = -j\omega \sum_{m=1}^{\infty} \sum_{n=1}^{\infty} \frac{\phi_{mn}^{h,k} \frac{\partial \phi}{\partial y} \Big|_{xa,yc1}}{\Lambda(\omega_{mn}^2(1+j\eta_s) - \omega^2)} \quad (\text{B.62})$$

$$Y_{\theta_{x2}m}^{a,g} = -j\omega \sum_{m=1}^{\infty} \sum_{n=1}^{\infty} \frac{\phi_{mn}^{h,k} \frac{\partial \phi}{\partial y} \Big|_{xa,yc2}}{\Lambda(\omega_{mn}^2(1+j\eta_s) - \omega^2)} \quad (\text{B.63})$$

$$Y_{\theta_{y1}m}^{a,g} = j\omega \sum_{m=1}^{\infty} \sum_{n=1}^{\infty} \frac{\phi_{mn}^{h,k} \frac{\partial \phi}{\partial x} \Big|_{xc1,ya}}{\Lambda(\omega_{mn}^2(1+j\eta_s) - \omega^2)} \quad (\text{B.64})$$

$$Y_{\theta_{y2}m}^{a,g} = j\omega \sum_{m=1}^{\infty} \sum_{n=1}^{\infty} \frac{\phi_{mn}^{h,k} \frac{\partial \phi}{\partial x} \Big|_{xc2,ya}}{\Lambda(\omega_{mn}^2(1+j\eta_s) - \omega^2)}. \quad (\text{B.65})$$

B.5 Actuator-Sensor-Plate Fully Coupled Model

When the panel is excited by the primary excitation f_p , and the control moment m_c generated by the lightweight elastic piezoelectric actuator, the phasor of the velocity in z-direction at the sensor position \dot{w}_c can be written using the following mobility expression:

$$\dot{w}_c = Y_{cp}f_p + \mathbf{Y}_{cm}\mathbf{f}_m + \mathbf{Y}_{cM}\mathbf{M}_t + Y_{cc}(f_{a1} + f_h), \quad (\text{B.66})$$

where Y_{cp} is given in Eq.(B.2), \mathbf{Y}_{cm} is given in Eq.(B.11), and \mathbf{Y}_{cM} is given in Eq.(B.25). Y_{cc} is given below:

$$Y_{cc} = j\omega \sum_{m=1}^{\infty} \sum_{n=1}^{\infty} \frac{\phi_{mn}^c \phi_{mn}^c}{\Lambda(\omega_{mn}^2(1 + j\eta_s) - \omega^2)}. \quad (\text{B.67})$$

The complex velocities at the centers of the lumped masses are given in the vector form:

$$\dot{\mathbf{w}}_m = \mathbf{Y}_{mp}f_p + \mathbf{Y}_{mm}\mathbf{f}_m + \mathbf{Y}_{mM}\mathbf{M}_t + \mathbf{Y}_{mc}(f_{a1} + f_h), \quad (\text{B.68})$$

where \mathbf{Y}_{mp} is given in Eq.(B.15), \mathbf{Y}_{mm} is given in Eq.(B.22), and \mathbf{Y}_{mM} is given in Eq.(B.55). \mathbf{Y}_{mc} is n_m^2 -element column vector:

$$\mathbf{Y}_{mc} = \left[Y_{mc}^{1,1} \quad Y_{mc}^{1,2} \quad \dots \quad Y_{mc}^{h,k} \quad \dots \quad Y_{mc}^{n_m,n_m} \right]^T, \quad (\text{B.69})$$

where h^{th}, k^{th} element of column matrix \mathbf{Y}_{mc} is given below:

$$Y_{mc}^{h,k} = j\omega \sum_{m=1}^{\infty} \sum_{n=1}^{\infty} \frac{\phi_{mn}^c \phi_{mn}^{h,k}}{\Lambda(\omega_{mn}^2(1 + j\eta_s) - \omega^2)}. \quad (\text{B.70})$$

The complex angular velocities along the edges of the patch actuator are given in the vector form:

$$\dot{\boldsymbol{\theta}} = \mathbf{Y}_{\theta p}f_p + \mathbf{Y}_{\theta m}\mathbf{f}_m + \mathbf{Y}_{\theta M}\mathbf{M}_t + \mathbf{Y}_{\theta c}(f_{a1} + f_h), \quad (\text{B.71})$$

where $\mathbf{Y}_{\theta M}$ is given in Eq.(B.36), $\mathbf{Y}_{\theta p}$ is given in Eq.(B.31), and $\mathbf{Y}_{\theta m}$ is given in Eq.(B.61). $\mathbf{Y}_{\theta c}$ is a $4n_k$ -element column vector, which consists of 4 arrays of n_k -element column vectors, $\mathbf{Y}_{\theta_{x1c}}$, $\mathbf{Y}_{\theta_{x2c}}$, $\mathbf{Y}_{\theta_{y1c}}$, and $\mathbf{Y}_{\theta_{y2c}}$:

$$\mathbf{Y}_{\theta c} = \left[\mathbf{Y}_{\theta_{x1c}} \quad \mathbf{Y}_{\theta_{x2c}} \quad \mathbf{Y}_{\theta_{y1c}} \quad \mathbf{Y}_{\theta_{y2c}} \right]^T, \quad (\text{B.72})$$

where a^{th} element of each vector is given below:

$$Y_{\theta_{xc}}^a = -j\omega \sum_{m=1}^{\infty} \sum_{n=1}^{\infty} \frac{\phi_{mn}^c \frac{\partial \phi}{\partial y} \Big|_{xa,yc1}}{\Lambda(\omega_{mn}^2(1 + j\eta_s) - \omega^2)} \quad (\text{B.73})$$

$$Y_{\theta_{yc}}^a = -j\omega \sum_{m=1}^{\infty} \sum_{n=1}^{\infty} \frac{\phi_{mn}^c \frac{\partial \phi}{\partial y} \Big|_{xa,yc2}}{\Lambda(\omega_{mn}^2(1 + j\eta_s) - \omega^2)} \quad (\text{B.74})$$

$$Y_{\theta_{xc}}^a = j\omega \sum_{m=1}^{\infty} \sum_{n=1}^{\infty} \frac{\phi_{mn}^c \frac{\partial \phi}{\partial x} \Big|_{xc1,ya}}{\Lambda(\omega_{mn}^2(1 + j\eta_s) - \omega^2)} \quad (\text{B.75})$$

$$Y_{\theta_{yc}}^a = j\omega \sum_{m=1}^{\infty} \sum_{n=1}^{\infty} \frac{\phi_{mn}^c \frac{\partial \phi}{\partial x} \Big|_{xc2,ya}}{\Lambda(\omega_{mn}^2(1 + j\eta_s) - \omega^2)}. \quad (\text{B.76})$$

Appendix C

Piezoelectric Actuator Induced Moment

This appendix introduces the formulation of the effective actuation moments induced by the piezoelectric patch actuator to the supporting structure. Clawley et al.[17] have investigated the behavior of a pair of piezoelectric patches bonded on both surfaces of a beam, and derived the formulation of the actuation moment induced in the beam. Dimitriadis et al.[18] have developed the similar formulation for a two-dimensional problem as an extension of Clawley's work. Fuller et al.[19] complemented these works by adding the formulation of the actuation moment induced by the single piezoelectric patch bonded on one surfaces of the beam. In this report, the actuation moment induced by a single two-dimensional rectangular piezoelectric actuator bonded on single surface of a flat panel, is discussed. The method of formulation used in this report follows the above mentioned previous works.

In the model formulation, the following assumptions were made:

1. A two-dimensional piezoelectric actuator has the same properties in the 1- and 2- directions.
2. The piezoelectric actuator patch is perfectly bonded to the surface of a plate[17].

When an unconstrained piezoelectric patch actuator is activated by applying a voltage, the piezoelectric patch develops strain, as shown in Figure C.1-(a). The magnitude of the induced strains of an unconstrained patch ϵ_{pzt} can be expressed by:

$$\epsilon_{pzt} = \frac{d_{31}V_c}{h_{pzt}}, \quad (\text{C.1})$$

where d_{31} denotes the piezoelectric strain constant, V_c is the applied control voltage, and h_{pzt} is the thickness of the patch.

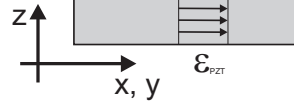
When a bonded piezoelectric patch actuator is activated by a voltage, the piezoelectric patch develops strain, which however is constrained due to the stiffness of the supporting structure. As a result of Kirchhoff's hypothesis of Classic Laminate Plate Theory (CLPT)[20], the strain distribution is assumed linear. Furthermore, the assumption of perfect bonding between the actuator patch and the plate implies that strain is continuous at the interface. Due to the geometric asymmetry of the structure, the generated strain within the panel is asymmetric with reference to the middle plane of the panel, as shown in Figure C.1-(b).

Therefore, the formulas of the strain distribution in the x- and y- directions can be expressed as:

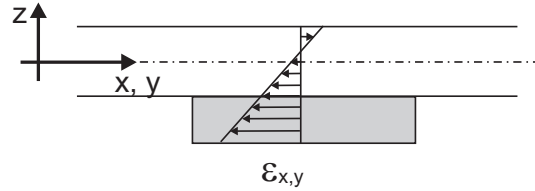
$$\epsilon_x = C_x z + \epsilon_{x0}, \quad (\text{C.2})$$

$$\epsilon_y = C_y z + \epsilon_{y0}, \quad (\text{C.3})$$

where C_x and C_y are the slopes of the strain distribution, and ϵ_{x0} and ϵ_{y0} denote the z-intercept for the x-z and y-z planes, respectively.



(a) Unconstrained piezoelectric patch



(b) Bonded piezoelectric patch

Figure C.1: Strain distribution; (a)unconstrained piezoelectric actuator(Top) and (b) bonded piezoelectric actuator on the panel (bottm)

According to Hook's low, the stress distribution within the panel is given by:

$$\sigma_s^x = \frac{E_s}{1 - \nu_s^2} (\epsilon_x + \nu_s \epsilon_y), \quad (\text{C.4})$$

$$\sigma_s^y = \frac{E_s}{1 - \nu_s^2} (\epsilon_y + \nu_s \epsilon_x), \quad (\text{C.5})$$

where E_s and ν_s respectively denote the elastic module and poisson ration of the panel. The stress distribution within the patch actuator is given as a result of superposing the passive stress σ_{pzt}^k due to external plate strains at the interface, and the active stress σ_{pzt}^a due to unconstrained piezoelectric patch strain, as shown in Figure C.2:

$$\sigma_{pzt}^x = \frac{E_{pzt}}{1 - \nu_{pzt}^2} \{ (\epsilon_x + \nu_{pzt} \epsilon_y) - (1 + \nu_{pzt}) \epsilon_{pzt} \}, \quad (\text{C.6})$$

$$\sigma_{pzt}^y = \frac{E_{pzt}}{1 - \nu_{pzt}^2} \{ (\epsilon_y + \nu_{pzt} \epsilon_x) - (1 + \nu_{pzt}) \epsilon_{pzt} \}, \quad (\text{C.7})$$

where E_{pzt} and ν_{pzt} respectively denote the elastic module and poisson ratio of the piezoelectric patch actuator.

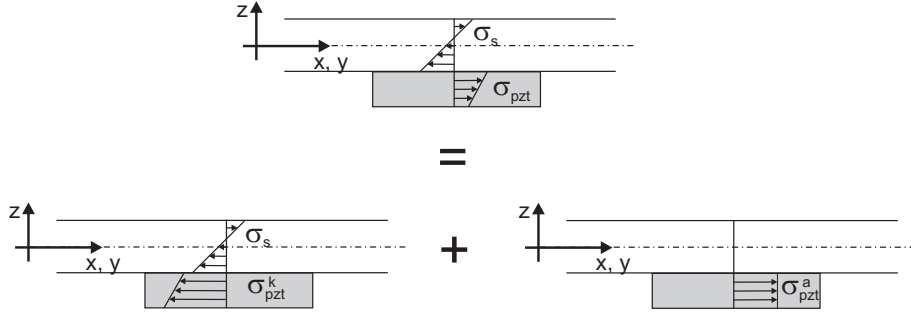


Figure C.2: Stress distribution (top) and its decomposition into passive (bottom left) and active stress (bottom right)

Applying force and moment equilibriums about the middle plane of the panel in the x- and y-directions produce the following relations:

$$\begin{aligned}
 \int_{-\frac{h_s}{2}}^{\frac{h_s}{2}} \sigma_s^x dz + \int_{-\frac{h_s}{2}-h_{pzt}}^{-\frac{h_s}{2}} \sigma_{pzt}^x dz &= 0, \\
 \int_{-\frac{h_s}{2}}^{\frac{h_s}{2}} \sigma_s^y dz + \int_{-\frac{h_s}{2}-h_{pzt}}^{-\frac{h_s}{2}} \sigma_{pzt}^y dz &= 0,
 \end{aligned} \tag{C.8}$$

$$\begin{aligned}
 \int_{-\frac{h_s}{2}}^{\frac{h_s}{2}} \sigma_s^x z dz + \int_{-\frac{h_s}{2}-h_{pzt}}^{-\frac{h_s}{2}} \sigma_{pzt}^x z dz &= 0, \\
 \int_{-\frac{h_s}{2}}^{\frac{h_s}{2}} \sigma_s^y z dz + \int_{-\frac{h_s}{2}-h_{pzt}}^{-\frac{h_s}{2}} \sigma_{pzt}^y z dz &= 0,
 \end{aligned} \tag{C.9}$$

where h_s denotes the thicknesses of the panel. After integration, Eq.(C.8) and Eq.(C.9) can be solved for unknowns C_x , C_y , ϵ_x , and ϵ_y , which are given by:

$$C = C_x = C_y = K_f \epsilon_{pzt}, \tag{C.10}$$

$$\epsilon_0 = \epsilon_{x0} = \epsilon_{y0} = K_L \epsilon_{pzt}, \tag{C.11}$$

where material-geometric constant K_f and K_L are given by:

$$K_f = \frac{6\bar{E}_s \bar{E}_{pzt} h_s h_{pzt} (h_s + h_{pzt})}{\bar{E}_s^2 h_s^4 + 2\bar{E}_s \bar{E}_{pzt} (2h_s^3 h_{pzt} + 3h_s^2 h_{pzt}^2 + 2h_s h_{pzt}^3) + \bar{E}_{pzt}^2 h_{pzt}^4}, \tag{C.12}$$

$$K_L = \frac{\bar{E}_{pzt} h_{pzt} (\bar{E}_s h_s^3 + \bar{E}_{pzt} h_{pzt}^3)}{\bar{E}_s^2 h_s^4 + 2\bar{E}_s \bar{E}_{pzt} (2h_s^3 h_{pzt} + 3h_s^2 h_{pzt}^2 + 2h_s h_{pzt}^3) + \bar{E}_{pzt}^2 h_{pzt}^4}, \tag{C.13}$$

where

$$\bar{E}_s = \frac{E_s}{1 - \nu_s}, \tag{C.14}$$

$$\bar{E}_{pzt} = \frac{E_{pzt}}{1 - \nu_{pzt}}. \tag{C.15}$$

Thus, the effective bending moment applied to the plate induced by a piezoelectric patch m_c can be expressed as follows:

$$\begin{aligned}
 m_c &= \int_{-\frac{h_s}{2}}^{\frac{h_s}{2}} \sigma_s z dz, \\
 &= \frac{\bar{E}_s h_s^3}{12} \frac{d_{31}}{h_{pzt}} K_f V_c, \\
 &= c_\alpha V_c.
 \end{aligned} \tag{C.16}$$

Additionally, the effective inplane force applied to the plate induced by a piezoelectric patch f_u can be expressed as follows:

$$\begin{aligned}
 f_u &= \int_{-\frac{h_s}{2}}^{\frac{h_s}{2}} \sigma_s dz, \\
 &= \bar{E}_s K_L h_s \frac{d_{31}}{h_{pzt}} V_c, \\
 &= c_\beta V_c.
 \end{aligned} \tag{C.17}$$

Reference

- [1] F. Fahy and P. Gardonio, *Sound and Structural Vibration*, Academic Press, London (2006).
- [2] A. Preumont, *Vibration Control of Active Structures*, 2nd edition, Kluwer Academic Publishers, Dordrecht (2002).
- [3] M. J. Balas, Direct velocity control of large space structures, *Journal of Guidance and Control* 2, 252-253 (1979).
- [4] R. L. Clark, W. R. Saunders and G. P. Gibbs, *Adaptive Structures*, 1st Edition, New York: John Wiley and Sons, Inc. (1998).
- [5] J. Q. Sun, Some observations on physical duality and collocation of structural control sensors and actuators, *Journal of Sound and Vibration* 194, 765-770 (1996).
- [6] V. Jayachandran and J. Q. Sun, Unconditional stability domains of structural control systems using dual actuator-sensor pairs, *Journal of Sound and Vibration* 208, 159-166 (1997).
- [7] S. J. Elliott, P. Gardonio, T. C. Sors, and M. J. Brennan, Active vibroacoustic control with multiple local feedback loops, *Journal of the Acoustical Society of America* 111[2], 908-915 (2002).
- [8] P. Gardonio, E. Bianchi, and S. J. Elliott, Smart panel with multiple decentralized units for the control of sound transmission. Part I: theoretical predictions, *Journal of Sound and Vibration* 274[1-2], 163-192 (2004).
- [9] P. Gardonio, E. Bianchi, and S. J. Elliott, Smart panel with multiple decentralized units for the control of sound transmission. Part II: design of the decentralized control units, *Journal of Sound and Vibration* 274[1-2], 193-213 (2004).
- [10] E. Bianchi, P. Gardonio, and S. J. Elliott, Smart panel with multiple decentralized units for the control of sound transmission. Part III: Control System Implementation, *Journal of Sound and Vibration* 274[1-2], 215-232 (2004).
- [11] C. K. Lee, Theory of laminated piezoelectric plates of the design of distributed sensors/actuators. Part I: Governing equations and reciprocal relationships, *Journal of the Acoustical Society of America* 87, 1144-1158 (1990).
- [12] P. Gardonio and S. J. Elliott, Smart Panels for Active Structural Acoustic Control, *Smart Materials and Structures* 13, 1314-1336 (2004).

- [13] L. C. Cremer and M. Heckel, *Structure-Borne Sound*, Springer Verlag (1988)
- [14] F. J. Fahy , P. Gardonio, *Sound and Structural Vibration : Radiation, Transmission and Response*, Academic Press (2007).
- [15] Y. Aoki, P. Gardonio, and S. J. Elliott, Parametric Study of a Piezoelectric Patch-Accelerometer Pair For Velocity Feedback Control, *IOA Spring conference, Southampton* (2006).
- [16] M. J. Brennan, S. J. Elliott, and R. J. Pinnington, The dynamic coupling between piezoceramic actuators and a beam, *Journal of the Acoustical Society of America* 102[4], 1931-1942 (1997)
- [17] E. F. Crawley and J. Luis, Use of Piezoelectric Actuators as Elements of Intelligent Structures, *AIAA Journal*, volume 25[10], 1373-1385 (1989).
- [18] E. K. Dimitriadis, C. R. Fuller, C. A. Roger, Piezoelectric actuators for distributed vibration excitation of thin plates , *Journal of Vibration and Acoustics Transactions of the ASME* 113, 100-107 (1991)
- [19] C. R. Fuller, S. J. Elliott, and P. A. Nelson, *Active Control of Vibration*, London Academic Press (2002).
- [20] J. N. Reddy, *Mechanics of Laminated Composite Plates Theory and Analysis*, CRC (1996)
- [21] P. Gardonio and S. J. Elliott, Modal response of a beam with a sensor-actuator pair for the implementation of velocity feedback control, *Journal of Sound and Vibration* 284[1-2], 1-22 (2005)
- [22] L. Meirovitch, *Dynamics and Control of Structures*, John Wiley and Sons, New York (1990).
- [23] P. Gardonio, Y. S. Lee, S. J. Elliott and S. Debost, Analysis and measure of a matched volume velocity sensor and uniform force actuator for active structural acoustic control, *Journal of the Acoustical Society of America* 110[6], 3025-3031 (2001).
- [24] R. L. Clark and C. R. Fuller, Optimal placement of piezoceramic actuators and polyvinylidene fluoride error sensors in active structural acoustic control approaches, *Journal of the Acoustical Society of America* 92[3], 1521-1533 (1992).
- [25] T. C. Scors and S. J. Elliott, Volume Velocity Estimation with Accelerometer Arrays for Active Structural Acoustic Control, *Journal of Sound and Vibration* 258 [5], 867-883 (2002).
- [26] B. T. Wang, C. R. Fuller and E. K. Dimitriadis, Active control of noise transmission through rectangular plates using multiple piezoelectric or point force actuators, *Journal of the Acoustical Society of America* 90, 2820-2830 (1991).